

AN ABSTRACT OF THE DISSERTATION OF

Junhui Lou for the degree of Doctor of Philosophy in Civil Engineering presented on March 22, 2017.

Title: Numerical Simulation, Laboratory and Field Experiments, Analysis and Design of Wave Energy Converter and Mooring System

Abstract approved:

Solomon C. Yim

Abstract:

This dissertation studies the coupled fluid-structure interaction (FSI) of a wave energy converter (WEC) and evaluates the design of a WEC mooring system. The research is conducted in support of conceptual development, field test and performance evaluation of WECs as part of the mission of the Northwest National Marine Renewable Energy Center at Oregon State University. The coupled FSI study focuses on the evaluation of predictive capabilities and computational performance of commercial computational fluid dynamics (CFD) and potential flow codes using laboratory model test results. The evaluations of a WEC mooring system focus on analysis of field test data and evaluations of the anchor movability, fatigue design and extreme load of the Ocean Sentinel (OS) test platform mooring system deployed off the Oregon coast. Numerical data using a commercial mooring system simulation code are conducted to supplement time history data for the calculations of anchor pulling force, fatigue damage and extreme load.

Specifically, this dissertation can be divided into three parts. In the first part the performances of a finite element explicit Navier-Stokes (NS) solver (LS-DYNA ALE), a finite element implicit NS solver (LS-DYNA ICFD), and a nonlinear potential flow solver (AQWA) in predicting highly nonlinear hydrodynamic responses of a floating point absorber (FPA) under large-amplitude waves are studied. The two NS solvers calculate the coupled FSI including fully nonlinear inviscid and viscous forces. The nonlinear potential flow solver calculates individual inviscid wave force components (a Froude-Krylov force, a radiation force, a diffraction force and a hydrostatic force) and empirical (Morison equation) viscous force. Comparing numerical results to laboratory experimental measurements, the two NS solvers and the nonlinear potential flow solver are found to be capable of providing accurate predictions of the nonlinear motion responses of the FPA. FSI coupling algorithms and computational costs of these three solvers are evaluated. Based on the results of the nonlinear potential flow solver at different wave periods, the individual wave force components and the viscous force are studied quantitatively. The nonlinearity of the restoring force and the Froude-Krylov force are found to be important for the FPA responses in all (heave, surge and pitch) directions; the nonlinearity of the viscous force is found to be important in only the heave and pitch directions.

The second part first presents a catenary spread mooring system design of a mobile ocean test berth (MOTB), the Ocean Sentinel (OS) instrumentation buoy, which is developed by the Northwest National Marine Renewable Energy Center (NNMREC) to facilitate ocean test of wave energy converters (WECs). Then the OS mooring design, which is similar to a conventional WEC point absorber mooring system, is evaluated through both field test analysis and quasi-static analysis: the field test analysis is based on the extensive data of

the OS positions, mooring tensions on the OS and environmental conditions of waves, wind and current, collected during the 2013 field test of the OS mooring system; the quasi-static analysis is based on the analytical catenary equations of mooring chains. Both global characteristics and survivability characteristics of the mooring system are evaluated: the global characteristics include the influence of the OS excursion to mooring tension, positional distribution of the OS, directional control of the OS and environmental contributions of waves, current and wind to mooring tensions; the survivability characteristics include the anchor movability and strength capacities of mooring. Because anchor movement occurred near the end of the field test, a systematic procedure of designing a mooring system with adequate anchor holding capacity is developed and applied to design a new OS mooring system.

In the third part, first, the accuracies of a fully coupled method based numerical model in predicting the mooring tensions of the OS mooring system and the OS positions are validated by comparing the numerical results to the field data collected during the 2013 OS field test. Then, the anchor movability, fatigue damage and extreme mooring tension of the OS mooring system are investigated using the mooring tensions predicted by the numerical model. The results of the above studies are summarized as follows: (1) The numerical model provides accurate predictions of the mooring tensions and OS positions under harsh environmental conditions; (2) When the OS drifted significantly near the end of the field test, the bow, port and starboard anchors were likely not dragged, dragged significantly and dragged slightly, respectively; (3) The fatigue damages of mooring lines are predicted for environmental conditions from low to high sea states; and (4) The strengths of mooring

lines in the original mooring design are adequate compared to the predicted extreme mooring tensions.

©Copyright by Junhui Lou
March 22, 2017
All Rights Reserved

Numerical Simulation, Laboratory and Field Experiments, Analysis and Design of Wave
Energy Converter and Mooring System
by
Junhui Lou

A DISSERTATION

submitted to

Oregon State University

in partial fulfillment of
the requirements for the
degree of

Doctor of Philosophy

Presented March 22, 2017
Commencement June 2017

Doctor of Philosophy dissertation of Junhui Lou presented on March 22, 2017.

APPROVED:

Major Professor, representing Civil Engineering

Head of the School of Civil and Construction Engineering

Dean of the Graduate School

I understand that my dissertation will become part of the permanent collection of Oregon State University libraries. My signature below authorizes release of my dissertation to any reader upon request.

Junhui Lou, Author

ACKNOWLEDGEMENTS

The author expresses sincere appreciation to his major advisor Prof. Solomon Yim. He walked with me throughout my journey of PhD study with great advises and patience. I am grateful that he holds on his student and continues providing help even many times I was so slow in progress. In addition to that, his professionalism in research, his broad knowledge, and his training in critical thinking and academic writing benefits me greatly.

I express my appreciation to the members of my committee Prof. Annette von Jouanne, Matthew Evans and Andre R. Barbosa who offer advices and reviews for my research works. Appreciate that Prof. Jennifer Field is interested in my research topic and willing to be my Graduate Council Representative. I also express my appreciation to my previous committee members: Prof. Robert Higdon, Michael Scott, Sourabh Apte and John Baham. Thanks to Prof. Ye Li who provides inspiring thoughts and experimental data for my research of the floating pointer absorber. Thanks to Dr. Ean Amon and Prof. Annette von Jouanne, who provide comments, experimental data and numerical tool for my research of the Ocean Sentinel mooring.

Thanks to the OSU computing system staffs Paul Montagne, Jordan Jones, Michael Sander and Stephen Cleveland for their continuous supports in my usage of the high-performance computing platforms and software tools.

Thanks to my fellow graduate students Ali Mohtat, Ravi Challa, Joshua Baker, Yisen Guo, Tao Xiang and Ming Chen. Thanks to my best friend Minjie Zhu and other dear friends in Corvallis Chinese Christian Church.

Thanks to my lovely wife Wei Shen, my two sons Timothy and Jeremiah Lou, my parents, my parents in law and my brother.

Partial financial support from the Department of Energy Grant No. DE-FG36-08GO18179-M001 is gratefully acknowledged.

CONTRIBUTION OF AUTHORS

Dr. Annette von Jouanne contributed directly to the writing on the background of the Mobile Ocean Test Berth project in Section 3.3.

TABLE OF CONTENTS

	<u>Page</u>
1. General Introduction.....	1
1.1 Introduction.....	1
1.2 Scientific contributions of the dissertation.....	5
2. Prediction of Nonlinear Response of a Floating Point Absorber under Large- Amplitude Waves Using Navier-Stokes and Potential Flow Models.....	8
2.1 Abstract.....	8
2.2 Introduction.....	9
2.3 Numerical Models and Solution Procedures.....	13
2.3.1 The ALE NS solver with penalty method coupling algorithm	13
2.3.2 The ICFD NS solver with kinematic coupling algorithm.....	14
2.3.3 Nonlinear potential flow solver	15
2.4 WEC Dynamic Wave Flume Experiment.....	16
2.5 Numerical Modeling and Simulation of scaled FPA Response	17
2.5.1 Simulations using the ALE NS solver	17
2.5.2 Simulations using the ICFD NS solver.....	21
2.5.3 Simulations using the nonlinear potential flow solver.....	23
2.6 Results and Discussion.....	25
2.6.1 Performances of the three numerical solvers	25

TABLE OF CONTENTS (Continued)

	<u>Page</u>
2.6.2 Quantitative analysis of the nonlinear wave force components and the viscous force	31
2.7 Concluding Remarks	36
2.8 Acknowledgements	39
2.9 References	39
3. Evaluation of a Catenary Spread Mooring System Design of a Wave Energy Converter Test Platform through both Field Test Study and Quasi-Static Analysis	42
3.1 Abstract	42
3.2 Introduction	43
3.3 Background of the Mobile Ocean Test Berth Project	46
3.4 The 2013 Field test of OS Mooring System.....	48
3.4.1 Properties of the OS hull.....	48
3.4.2 The OS mooring system design	50
3.4.3 Field test measurements and a notable event.....	52
3.5 Quasi-Static Analysis of Catenary Mooring Chains	54
3.6 Global Characteristics of the OS Mooring System	58
3.6.1 Influence of OS excursion on mooring tension	58
3.6.2 Position distribution of the OS.....	64

TABLE OF CONTENTS (Continued)

	<u>Page</u>
3.6.3 Directional control of the OS	65
3.6.4 Wave, current and wind influences on mooring tensions	66
3.7 Survivability Characteristics of the OS Mooring System	70
3.7.1 Quasi-static analysis of anchor movability	70
3.7.2 Strength capacities of mooring lines	73
3.8 A Systematic Procedure of Mooring Design for Anchor Movement Prevention	73
3.9 Conclusion remarks	80
3.10 Acknowledgements	82
3.11 References	83
4. Dynamic Analysis and Field Test Evaluation of the Catenary Spread Mooring System Design of a Wave Energy Converter Test Platform.....	86
4.1 Abstract	86
4.2 Introduction	87
4.3 Numerical Model Based on the Fully Coupled Method	90
4.4 Numerical Model Validation through the Ocean Sentinel (OS) Field test	93
4.4.1 The OS mooring system field test.....	93
4.4.2 Numerical simulations	95

TABLE OF CONTENTS (Continued)

	<u>Page</u>
4.4.3 Results.....	105
4.5 Mechanics of Anchor Movement.....	117
4.6 Fatigue Damage Estimation	121
4.6.1 Fatigue properties and accumulation rule	122
4.6.2 Specification of statistical waves, wind and current conditions	122
4.6.3 Predicted fatigue damages for polyester lines	124
4.7 Extreme Mooring Tension Estimation	126
4.7.1 Design tension.....	126
4.7.2 Specification of extreme waves, wind and current conditions	127
4.7.3 Predicted extreme mooring tensions for polyester line and mooring chain	132
4.8 Conclusion remarks.....	133
4.9 Acknowledgements	135
4.10 References	136
5. General conclusions.....	139
Bibliography	148
Appendices.....	154

LIST OF FIGURES

<u>Figure</u>	<u>Page</u>
Figure 2-1. The one-body FPA system	16
Figure 2-2. Full scale geometries of the FPA experimental and the ALE (ICFD) NS solver models	18
Figure 2-3. Geometries of water and air domain in the ALE NS solver	19
Figure 2-4. Structure and fluid mesh in the ALE NS solver.....	20
Figure 2-5. Dimensions of the water and air domains in the ICFD NS solver	21
Figure 2-6. Structure and fluid mesh in the ICFD NS solver	22
Figure 2-7. Geometries of the FPA models for the experiment and the nonlinear potential flow solver	24
Figure 2-8. Comparison of response amplitudes of the three solvers and experimental data.....	26
Figure 2-9. Comparison of the experimental pitch response of the FPA and the predicted pitch responses using the ALE NS solver and the potential flow solver at wave period $T=12.5s$	29
Figure 2-10. Comparisons of the individual inviscid wave force components, the viscous force and the total force	33
Figure 3-1. Geometry of Ocean Sentinel (photos by Dan Hellin)	49
Figure 3-2. Plan view of the 2013 Ocean Sentinel mooring system.....	51
Figure 3-3. Side view of the 2013 Ocean Sentinel mooring system.....	51
Figure 3-4. GPS positions of the Ocean Sentinel from 07/30 to 09/22	54
Figure 3-5. Geometric parameters and forces of the OS mooring system.....	55
Figure 3-6. Quasi-static relationship between the top horizontal force F_{th} and excursion D of the mooring chains (add stage C)	58
Figure 3-7. Mean mooring tensions of the bow, port and starboard lines with respect to Ocean Sentinel positions before the significant OS drift.....	59

LIST OF FIGURES (Continued)

<u>Figure</u>	<u>Page</u>
Figure 3-8. The relationship between the mean mooring tension and OS excursion compared to the quasi-static tension-excursion curve of the OS	61
Figure 3-9. Means, maximums and standard deviations of mooring tensions with respect to OS excursions	63
Figure 3-10. Number of occurrences of the Ocean Sentinel positions and watch circle ..	64
Figure 3-11. Time history of the OS heading direction	66
Figure 3-12. Directional distribution of waves, current and wind during the field test of the Ocean Sentinel	67
Figure 3-13. Correlation between environmental conditions and maximum mooring tensions for every 20 minutes	69
Figure 3-14. The quasi-static ratio (r_a) of effective force to anchor resistance with respect to the mooring tension on the OS (F_o)	72
Figure 3-15. Mooring configurations of six and three legs	77
Figure 4-1. Finite element discretization of a slender structure (Orcina, 2009)	91
Figure 4-2. Plan view of the three-legs mooring system of the Ocean Sentinel.....	94
Figure 4-3. Side view of the three-legs mooring system of the Ocean Sentinel.....	94
Figure 4-4. GPS positions of the Ocean Sentinel from 07/30 to 09/22 and four typical positions (a, b, c and d) where the Ocean Sentinel was close to or outside its position boundary	96
Figure 4-5. Zoom in view of three typical positions (b, c and d) of the Ocean Sentinel ..	98
Figure 4-6. Wave spectrum at scenario C	100
Figure 4-7. Current speed profile along water depth at scenario C	101
Figure 4-8. Comparison between the numerical excursion-tension curve and the experimental excursion-tension curve with recorded anchor position for individual bow, port and starboard mooring lines	102

LIST OF FIGURES (Continued)

<u>Figure</u>	<u>Page</u>
Figure 4-9. Calculation of horizontal distances from Ocean Sentinel to the bow, port and starboard anchors based on the numerical excursion-tension curves and average measured mooring tensions acting on the Ocean Sentinel at scenarios A and B.....	103
Figure 4-10. Estimation of anchor positions using the calculated horizontal distances from the Ocean Sentinel to the bow, port and starboard anchors	104
Figure 4-11. Comparison between the numerical excursion-tension curve and the experimental excursion-tension curve with adjusted anchor position for individual bow, port and starboard mooring lines	105
Figure 4-12. Comparison of power spectral densities between the predicted and measured mooring tensions	113
Figure 4-13. Super-harmonic response of the predicted mooring tensions of the port line at Scenario D, when there is no additional linear damping in the horizontal directions of the port surface buoy.....	114
Figure 4-14. Comparison of measured and numerical positions of Ocean Sentinel at four scenarios (a, b, c and d).....	116
Figure 4-15. Time history of the ratio r_a for the bow, port and starboard anchors	119
Figure 4-16. Sensitivity study of r_a with respect to friction coefficient c	121
Figure 4-17. Fatigue damages per hour of field measurements and numerical predictions	125
Figure 4-18. Extreme values of significant wave height with return periods of 10 and 100 years at the position of NDBD buoy 46050 (located 30 km west of the NETS).....	129
Figure 4-19. Extreme values of average wind speed with return periods of 10 and 100 years at NDBD buoy 46050 (located 30 km west of the NETS)	130
Figure 4-20. Extreme values of current speed with return period of 10 years at the position of NH10 (located 13 km east of the NETS).....	131
Figure 5-1. Schematics of Initial Ocean Sentinel Mooring Design (AXYS, 2012)	160
Figure 5-2. Time history of the average and maximum tension of the bow, port and starboard mooring line from 07/30 to 09/22, and the typical times with large mooring tensions	164

LIST OF FIGURES (Continued)

<u>Figure</u>	<u>Page</u>
Figure 5-3. Time history of significant wave height, current speed and wind speed during the whole deployment of Ocean Sentinel (07/30-10/03)	166
Figure 5-4. Relationship between current conditions (speed and direction) and Ocean Sentinel positions	168
Figure 5-5. Relationship between wind conditions (speed and direction) and Ocean Sentinel positions	169
Figure 5-6. Relationship between wave conditions (wave height) and Ocean Sentinel positions	170
Figure 5-7. Angle of attack definition.....	173
Figure 5-8. Wind drag coefficients at scenario a, b, c and d.....	173
Figure 5-9. Water drag coefficient at scenario a, b, c and d	174

LIST OF TABLES

<u>Table</u>	<u>Page</u>
Table 2-1. Mass properties of the one-body FPA model in the experiment	16
Table 2-2. Drag coefficients for the floater, spar and plate of the FPA.....	25
Table 2-3. Ratios of the amplitudes of the nonlinear restoring force to the amplitudes of the linear restoring force in the heave and pitch directions	35
Table 2-4. Ratios of the amplitudes of the nonlinear Froude-Krylov force to the amplitudes of the linear Froude-Krylov force in the surge, heave and pitch directions ...	35
Table 2-5. Comparison of linear and nonlinear motion responses in the surge, heave and pitch directions.....	36
Table 3-1. Dimensions and mass properties of the Ocean Sentinel.....	49
Table 3-2. Ratios of maximum tension to mooring line strength	73
Table 3-3. Specified extreme environmental conditions	75
Table 3-4. Extreme environmental conditions in the original design, field test and statistical estimation.....	76
Table 3-5. Selected new mooring configurations	77
Table 3-6. Initial horizontal excursions of mooring anchors relative to the OS.....	78
Table 3-7. Maximum of instantaneous effective force for each new mooring configuration	79
Table 3-8. Mooring anchor design for the optimum mooring configuration #1.....	79
Table 4-1. Dimensions and mass properties of the Ocean Sentinel.....	95
Table 4-2. Modeling details of mooring components	95
Table 4-3. Environmental conditions at scenarios of A, B, C and D.....	99
Table 4-4. Comparison of measured and predicted mooring tensions acting on the Ocean Sentinel at four scenarios (A, B, C and D)	107
Table 4-5. Accuracy of the fully coupled method in predicting mooring line tensions .	110
Table 4-6. Statistics of the ratio (ra) of instantaneous effective force to static resistance	118

LIST OF TABLES (Continued)

<u>Table</u>	<u>Page</u>
Table 4-7. Summary of specified statistical environmental conditions at the NETS (whole year)	123
Table 4-8. Probabilities of occurrence for specified statistical environmental conditions	123
Table 4-9. Values of factor a with respect to the number of simulations	127
Table 4-10. Simulated extreme environmental conditions	132
Table 4-11. Design tensions and strengths of the polyester line and mooring chain.....	133
Table 5-1. Drag coefficients for the FPA.....	157

LIST OF APPENDICES

<u>Appendix</u>	<u>Page</u>
Appendix A Drag coefficient C_d and eddy-making damping coefficient C_D for the FPA model in the nonlinear potential flow solver	155
Appendix B Calculation the hydrostatic force and the Froude-Krylov force	158
Appendix C Schematics of the initial Ocean Sentinel mooring design	160
Appendix D Calculation of the reserved capacity C_r with respect to the horizontal force at the top end of the mooring chain F_{th}	162
Appendix E Measured mooring tensions with respect to time	163
Appendix F Measured environmental conditions	165
Appendix G Relationship between environmental conditions and Ocean Sentinel positions	167
Appendix H Wind and current drag coefficients	173

Numerical Simulation, Laboratory and Field Experiments, Analysis and Design of Wave Energy Converter and Mooring System

CHAPTER 1

1. General Introduction

1.1 Introduction

Wave energy converters (WECs), which harvest energy from the ocean via various mechanisms (e.g., oscillation or rotation), have been developing progressively toward commercialization over the last decades. There are generally two categories of WECs, the first are the floating ones, which include point absorber, attenuator, rotating mass and bulge wave devices; and the second are those mounted on seabed or shore banks including submerged pressure differential, oscillating wave surge converter, oscillating water column and overtopping/terminator devices (EMEC, 2014).

For floating WECs, their hydrodynamic response and mooring system behavior are two major areas of research and development. To study the hydrodynamic response of the floating WEC, a variety of numerical models (a linear potential flow model, a nonlinear potential flow model and a Navier-Stokes model) have been introduced to calculate the wave force on structure based on different wave conditions. The linear potential flow model was used for the floating WEC under small-amplitude waves, where the wave force behaves linearly; the nonlinear potential flow model and the Navier-Stokes model were used for the floating WEC under moderate-amplitude waves, where the wave force behaves nonlinearly.

To predict the hydrodynamic response, different algorithms of wave force calculation are used in the three numerical models, which are summarized as follows: (1) The linear potential flow model assumes that a total (inviscid) wave force on the structure is a superposition of four linearized inviscid wave force components: a hydrostatic force, a Froude-Krylov force, a radiation force and a diffraction force; (2) The nonlinear potential flow model also assumes that the total (inviscid) wave force is the superposition of the four wave force components. However, part or all of them are calculated nonlinearly (Babarit et al., 2009; Gilloteaux et al., 2008; Guérinel et al., 2011; Merigaud et al., 2012; Rogne, 2014; Zurkinden et al., 2014); and (3) The NS model calculates only one wave force on the structure, which is called the fully nonlinear wave force (including viscous effects), through solving the NS equations of a fluid domain (Agamloh et al., 2008; Bhinder, 2009; Finnegan and Goggins, 2012; Omidvar et al., 2013; Westphalen et al., 2010; Yu and Li, 2013).

In Chapter 2 of this dissertation, the accuracies of two NS solvers and one nonlinear potential solver in predicting the highly nonlinear hydrodynamic responses of a floating point absorber (FPA) under large-amplitude wave excitations are validated through comparing numerical predictions with laboratory experimental measurements. The strong coupling algorithms in these two NS solvers, which are necessary for calculating the strong interaction between the floating FPA and its surrounding large amplitude waves, are presented. The magnitudes of the nonlinear wave force components and the viscous force calculated by the nonlinear potential flow solver are quantified.

Besides the hydrodynamic response studies of WECs, the mooring system behaviors of WECs have been studied through experiments, among which many have focused on wave tank tests while a few have focused in field tests. In the experimental studies based on wave tank tests, the following WEC mooring characteristics were examined: the dynamic tensions of mooring lines (Ambühl et al., 2014; Hald and Frigaard, 2001; Harnois et al., 2015; Martinelli et al., 2010; Palm et al., 2013; Parmeggiani et al., 2013; Wolf, 2012), the damping effect of a single catenary line (Johanning et al., 2007) and the influences of mooring systems on the motion responses of WECs (Ruiz-Minguela et al., 2008; Zanuttigh et al., 2013).

Compared to the number of wave tank tests, there are fewer field tests because of their higher costs and operational difficulties. Additionally, only a few WEC devices have been mature enough to reach the stage of ocean test. However, the field test has its unique advantage of test a prototype WEC in real ocean conditions with waves, wind and current. In the experimental studies based on field tests, their works are described as follows: the relationship between mooring tensions and significant wave heights was discussed based on a field test of the CALM (Catenary Anchor Leg Mooring) system of the Wave Dragon overtopping device (Kofoed et al., 2006); the mooring line fatigue damage, anchor movement and relationship between wave conditions and extreme mooring tensions, were studied based on a field test of a three leg catenary mooring of an instrumentation buoy at the South West Mooring Test Facility (SWMTF) (Thies et al., 2014; Harnois et al., 2012; Harnois et al., 2013); and the field test of a multi-catenary spread mooring of the OCEANTEC WEC was described in Salcedo et al. (2009).

In the above field test studies the following were not discussed: (1) influence of WEC excursion on mooring tension; (2) importance of dynamic mooring tension compared to mean mooring tension; (3) influences of wind and current conditions on mooring tensions; and (4) a procedure of mooring design to prevent anchor movement.

In Chapter 3, the field test of a multi-body catenary spread mooring system of a mobile ocean test berth (MOTB), the Ocean Sentinel, which is developed by the Northwest National Marine Renewable Energy Center (NNMREC) to facilitate ocean test of WECs, is presented. Then global characteristics and survivability characteristics of the OS mooring design, which is similar to a conventional WEC point absorber mooring system, are evaluated through both field test analysis and quasi-static analysis: the field test analysis is based on the extensive data of the OS positions, mooring tensions on the OS and environmental conditions of waves, wind and current, collected during the 2013 field test of the OS mooring system; the quasi-static analysis is based on the analytical catenary equations of mooring chains. As the OS drifted significantly away from its position domain near the end of the OS field test, the anchor resistance was not adequate in the original mooring design. A systematic procedure of designing a new mooring system with adequate anchor resistance is developed and applied to design a new mooring configuration with the smallest maximum of effective force.

In addition to the experimental studies of WEC mooring systems, numerical simulations based on the fully coupled method have been used to study the WEC mooring systems. To validate the accuracy of the fully coupled method for floating WECs, wave tank tests were conducted for a catenary mooring line of a cylindrical drum buoy (Johanning et al., 2007) and a three-legs catenary mooring system of an instrumented buoy (Harnois et al., 2015).

However, there are some limitations in these two wave tank tests: in Johanning et al. (2007), the displacement of the drum buoy was prescribed, which means that the mooring system does not affect the motion of the drum buoy; in Harnois et al. (2015), only waves were generated in the test (no wind and current).

Comparing to wave tank tests, field tests of WEC mooring systems can validate the fully coupled method in true ocean environments with waves, wind and current. In Harnois et al. (2015), a field test was used to validate the fully couple method. However, large differences between predicted and measured mooring tensions were found because of the unknown anchor position.

In Chapter 4, first, the accuracies of a fully coupled method based numerical model in predicting the mooring tensions of the OS mooring system and the OS positions are validated by comparing numerical predictions to the field data collected during the 2013 OS field test. Then, the anchor movability, fatigue damage and extreme mooring tension of the OS mooring system are evaluated using the mooring tensions predicted by the numerical model.

1.2 Scientific Contributions of the Dissertation

In Chapter 2, the performances of two finite element (FE) NS solvers and one boundary-element nonlinear potential flow solver in predicting the responses of a locked-body FPA (the same FPA as (Yu and Li 2013)) under large amplitude regular waves are studied to determine their predictive accuracies and computational costs. Using the nonlinear potential flow, nonlinear effects of the individual Froude-Krylov force, restoring force and viscous force are analyzed quantitatively.

In Chapter 3, the global characteristics and survivability characteristics of the Ocean Sentinel (OS) catenary spread mooring system design are evaluated through both field test analysis and quasi-static analysis: the field test analysis is based on the extensive data of the OS positions, mooring tensions on the OS and environmental conditions of waves, wind and current, collected during the 2013 field test of the OS mooring system; the quasi-static analysis is based on the catenary equations of mooring chains. The global characteristics of the mooring system include the influence of the OS excursion to mooring tension, positional distribution of the OS, directional control of the OS and environmental contributions of waves, current and wind to mooring tensions. The survivability characteristics of the mooring system include the anchor movability and strength capacities of mooring lines. Because anchor movement occurred near the end of the field test, a systematic procedure of designing a mooring system with adequate anchor resistance is developed and applied to design a new OS mooring system.

In Chapter 4, the accuracies of a fully coupled method based numerical model in predicting the mooring tensions of the OS mooring system and the OS positions are validated by comparing numerical predictions to the field data collected during the 2013 OS field test. Then, the anchor movability, fatigue damage and extreme mooring tension of the OS mooring system are evaluated using the mooring tensions predicted by the numerical model. The results of the above studies are summarized as follows: (1) The numerical model provides accurate predictions of the mooring tensions and OS positions under harsh environmental conditions; (2) When the OS drifted significantly near the end of the field test, the bow, port and starboard anchors were likely not dragged, dragged significantly

and dragged slightly, respectively; (3) The fatigue damages of mooring lines are predicted for environmental conditions from low to high sea states; and (4) The strengths of mooring lines in the original mooring design are adequate compared to the predicted extreme mooring tensions.

CHAPTER 2

2. Prediction of Nonlinear Response of a Floating Point Absorber under Large-Amplitude Waves Using Navier-Stokes and Potential Flow Models

Junhui Lou ^a, Solomon Yim ^a and Ye Li ^b

^a Oregon State University and ^b Shanghai Jiao Tong University

2.1 Abstract

In this study, performances of a finite-element explicit Navier-Stokes (NS) solver, a finite-element implicit NS solver and a boundary-element nonlinear potential flow solver in predicting the highly nonlinear hydrodynamic responses of a floating point absorber (FPA) under large-amplitude waves are studied. The two NS solvers calculate coupled fluid structure interaction (FSI) including fully nonlinear inviscid and viscous forces. The nonlinear potential flow solver calculates individual (inviscid) wave force components (a Froude-Krylov force, a radiation force, a diffraction force and a hydrostatic force) and empirical viscous force. Comparing numerical results to laboratory experimental measurements, the two NS solvers and the nonlinear potential flow solver are found to be capable of providing accurate predictions of the nonlinear motion responses of the FPA. FSI coupling algorithms and computational costs of these three solvers are evaluated. Based on the results of the nonlinear potential flow solver at different wave periods, the individual wave force components and the viscous force are studied quantitatively. The nonlinearity of the restoring force and the Froude-Krylov force are found to be important for the FPA responses in all (heave, surge and pitch) directions; the nonlinearity of the viscous force is found to be important in only the heave and pitch directions.

Keywords: Wave energy converter, floating point absorber, hydrodynamic response, potential flow model, Navier-Stokes model, nonlinear wave force, viscous force, fluid-structure interaction

2.2 Introduction

Wave energy converters (WECs), which have a promising potential to utilize abundant ocean renewable wave energy resources and provide cost-efficient electricity supply, have raised significant research interests worldwide during the last decades. Among the various types of WECs, a floating WEC operates at or near ocean surface and generates power through wave excited motions.

To study the hydrodynamic response of the floating WECs, a variety of numerical models (a linear potential flow model, a nonlinear potential flow model and a Navier-Stokes model) have been introduced to calculate the wave force on structure based on different wave conditions. The linear potential flow model was used for the floating WEC under small-amplitude waves, where the wave force behaves linearly; the nonlinear potential flow model and the Navier-Stokes model were used for the floating WEC under moderate-amplitude waves, where the wave force behaves nonlinearly.

The linear potential flow model assumes that a total (inviscid) wave force on the structure is a superposition of four linearized inviscid wave force components: a hydrostatic force, a Froude-Krylov force, a radiation force and a diffraction force. The linear hydrostatic force and the Froude-Krylov force are calculated through integrating the static fluid pressure and the dynamic fluid pressure over the mean wetted body surface of the WEC respectively.

The linear radiation force and linear diffraction force are calculated by solving the radiation potential ϕ_r and the diffraction potential ϕ_d at the mean wetted body surface respectively, using a boundary element method (BEM).

The nonlinear potential flow model also assumes that the total (inviscid) wave force is the superposition of the four wave force components. However, part or all of them are calculated nonlinearly:

- In the references of Babarit et al. (2009), Gilloteaux et al. (2008), Guérinel et al. (2011), Merigaud et al. (2012), Rogne (2014) and Zurkinden et al. (2014), the hydrostatic force and the Froude-Krylov force are calculated nonlinearly through integrating the static and dynamic fluid pressure over the instantaneous wetted body surface of the WEC respectively; the radiation force and the diffraction force are calculated linearly as in the linear potential flow model.
- In the references of Bretl (2009) and Sclavounos (2012), all the hydrostatic force, the Froude-Krylov force, the radiation force and the diffraction force are calculated nonlinearly at the instantaneous wetted body surface.

The NS model calculates only one wave force on the structure, which is called the fully nonlinear wave force (including viscous effects), through solving the NS equations of a fluid domain (Agamloh et al., 2008; Bhinder, 2009; Finnegan and Goggins, 2012; Omidvar et al., 2013; Westphalen et al., 2010; Yu and Li, 2013). Among the references, the predicted fully nonlinear wave forces on a fixed WEC (Westphalen et al., 2010) and a WEC with prescribed motions (Omidvar et al., 2013) were validated through experiments; the predicted nonlinear responses of a free moving WEC under focused waves ((Omidvar et

al., 2013)) and two free moving WECs under regular waves (Bhinder, 2009; Yu and Li, 2013) were compared to experimental data.

In addition to the nonlinear inviscid wave force, a viscous force may also contribute to the nonlinear response of WECs. In Rogne (2014) and Zurkinden et al. (2014), the viscous force was calculated by the empirical Morison equation in the nonlinear potential flow model. In Monroy et al. (2010), the viscous force was taken into account through modeling viscous diffracted flow around a buoy using a simplified NS model, while the incident waves were computed based on the potential flow theory. In (Yu and Li, 2013), viscous forces on a one-body floating point absorber (FPA) and a two-body FPA were taken into account automatically through applying the NS model for the whole fluid domain.

Effects of the nonlinear inviscid wave force and the viscous force were discussed in the following two studies through serials of regular wave tests: 1. in Zurkinden et al. (2014), the nonlinear potential flow model was used to predict the nonlinear responses of a moving hemispherical buoy when the nonlinear interaction between the buoy of simple geometry and moderate-amplitude waves (operational wave conditions) was relatively small. The results showed that the viscous force on the buoy was relatively small compared to the inviscid wave force components. 2. in Yu and Li (2013), the NS model was used to model the nonlinear responses of the two FPA systems when nonlinear interactions between the FPAs of complex geometries and moderate-amplitude waves were relatively larger. The nonlinear dynamic responses of the two FPAs were demonstrated through the relationship of: 1. the ratios of the heave response amplitude of the one-body FPA to wave height vary with different wave heights; 2. the ratios of the power take-off (PTO) of the two-body FPA to the square of wave height also vary with different wave heights.

The first major aim of this study is to investigate the performances of the NS models and the nonlinear potential flow model in predicting the highly nonlinear fluid-structure interaction (FSI) where both complex structure geometry and large-amplitude waves (extreme wave conditions) are present. The second major aim is to quantify the nonlinear wave force components and the viscous force using the results of a nonlinear potential flow model.

In the first part of this study, the highly nonlinear responses of the same one-body FPA in Yu and Li (2013) are modeled in heave, surge and pitch directions under large amplitude regular waves. Comparing to the operational wave heights (2 m and 4 m in full scale) in Yu and Li (2013), the wave height in this study is increased to an extreme wave height (10 m in full scale). Two NS solvers based on the finite element method with strong FSI algorithms are introduced (*c.f.* NS solvers in previous studies in the literature which were based on the finite volume ((Agamloh et al., 2008; Bhinder, 2009; Finnegan and Goggins, 2012; Yu and Li, 2013)) and smoothed particle hydrodynamics (SPH) methods (Omidvar et al., 2013)). In addition, a related nonlinear potential flow solver is also used in this study to model the highly nonlinear responses of the FPA. The accuracies and limitations of these three numerical solvers are discussed.

In the second part of this study, the magnitudes of the individual wave force components and the viscous force calculated by the nonlinear potential flow solver are compared to the magnitude of the total force at each wave period; the magnitudes of the nonlinear restoring force and Froude-Krylov force in the time domain are compared to the magnitudes of the linear restoring force and Froude-Krylov force in the frequency domain respectively.

2.3 Numerical Models and Solution Procedures

Three commercial codes are applied in this study: a finite element explicit NS solver using the penalty method coupling algorithm (LSDYNA-ALE), a finite element implicit NS solver using the kinematic coupling algorithm (LSDYNA-ICFD) and a nonlinear potential flow solver (AQWA). The governing equations and fluid-structure interaction coupling algorithms of each solver are described in the following.

2.3.1 The ALE NS solver with penalty method coupling algorithm

The governing equations for the fluid in the ALE NS solver are the compressible NS equations and continuity equations in the Arbitrary Lagrangian Eulerian (ALE) formulation:

$$\rho \left(\frac{\partial u_i}{\partial t} + (u_j - v_j) \frac{\partial u_i}{\partial x_j} \right) = - \frac{\partial p}{\partial x_i} + \frac{\partial}{\partial x_j} \left(\mu \left(\frac{\partial u_i}{\partial x_j} + \frac{\partial u_j}{\partial x_i} \right) - \frac{2}{3} \mu \frac{\partial u_i}{\partial x_i} \delta_{ij} \right) + \rho f_i \quad \text{Eq. (2.1)}$$

$$\frac{\partial \rho}{\partial t} + (u_j - v_j) \frac{\partial \rho}{\partial x_j} + \rho \frac{\partial u_i}{\partial x_i} = 0 \quad \text{Eq. (2.2)}$$

where x_i is the ALE coordinate; t is the time; u_i is the particle velocity; v_i is the velocity of the reference frame; ρ is the fluid density; p is the pressure; μ is the coefficient of viscosity and f_i is the body acceleration.

The governing equations for the structure in this solver are also in the ALE formulation. In such way, the governing equations for the fluid and structure can be solved simultaneously for all unknown variables (a monolithic scheme, which is explicit for this solver).

In FSI coupling, the fluid mesh overlaps the structure mesh. The fluid material, which flows through the fluid mesh, interacts with the structure material, which moves with the structure mesh. The interface of the fluid material is determined by the volume of fluid VOF method.

Through these algorithms the fluid mesh distortion at the FSI interface can be reduced significantly.

The coupling force between fluid and structure is calculated using a penalty method, which applies a resisting force to a pair of adjacent structure and fluid nodes in opposite directions if the structure node penetrates through the fluid node. The magnitude of the resisting force is proportional to the penetration depth. Detailed descriptions of the ALE NS solver and its FSI algorithms can be found in Souli and Benson (2010).

2.3.2 The ICFD NS solver with kinematic coupling algorithm

The governing equations for the fluid in the ICFD NS solver are the incompressible NS equations and continuity equations in the Arbitrary Lagrangian Eulerian (ALE) formulation

$$\rho \left(\frac{\partial u_i}{\partial t} + (u_j - v_j) \frac{\partial u_i}{\partial x_j} \right) = - \frac{\partial p}{\partial x_i} + \mu \frac{\partial^2 u_i}{\partial x_j \partial x_j} + \rho f_i \quad \text{Eq. (2.3)}$$

$$\frac{\partial u_i}{\partial x_i} = 0 \quad \text{Eq. (2.4)}$$

In FSI coupling, the fluid and structure meshes share the same nodes at the interface and are constrained at the same velocity (kinematic contact). The coupling force between fluid and structure is calculated based on ICFD partitioned scheme (the fluid and structure governing equations are solved in two separated solvers). In each time step, the fluid force and structure displacement at the fluid-structure interface are communicated between the fluid and structure solvers iteratively until the convergence of the solutions. For applications where the structure density is close to the fluid density, which is the case for the FPA of this study, the added mass effect (Causin et al., 2005) is significant in the

partitioned coupling and may cause non-convergence solutions. To improve the convergence of the solutions, a stabilization method by Idelsohn et al. (2009) is employed. In this numerical model, the free-surface of the fluid domain is tracked by the level set method.

2.3.3 Nonlinear potential flow solver

The governing equations for the fluid in the nonlinear potential flow solver are the Laplace equation of velocity potential ϕ and the linearized Bernoulli's equation.

$$\nabla^2 \phi = 0 \quad \text{Eq. (2.5)}$$

$$p = -\rho \left(\frac{\partial \phi}{\partial t} + gy \right) \quad \text{Eq. (2.6)}$$

where y is the vertical distance to the water surface.

The governing equation for the structural motion is

$$\mathbf{M}_s \ddot{\mathbf{x}}(t) = \mathbf{F}_r(t) + \mathbf{F}_d(t) + \mathbf{F}_f(t) + \mathbf{F}_h(t) + \mathbf{F}_{vis}(t) + \mathbf{F}_g(t) + \mathbf{F}_m(t) \quad \text{Eq. (2.7)}$$

where $\mathbf{x}(t)$ is the structural displacement vector; t is the time; \mathbf{M}_s is the structural mass matrix; $\mathbf{F}_r(t)$ is the linear radiation force vector; $\mathbf{F}_d(t)$ is the linear diffraction force vector; $\mathbf{F}_f(t)$ is the nonlinear Froude-Krylov force vector; $\mathbf{F}_h(t)$ is the nonlinear hydrostatic force vector; $\mathbf{F}_{vis}(t)$ is the viscous force vector; $\mathbf{F}_g(t)$ is the gravity force vector; and $\mathbf{F}_m(t)$ is the mooring force vector.

The structure and the fluid (waves) motions are coupled through the wave force components and the viscous force calculated in the nonlinear potential flow model.

2.4 WEC Dynamic Wave Flume Experiment

An experiment of a one-body FPA (shown in Figure 2-1) was conducted in the wave tank of University of California, Berkeley (Li et al., 2016). The FPA consisted of three parts: a floater, a submerged bottom plate, and a connecting spar. Because the relative motion between the floater and the bottom plate was locked in large amplitude waves to prevent structural damage, the FPA was built as a locked-body structure. The mass properties of the FPA model in the experiment (conducted in 1/00 scale) are listed in Table 2-1.

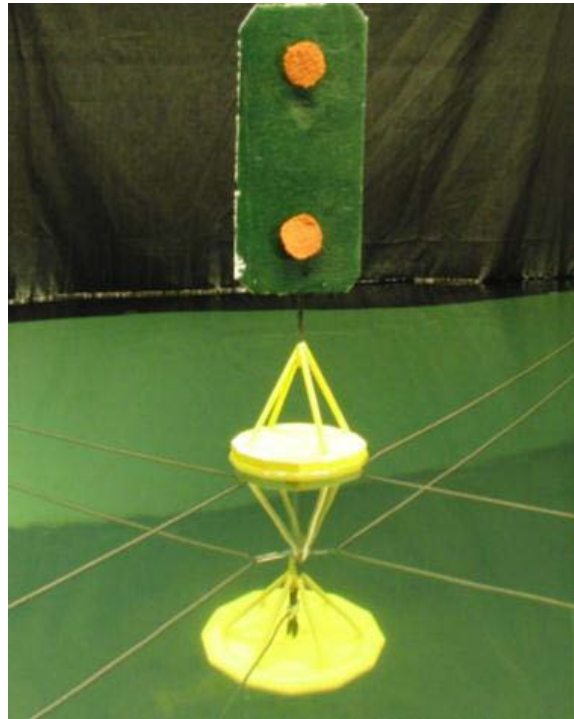


Figure 2-1. The one-body FPA system

Table 2-1. Mass properties of the one-body FPA model in the experiment

Total mass	0.313 kg
Moment of inertia in pitch direction	72.18 kg · cm ²
Center of gravity (COG)	0.23 m below the still water level (SWL)

The FPA mooring system consists of 8 mooring lines, which were arranged in two layers, with a 90-degree angle between adjacent mooring lines in each layer. The stiffness of each mooring line was approximately 0.7 N/m.

Responses of the FPA were tracked by a two-point motion tracking system. Motions of the two tracking points, which are shown as red dots in Figure 2-1, were tracked by one digital camera each. After obtaining the horizontal and vertical motions of the tracking points through post processing the video data, surge, heave and pitch motions at the CG of the FPA were calculated. A series of regular wave tests with 0.1m wave height (10m in full scale) are examined in details in this study.

2.5 Numerical Modeling and Simulation of Scaled FPA Response

2.5.1 Simulations using the ALE NS solver

Surge, heave and pitch motions of the FPA are simulated in full scale using the ALE NS solver. The corresponding full-scale geometries of the experimental FPA model and the ALE NS solver model are shown in Figure 2-2.

.

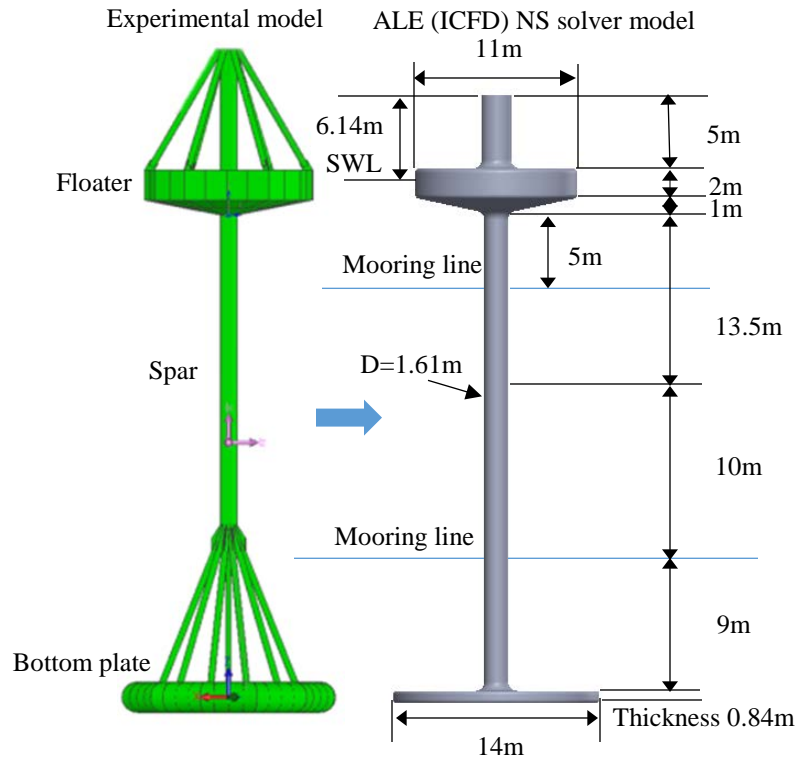


Figure 2-2. Full scale geometries of the FPA experimental and the ALE (ICFD) NS solver models

The geometries of the entire computational (full-scale) domain, which includes the water and air domains, are 40 m wide and 170 m high (see Figure 2-3). The computational zone is two wavelengths long (wavelength $L = 127$ m for wave period $T = 8.8$ s; $L = 345$ m for wave period $T = 14.9$ s) and the damping zone is 1872 m long (equals to four wavelengths of maximum period of $T = 17.6$ s). Note that only half of the computational domain is simulated in the ALE NS model by taking advantage of the symmetric property of the system.

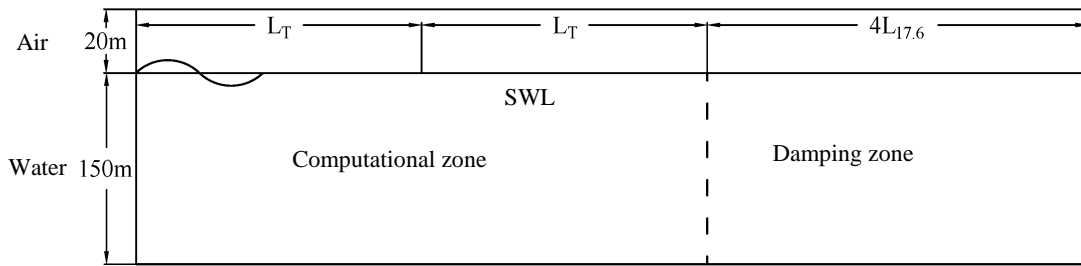


Figure 2-3. Geometries of water and air domain in the ALE NS solver

Incident waves are generated through specifying water particle velocities at the inflow boundary of the water domain, based on the 5th-order Stokes wave theory (Fenton, 1985). Reflected waves are damped out in the damping zone through gradually increasing the mesh size in the wave propagation direction (Park et al., 1999).

As illustrated in Figure 2-4, the structure mesh (modeled by triangular or quadrangular shell elements with an average mesh size of 0.4 m) overlaps the fluid mesh of the water and air domains (modeled by cubic solid elements with the smallest size of 0.5 m). To improve the stability of the penalty coupling method, sharp edges of the FPA are rounded, so that the penetration of the structure mesh into the fluid mesh can be smoothed.

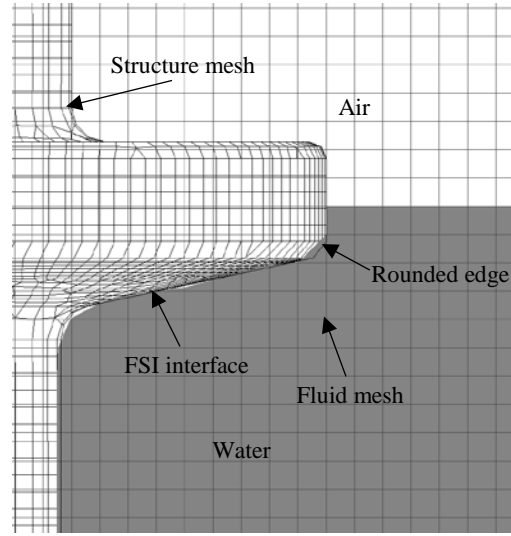


Figure 2-4. Structure and fluid mesh in the ALE NS solver

(Ikeda et al., 1993) indicates that the viscous eddy-making damping is important to the roll responses of floating structures (including ships) that have sharp corners at the bases. Accordingly, the eddy-making damping effect on the pitch response of the FPA, which has sharp edge at the plate, is included in the model as an added damping term in the governing equations of the FPA motions in the pitch direction (Chakrabarti, 2001; Himeno, 1981):

$$F_e = -C_D \dot{\theta} |\dot{\theta}| \quad \text{Eq. (2.8)}$$

where F_e is the generalized eddy-making damping “force”; C_D is the non-dimensional empirical eddy-making coefficient; and θ is the rotation angle (in radians). This damping coefficient is a complex function of the geometry and mass distribution of the FPA that can only be obtained empirically by trial and error. For the FPA considered in this study, a C_D valued of 8×10^8 is found to provide optimal numerical pitch response compared with experimental data.

2.5.2 Simulations using the ICFD NS solver

The geometries of the FPA in the ICFD NS solver are identical to those of the ALE NS solver model. The computational water and air domains are demonstrated in Figure 2-5, with a width of 48 m and a total height of 170 m: the computational zone is two wavelengths long and the damping zone is 2250 m long (equals to 4.8 wavelengths of wave period $T = 17.6$ s).

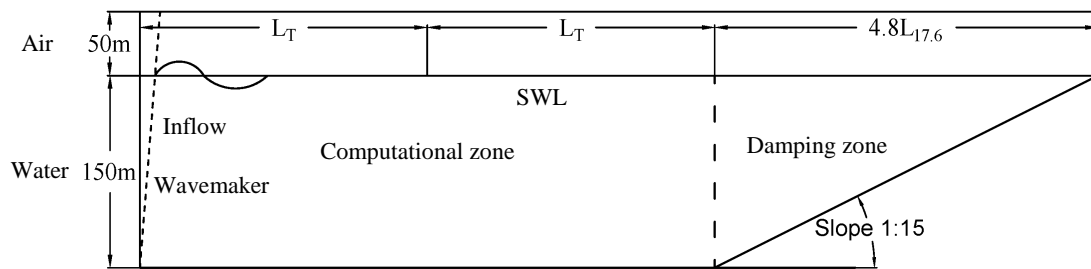


Figure 2-5. Dimensions of the water and air domains in the ICFD NS solver

Incident waves are generated by a flap wavemaker at the inflow boundary. Reflected waves are suppressed in the damping zone through an absorbing beach with a slope of 1:15. Instead of gradually increasing the size of the structured cubic fluid mesh of the ALE NS solver in the wave propagation direction, the absorbing beach is used to damp out reflected waves, because gradually increasing the size of the unstructured tetrahedral fluid mesh of the ICFD NS solver (the corresponding mesh will be described below) in the wave propagation direction is not practical.

As illustrated in Figure 2-6, the FPA is modeled as a rigid body using triangular shell elements in this model with an average mesh size of 0.2 m. The water and air domains are modeled using tetrahedral solid elements (the smallest mesh size is 0.2 m) generated based

on the surface mesh of the structure and the boundary mesh of the water and air domains. The structure mesh shares the same nodes with the fluid mesh at the FSI interface. When the structure mesh moves, the fluid mesh also moves in the ALE algorithm. If the FPA undergoes large motion, large distortion of the fluid mesh would occur near the FSI interface, which induces low accuracy and instability problems. In such case, re-meshing is activated generate a new set of fluid mesh with a new topology.

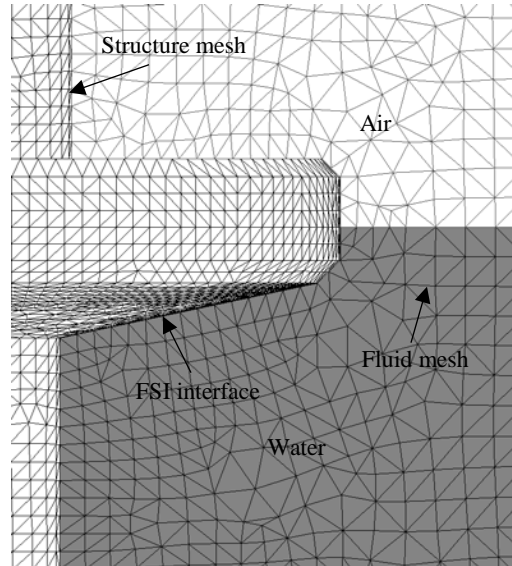


Figure 2-6. Structure and fluid mesh in the ICFD NS solver

In this (ICFD) model, an eddy-making term $F_e = -C_D \dot{\theta} |\dot{\theta}|$ is also added in the governing equations of the FPA motions in the pitch direction with $C_D = 2 \times 10^9$ (in full scale) to improve the predictive accuracy in the pitch response.

2.5.3 Simulations using the nonlinear potential flow solver

2.5.3.1 Modeling setup

The motion responses of the FPA are simulated in the surge, heave and pitch directions in the nonlinear potential flow solver. Figure 2-7 shows the full scale geometries of the experimental FPA model and the nonlinear potential solver model with a computational water domain dimensions of 150 m in depth, 240 m in width and 6,800 m in length which are the exact scaled-up dimensions of the laboratory wave flume. The FPA is modeled using boundary elements, with an average mesh size of 0.3 m.

In the nonlinear potential flow model, the hydrodynamic responses of the FPA are simulated in two steps: first, the linear wave force components and the linear responses of the FPA are calculated in the frequency domain; second, the instantaneous linear and nonlinear wave force components and the nonlinear responses of the FPA are calculated in the time domain.

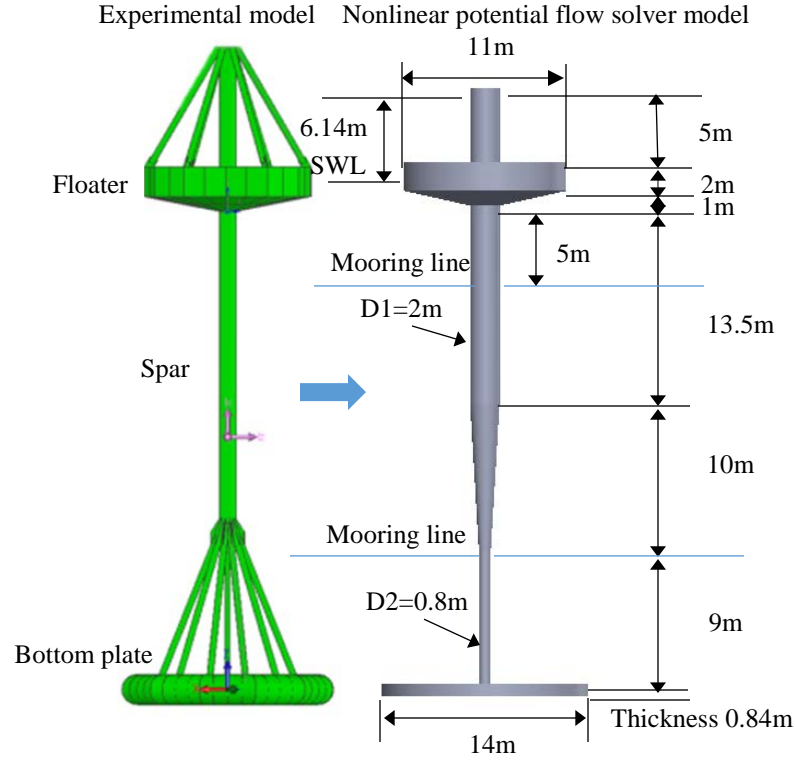


Figure 2-7. Geometries of the FPA models for the experiment and the nonlinear potential flow solver

2.5.3.2 Viscous effects in the heave, surge and pitch directions

In the nonlinear potential flow solver, viscous effects are not included in the governing (potential flow) equations. To take into account the viscous effect in the heave and surge directions, viscous force terms, calculated using the following Morison equation, are included in the governing equations of the FPA motions in the heave and surge directions:

$$F = -\frac{1}{2}\rho C_d A(u_s - u_f)|u_s - u_f| \quad \text{Eq. (2.9)}$$

where ρ is the water density; C_d is the empirical non-dimensional drag coefficient; A is the cross-sectional area of the body perpendicular to the flow direction; u_s is the structural velocity orthogonal to the cross section; and u_f is the undisturbed fluid velocity orthogonal to the cross section.

To calculate the total viscous force on the FPA with a complex geometry, the drag coefficients C_d for the floater, the spar and the plate of the FPA are specified individually in local x' and z' directions. The local x' direction is defined as the direction orthogonal to the spar; the local z' direction is defined as the direction along the spar axis. Table 2-2 lists the drag coefficients C_d for each part of the FPA. Note that KC indicates the Keulegan–Carpenter number.

Table 2-2. Drag coefficients for the floater, spar and plate of the FPA

	Floater		Spar		Plate	
Direction	x'	z'	x'	z'	x'	z'
	$C_d = 0.5$	$C_d = 3$	$C_d = 2$	0	$C_d = 0.5$	$C_d = 8KC^{-0.33}$

To take into account the viscous effect in the pitch direction, an eddy-making term ($F_e = -4 \times 10^9 \times \dot{\theta} |\dot{\theta}|$) is added in the governing equations of the FPA motions in the pitch direction. The drag coefficient C_d and eddy-making damping coefficient C_D are determined according to the references of Bearman et al. (1984), Faltinsen (1990), Graham (1980), Ikeda et al. (1993) and Sarpkaya (1976) (see Appendix A for details).

2.6 Results and Discussion

2.6.1 Performances of the three numerical solvers

2.6.1.1 Accuracy in predicting the highly nonlinear responses of the FPA

The predictive performances of the ALE NS solver, the ICFD NS solver and the nonlinear potential flow solver are evaluated by comparing their corresponding numerical model

predictions to the experimental results in the heave, pitch and surge directions, respectively, as shown in Figure 2-8.

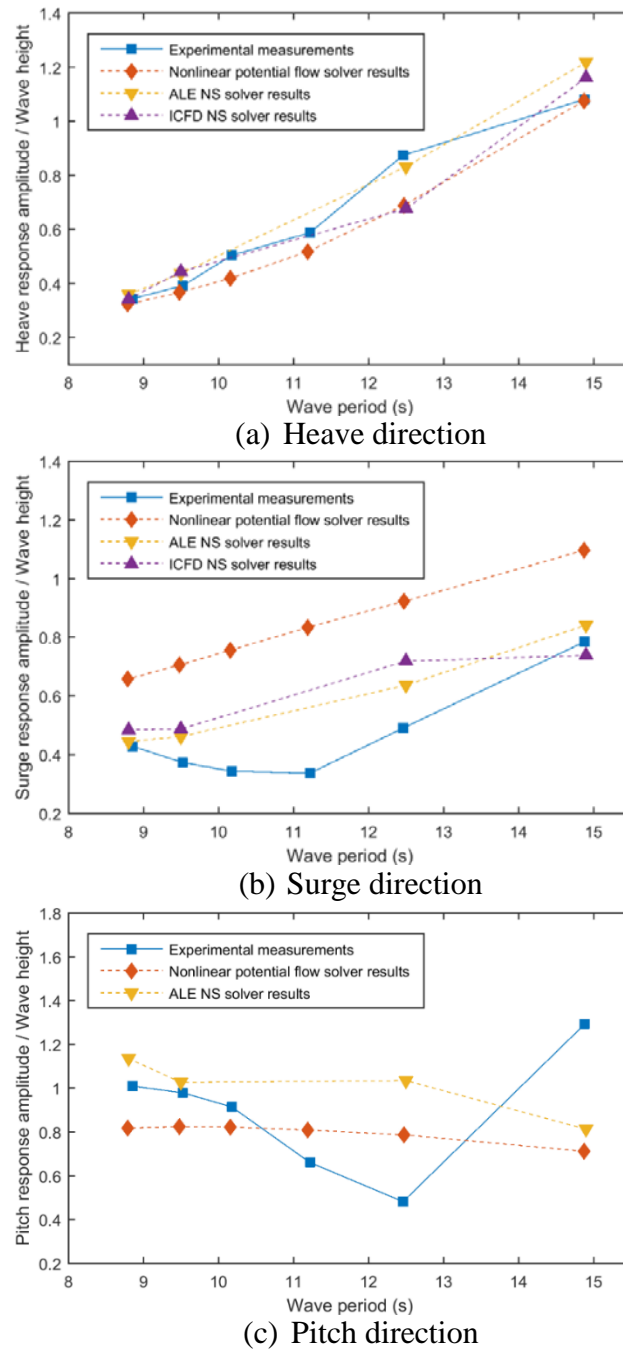


Figure 2-8. Comparison of response amplitudes of the three solvers and experimental data

In the heave direction, the predictive accuracies of the ALE and ICFD NS solvers are close to that of the nonlinear potential flow solver. The averages of the relative differences (for wave periods $T = 8.8, 9.5, 12.5, 14.9$ s) between numerical predictions and experimental data are 8.3%, 10.8% and 8.5% for the ALE NS solver, the ICFD NS solver and the nonlinear potential solver, respectively. The viscous force is computed automatically in the two NS solvers while the viscous force is computed empirically using the Morison equation in the potential flow solver.

In the surge direction, the predictions of the ALE and ICFD NS solvers are more accurate than those of the nonlinear potential flow solver. The averages of the relative differences between numerical predictions and experimental data are 16.1%, 24.0% and 67.4% for the ALE NS solver, the ICFD NS solver and the nonlinear potential solver respectively. Because the surge response of the FPA is mainly contributed by the total inviscid wave force (which will be shown in Section 2.6), the results demonstrate that modeling the fully nonlinear wave force in the two NS solvers significantly improves the prediction accuracies of the FPA surge response, comparing to the nonlinear potential flow solver which models only the individual wave force components.

In the pitch direction, the predictive accuracy of the ALE NS solver is close to that of the nonlinear potential flow solver. The averages of the relative differences between numerical predictions and experimental data are 42.2% and 35.7% for the ALE NS solver and the nonlinear potential solver, respectively. The difference between the ALE NS solver predictions and the experimental results may be attributed to the limitation of the numerical solver in fully calculating the flow separation induced eddy-making force near the edge of the FPA bottom plate. The difference between the nonlinear potential flow solver

predictions and the experimental results may be attributed to the limitation of the empirical eddy-making equation in calculating the eddy-making force in the numerical model. Because the pitch responses of the FPA are sensitive to the stiffness of its two-layer mooring system, part of the differences between the predictions by the two numerical solvers and the experimental results may also be attributed to the difference between the linear mooring stiffness assumptions in the numerical models and the actual (nonlinear) mooring stiffness in the experiment. Additional observations on the predictive performance of the two numerical solvers are summarized as follows:

- The coefficient of the empirical eddy-making equation in the nonlinear potential flow model ($C_D = 4 \times 10^9$) is larger than that in the ALE NS model ($C_D = 8 \times 10^8$). A possible explanation of this difference is that the eddy-making equation in the potential flow model calculates the overall vortex-induced eddy-making force in the pitch direction that cannot be obtained by solving the potential flow equations, while the eddy-making equation in the ALE NS model only compensates the part of vortex-induced eddy-making force that is underestimated in solving the NS equations.
- Both the ALE NS solver and the nonlinear potential flow solver cannot predict the super-harmonic responses of the FPA at certain wave periods. For example, as shown in Figure 2-9, the experimental FPA response has strong super-harmonic component at wave period $T = 12.5$ s while the numerical responses of the ALE NS solver and the potential flow solver are close to harmonic. This phenomenon contributes to the significant overestimation of the pitch response amplitudes of the two numerical solvers at $T = 12.5$ s. The super-harmonic response of the experiment

may be induced by both the nonlinearity of the mooring stiffness in the experiment, which is not included in the numerical solvers, and the super-harmonic component of the generated waves in the experiment.

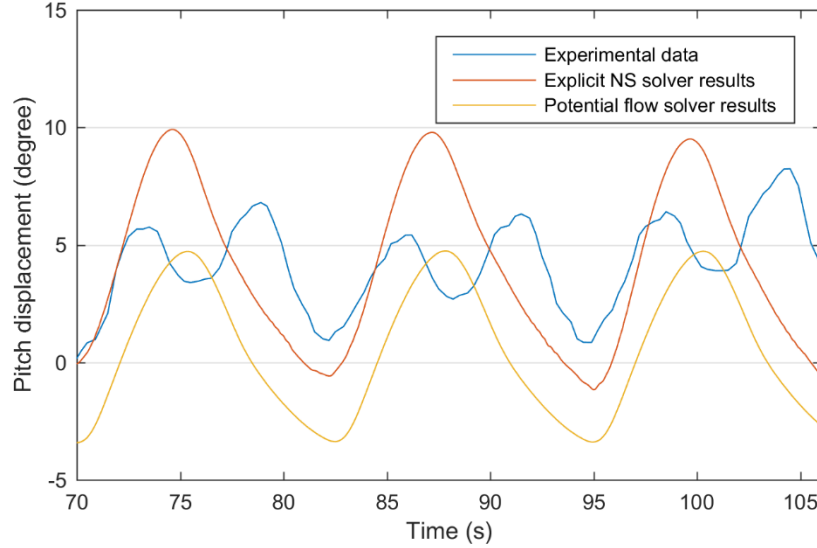


Figure 2-9. Comparison of the experimental pitch response of the FPA and the predicted pitch responses using the ALE NS solver and the potential flow solver at wave period $T=12.5s$

2.6.1.2 Numerical stability of the numerical solvers

Because the FPA has large motions under wave excitations and the density ratio between the FPA and the water is close to unity, the FSI coupling between the FPA and waves can be quite challenging (Badia et al., 2008; Causin et al., 2005). For this type problems, the ICFD NS solver can become less stable than the ALE NS solver because of the following reasons. First, the fluid mesh shares the same nodes with the structure mesh at the FSI interface in the ICFD NS solver, which may induce large fluid mesh distortion when the FPA undergoes large motions especially in the pitch direction. (On the contrary, the fluid

mesh overlaps the structure mesh in the ALE NS solver which prevents large fluid mesh distortion.) Second, the partitioned scheme in solving the fluid and structure equations in the ICFD NS solver is sensitive to the added mass effect (as the FPA density is close to the water density), which may result in non-convergence solutions. (On the contrary, the monolithic scheme is implemented in the ALE NS solver.)

2.6.1.3 Computational efficiency

To examine the computational performance dependence of the ALE and ICFD NS solver on the corresponding numbers of elements in simulations of different wave periods, the following computational times and numbers of elements are presented for a representative wave period ($T = 12.5$ s) for the three numerical solvers.

The computational costs of the ALE NS solver and ICFD NS solver are 1.0 hour per second and 1.7 hour per second, respectively for simulations running on 15 cores of a workstation mounted with two 8 core Intel Xeon CPUs (E5-2687W).

The computational cost of the ICFD NS model is 1.7 times as large as the computational cost of the ALE NS model, even the time step of the implicit ICFD NS model (0.02s in full scale) is about 70 times as large as the time step of the explicit ALE NS model (0.00028s in full scale). This is because of the following reasons: first, the number of fluid elements in the ICFD NS model (12,500,000), is about 7 times as large as the number of fluid elements in the ALE NS model (1,800,000); second, the re-meshing during the simulation of the ICFD NS model, which is conducted in only one core, is computationally expensive. Note that the computational cost of the ALE NS solver is reduced to 10% of its original value through modeling the FPA in the full scale (comparing to the experiment scale of

1/100). This is because in the full scale, the time step of the explicit solver, which is controlled by the mesh size divided by the sound speed in the water, is increased by a factor of 100, while the simulation time is only increased by a factor of 10.

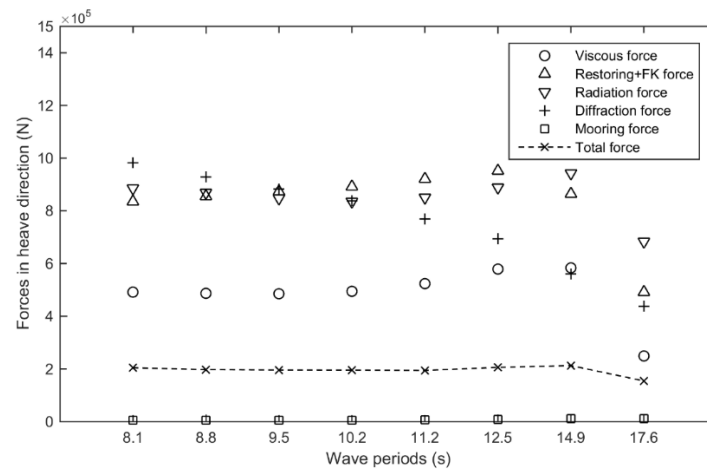
The computational cost using the ICFD NS solver may be significantly reduced when the numerical non-reflecting boundary, which is currently under development, will be implemented in the future version of this solver. In such case, the absorbing beach in the ICFD NS models of this study can be replaced by the non-reflecting boundary and the number of fluid elements can be reduced significantly.

The computational cost of the nonlinear potential flow solver simulation (the total number of elements is 9616) is much smaller than the computational costs of the ALE and ICFD NS solver simulations. Recall that the nonlinear potential flow simulation is conducted in two steps: the first step is the frequency domain simulation; the second step is the time domain simulation. For a study of one wave period, the frequency domain simulation takes about half an hour to run on a laptop with Intel Core i3 CPU; the time domain simulation takes about 3 minutes to run on the same laptop.

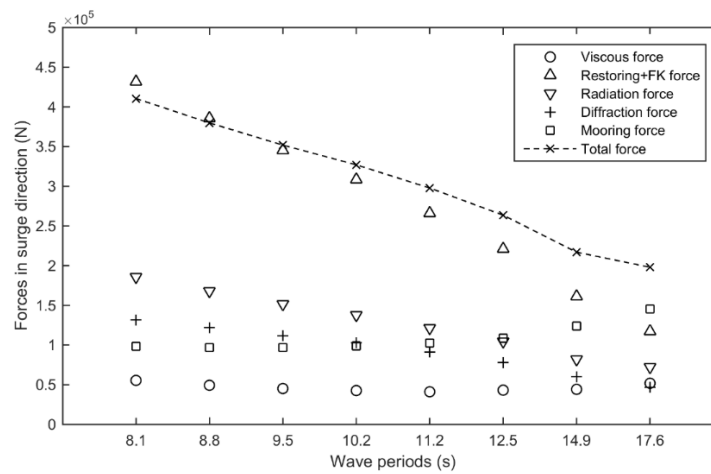
2.6.2 Quantitative analysis of the nonlinear wave force components and the viscous force

To study the quantitative contributions of the inviscid wave force components (hydrostatic, Froude-Krylov, radiation and diffraction forces), the viscous force and the mooring force to the total force that acts on the FPA, numerical results of the nonlinear potential flow solver are analyzed. Note that these are generalized “forces” including translational forces in the heave and surge directions and moments in the pitch direction. The viscous forces in

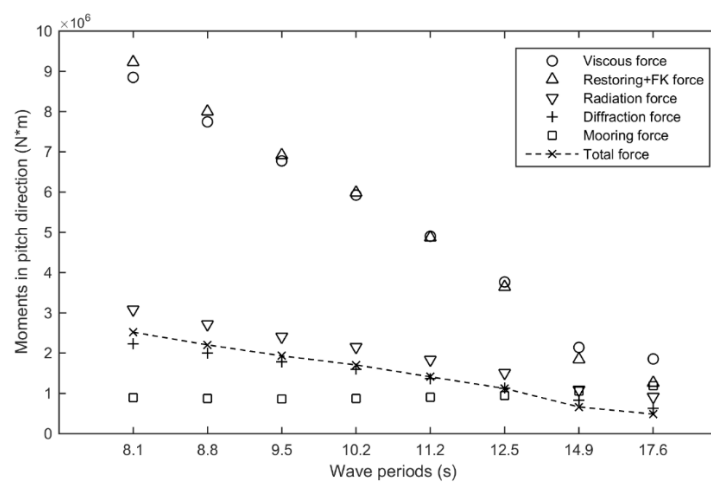
heave and surge directions are calculated using the Morison equation; the viscous force in the pitch direction is defined as the eddy-making damping moment in the pitch direction. Figure 2-10 compares the magnitudes (root mean squares) of the radiation force, the diffraction force, the sum of the restoring force and the Froude-Krylov force, the viscous force, the mooring force and the total force for wave periods from 8.1 s to 17.6 s in the heave, surge and pitch directions. Note that the restoring force is the sum of the hydrostatic force and the gravity force. (The reason of adding the restoring force and the Froude-Krylov force together when compared with other forces is discussed in detail in Appendix B .)



(a) In heave direction



(b) In surge direction



(c) In pitch direction

Figure 2-10. Comparisons of the individual inviscid wave force components, the viscous force and the total force

The dominant wave force components in the heave, surge and pitch directions are the restoring force and the Froude-Krylov force, the summation of which is indicated by the upward-pointing triangle of each wave period in Figure 2-10. The viscous force (indicated by the circle) is important in the heave and pitch directions. The magnitude of the radiation force (indicated by the plus sign) generally decreases as the wave period increases (or the corresponding wave length increases).

To further study the nonlinearity of the restoring force and the Froude-Krylov force, the nonlinear restoring force and the nonlinear Froude-Krylov force calculated in the time domain simulation are compared to the linear restoring force and the linear Froude-Krylov force calculated in the frequency domain simulation.

Table 2-3 presents the ratios R_r of the amplitudes of the nonlinear restoring force to the amplitudes of the linear restoring force for wave periods from $T = 8.1$ s to 17.6 s. The ranges of R_r are 5.4% - 100.4% and 20.4% - 124.9% in the heave and pitch directions, respectively. The ratio R_r reaches its minimum value at the wave period closest to the natural period in the individual heave and pitch directions: in the heave direction, $R_r = 5.4\%$ at $T = 8.1$ s (natural period $T = 8.4$ s); in the pitch direction, $R_r = 20.4\%$ at $T = 12.5$ s (natural period $T = 13.6$ s). R_r in the surge direction are not listed because the linear restoring forces in the surge direction are zero for all the wave periods.

Table 2-3. Ratios of the amplitudes of the nonlinear restoring force to the amplitudes of the linear restoring force in the heave and pitch directions

	$R_r = A_{\text{nonlinear_restoring_force}}/A_{\text{linear_restoring_force}}$	
Wave period (s)	Heave direction	Pitch direction
17.6	100.4%	124.9%
14.9	83.4%	45.1%
12.5	36.7%	20.4%
11.2	25.6%	46.8%
10.2	17.8%	67.6%
9.5	12.3%	82.1%
8.8	6.0%	100.3%
8.1	5.4%	122.2%

Table 2-4 presents the ratios R_f of the amplitudes of the nonlinear Froude-Krylov force to the amplitudes of the linear Froude-Krylov force for wave periods from $T = 8.1$ s to 17.6 s. The ranges of R_f are 117.6 - 142.6%, 23.7 - 96.9% and 114.0 - 290.8% in the surge, heave and pitch directions, respectively. In the heave direction, the ratio R_r reaches its minimum value of 23.7% at the wave period $T = 8.8$ s, which is close to the natural period $T = 8.4$ s. In the pitch direction, the ratios R_r are significantly larger than unity at wave periods of $T = 12.5$ s, 14.9s and 17.6s.

Table 2-4. Ratios of the amplitudes of the nonlinear Froude-Krylov force to the amplitudes of the linear Froude-Krylov force in the surge, heave and pitch directions

	$R_f = A_{\text{nonlinear_FK_force}}/A_{\text{linear_FK_force}}$		
Wave period (s)	Surge direction	Heave direction	Pitch direction
17.6	135.6%	96.9%	290.8%
14.9	142.6%	87.3%	265.9%
12.5	128.6%	38.7%	172.1%
11.2	124.6%	29.2%	145.6%
10.2	121.3%	25.1%	131.6%
9.5	120.5%	23.8%	125.3%
8.8	118.9%	23.7%	119.3%
8.1	117.6%	23.9%	114.0%

To study the overall effect of the nonlinear restoring force, the nonlinear Froude-Krylov force and the viscous force in the time domain simulation, the nonlinear motion responses in the time domain simulations are compared to the linear motion responses in the frequency domain simulations for wave periods from $T = 8.1$ s to 17.6 s (see Table 2-5). Results of the comparisons in the table shows that taking into account the nonlinear restoring force, the nonlinear Froude-Krylov force and the viscous force changes the predicted responses of the FPA significantly in the heave, surge and pitch directions. The largest differences, between the nonlinear and linear responses occur at $T = 12.5$ s, $T = 8.1$ s and $T = 12.5$ s in the surge, heave and pitch directions, respectively.

Table 2-5. Comparison of linear and nonlinear motion responses in the surge, heave and pitch directions

	$A_{\text{motion}}/A_{\text{wave_height}}$					
	Surge direction		Heave direction		Pitch direction	
Period (s)	linear	nonlinear	linear	nonlinear	linear	nonlinear
17.6	0.99	1.43	1.08	1.07	2.22	0.82
14.9	1.20	1.10	1.15	1.08	6.86	0.71
12.5	0.15	0.92	1.34	0.69	13.86	0.79
11.2	0.28	0.84	1.60	0.52	6.03	0.81
10.2	0.34	0.76	2.10	0.42	4.33	0.82
9.5	0.35	0.71	2.93	0.37	3.70	0.83
8.8	0.34	0.66	5.92	0.32	3.24	0.82
8.1	0.32	0.60	6.65	0.28	2.89	0.81

2.7 Concluding Remarks

In this study, the performances (accuracies and limitations) of an explicit finite element NS solver (ALE), an implicit finite element NS solver (ICFD) and a nonlinear potential flow solver (AQWA) in predicting the highly nonlinear hydrodynamic responses of a FPA under

large-amplitude waves are examined. The predicted response amplitudes of the FPA using these three solvers are found to compare well with the experimental data for wave periods from 8.8 s to 14.9 s. The accuracies of the three numerical solvers in the heave, surge and pitch directions can be summarized as follows:

- In the heave direction, the averaged relative differences between the numerical predictions and the experimental data for the ALE and ICFD NS solvers, which are 8.3% and 10.8% respectively, are close to the averaged relative difference for the nonlinear potential flow solver of 8.5%. Note that the viscous forces are computed automatically in these two NS solvers while the viscous force is computed empirically using the Morison equation in the potential flow solver.
- In the surge direction, the averaged relative differences between the numerical predictions and the experimental data for the ALE and ICFD NS solvers are 16.1% and 24.0%, respectively. These values are smaller than the averaged relative difference for the nonlinear potential flow solver, which is 67.4%. The better accuracies of these two NS solvers are mainly due to their ability to calculate the fully nonlinear wave force, while only the individual wave force components are calculated in the nonlinear potential flow solver.
- In the pitch direction, the averaged relative difference between the numerical predictions and the experimental data for the ALE NS solver is 42.2%, which is close to the averaged relative difference for the nonlinear potential flow solver of 35.7%. For the ALE NS solver, an eddy-making damping term is added in the governing equations of the FPA motions to compensate the vortices induced damping that are underestimated in solving the NS equations. For the nonlinear

potential flow solver, a corresponding eddy-making damping term is also added in the governing equations of the FPA motions to calculate the whole vortex-induced damping in the pitch direction that cannot be obtained by solving the potential flow equations.

The computational cost for the implicit ICFD NS solver is approximated 1.6 times as large as the computational cost for the explicit ALE NS solver, which is a result of the larger number of elements and re-meshing process in the ICFD NS solver. The computational cost for the potential flow solver is much smaller than the computational costs for the two NS solvers.

Through the quantitative analysis of the inviscid wave force components (the hydrostatic force, the Froude-Krylov force, the radiation force and the diffraction force), the viscous force, the mooring force and the total force in the time domain calculated by the nonlinear potential flow solver, it is found that for any wave period from 8.1 s to 17.6 s, the restoring force and the Froude-Krylov force are important for the highly nonlinear responses of the FPA in all the heave, surge and pitch directions. The viscous force is found to be important in the heave and pitch directions.

Through comparing the nonlinear restoring and Froude-Krylov forces in the time domain to the linear restoring and Froude-Krylov forces in the frequency domain respectively, the nonlinearities of the restoring and Froude-Krylov forces are shown to be important for the motion responses of the FPA in the heave and pitch directions, especially when the incident wave periods are close to the natural frequencies of the FPA response in the heave and pitch directions.

Based on the performances of the three numerical solvers in this study, the followings are suggested: a). the nonlinear potential flow solver can be used for preliminary studies of the highly nonlinear hydrodynamic responses of floating WECs under large-amplitude waves, with careful modeling of the viscous force; b). the two NS solvers, because of their high computational costs, should be employed to study the highly nonlinear hydrodynamic responses for extreme scenarios, keeping in mind the high computational effort required. For further study, the hydro-elastic responses of a floating WEC under large-amplitude waves can be analyzed using the two NS solvers.

2.8 Acknowledgements

Financial support from the Department of Energy Grant No. DE-FG36-08GO18179-M001 is gratefully acknowledged.

2.9 References

- Agamloh, E. B., Wallace, A. K., & von Jouanne, A. (2008). Application of Fluid-Structure Interaction Simulation of an Ocean Wave Energy Extraction Device. *Renewable Energy*, 33(4), 748-757. doi:10.1016/j.renene.2007.04.010
- Babarit, A., Mouslim, H., Clement, A., & Laporte-Weywada, P. (2009). *On the Numerical Modelling of the Nonlinear Behaviour of a Wave Energy Converter*. Paper presented at the ASME 28th 2011 International Conference on Ocean, Offshore and Arctic Engineering.
- Badia, S., Quaini, A., & Quarteroni, A. (2008). Modular vs. Non-Modular Preconditioners for Fluid-Structure Systems with Large Added-Mass Effect. *Computer Methods in Applied Mechanics and Engineering*, 197(49-50), 4216-4232. doi:10.1016/j.cma.2008.04.018
- Bearman, P. W., Graham, J. M. R., Obasaju, E. D., & Drossopoulos, G. M. (1984). The Influence of Corner Radius on the Forces Experienced by Cylindrical Bluff Bodies in Oscillatory Flow. *Applied Ocean Research*, 6(2), 83-89.
- Bhinder, M. A., Clive G. Mingham, Derek M. Causon, Mohammad T. Rahmati, George A. Aggidis, and Robert V. Chaplin. (2009). *A Joint Numerical and Experimental Study of a Surging Point Absorbing Wave Energy Converter (WRASPA)*. Paper

- presented at the ASME 2009 28th International Conference on Ocean, Offshore and Arctic Engineering.
- Bretl, J. G. (2009). *A Time Domain Model for Wave Induced Motions Coupled to Energy Extraction*. (PhD), The University of Michigan.
- Causin, P., Gerbeau, J. F., & Nobile, F. (2005). Added-Mass Effect in the Design of Partitioned Algorithms for Fluid-Structure Problems. *Computer Methods in Applied Mechanics and Engineering*, 194(42-44), 4506-4527. doi:10.1016/j.cma.2004.12.005
- Chakrabarti, S. (2001). Empirical Calculation of Roll Damping for Ships and Barges, *Ocean Engineering*, 28, 915-932.
- Faltinsen, O. (1990). *Sea Loads on Ships and Offshore Structures*: Cambridge university press.
- Fenton, J. D. (1985). A Fifth-Order Stokes Theory for Steady Waves. *Journal of waterway, port, coastal, and ocean engineering*, 111(2), 216-234.
- Finnegan, W., & Goggins, J. (2012). Numerical Simulation of Linear Water Waves and Wave-Structure Interaction. *Ocean Engineering*, 43, 23-31. doi:10.1016/j.oceaneng.2012.01.002
- Gilloteaux, J. C., Bacelli, G., & Ringwood, J. (2008). *A Non-Linear Potential Model to Predict Large-Amplitudes-Motions: Application to a Multi-Body Wave Energy Converter*. Paper presented at the World Renewable Energy Congress.
- Graham, J. M. R. (1980). The Forces on Sharp-Edged Cylinders in Oscillatory Flow at Low Keulegan–Carpenter Numbers. *Journal of Fluid Mechanics*, 97(2), 331-346.
- Guérinel, M., Alves, M., & Sarmiento, A. (2011). *Nonlinear Modelling of the Dynamics of a Free Floating Body*. Paper presented at the European Wave and Tidal Energy Conference.
- Himeno, Y. (1981). *Prediction of Ship Roll Damping — State of the Art (No. 239)*.
- Idelsohn, S. R., Del Pin, F., Rossi, R., & Onate, E. (2009). Fluid-Structure Interaction Problems with Strong Added-Mass Effect. *International Journal for Numerical Methods in Engineering*, 80(10), 1261-1294. doi:10.1002/nme.2659
- Ikeda, Y., Fujiwara, T., & Katayama, T. (1993). *Roll Damping of a Sharp-Cornered Barge and Roll Control by a New-Type Stabilizer*. Paper presented at the In Proceedings of the 3rd International Offshore and Polar Engineering Conference.
- Li, Y., Yu, Y.-H., Previsic, M., Epler, J., Nelson, E., & Lawson, M. (2016). Laboratory Experimental Investigation of Power Generation Capability and Survivability of Two-Body Floating Point Absorbers. *Journal of Oceanic Engineering*.
- Merigaud, A., Gilloteaux, J.-C., & Ringwood, J. V. (2012). *A Nonlinear Extension for Linear Boundary Element Methods in Wave Energy Device Modelling*. Paper presented at the ASME 2012 31st International Conference on Ocean, Offshore and Arctic Engineering.
- Monroy, C., Ducrozet, G., Bonnefoy, F., Babarit, A., Gentaz, L., & Ferrant, P. (2010). *RANS Simulations of a CALM Buoy in Regular and Irregular Seas using the SWENSE Method*. Paper presented at the Proceedings of the Twentieth (2010) International Offshore and Polar Engineering Conference.

- Omidvar, P., Stansby, P. K., & Rogers, B. D. (2013). SPH for 3D Floating Bodies using Variable Mass Particle Distribution. *International Journal for Numerical Methods in Fluids*, 72(4), 427-452. doi:10.1002/fld.3749
- Park, J. C., Kim, M. H., & Miyata, H. (1999). Fully Non-Linear Free-Surface Simulations by a 3D Viscous Numerical Wave Tank. *International Journal for Numerical Methods in Fluids*, 29(6), 685-703. doi:10.1002/(sici)1097-0363(19990330)29:6<685::aid-fld807>3.0.co;2-d
- Rogne, Ø. Y. (2014). *Numerical and Experimental Investigation of a Hinged 5-Body Wave Energy Converter*. (PhD), Norwegian University of Science and Technology.
- Sarpkaya, T. (1976). *Vortex Shedding and Resistance in Harmonic Flow about Smooth and Rough Circular Cylinders at High Reynolds Numbers*. Paper presented at the In Proceedings of the International Conference on Behavior of Offshore Structures BOSS'76.
- Sclavounos, P. D. (2012). Nonlinear Impulse of Ocean Waves On Floating Bodies. *Journal of Fluid Mechanics*, 697, 316-335. doi:10.1017/jfm.2012.68
- Souli, M., & Benson, D. J. (2010). *Arbitrary Lagrangian Eulerian and Fluid-Structure Interaction: Numerical Simulation*: John Wiley & Sons.
- Westphalen, J., Greaves, D. M., Hunt-Raby, A., Williams, C. J. K., Taylor, P. H., Hu, Z. Z., . . . Omidvar, P. (2010). *Numerical Simulation of Wave Energy Converters Using Eulerian And Lagrangian CFD Methods*.
- Yu, Y.-H., & Li, Y. (2013). Reynolds-Averaged Navier-Stokes Simulation of the Heave Performance of a Two-Body Floating-Point Absorber Wave Energy System. *Computers & Fluids*, 73, 104-114. doi:10.1016/j.compfluid.2012.10.007
- Zurkinden, A. S., Ferri, F., Beatty, S., Kofoed, J. P., & Kramer, M. M. (2014). Non-Linear Numerical Modeling and Experimental Testing of a Point Absorber Wave Energy Converter. *Ocean Engineering*, 78, 11-21. doi:10.1016/j.oceaneng.2013.12.009

CHAPTER 3

3. Evaluation of a Catenary Spread Mooring System Design of a Wave Energy Converter Test Platform through both Field Test Study and Quasi-Static Analysis

Junhui Lou ^a, Solomon Yim ^{a*}, Joshua Baker ^b, Ean Amon ^c and Annette von Jouanne ^a
^a Oregon State University, ^b US Navy, ^c Columbia Power Technologies

3.1 Abstract

This study firstly presents a catenary spread mooring system design of a mobile ocean test berth (MOTB), the Ocean Sentinel (OS) instrumentation buoy, which is developed by the Northwest National Marine Renewable Energy Center (NNMREC) to facilitate ocean test of wave energy converters (WECs). Then the OS mooring design, which is similar to a conventional WEC point absorber mooring system, is evaluated through both field test analysis and quasi-static analysis: the field test analysis is based on the extensive data of the OS positions, mooring tensions on the OS and environmental conditions of waves, wind and current, collected during the 2013 field test of the OS mooring system; the quasi-static analysis is based on the analytical catenary equations of mooring chains. Both global characteristics and survivability characteristics of the mooring system are evaluated: the global characteristics include the influence of the OS excursion to mooring tension, positional distribution of the OS, directional control of the OS and environmental contributions of waves, current and wind to mooring tensions; the survivability characteristics include the anchor movability and strength capacities of mooring lines. Because anchor movement occurred near the end of the field test, a systematic procedure

of designing a mooring system with adequate anchor resistance is developed and applied to design a new OS mooring system.

Keywords: Mobile ocean test berth, wave energy converter, mooring design, field test, static analysis, global characteristics, survivability characteristics, design procedure

3.2 Introduction

Wave energy converters (WECs) harness energy from ocean waves utilizing many different designs including: point absorber, attenuator, wave surge converter, oscillating water column, submerged point absorber, and overtopping devices among others. Compared to the moorings of conventional floating structures such as vessels, and oil and gas platforms, the moorings of floating WECs have their own characteristics (Johanning et al., 2007): 1), floating WEC devices have relatively small dimensions compared to typical ocean wind generated wave lengths (60 m to 150 m); 2), WEC devices are usually deployed in shallow and intermediate water depths (less than 150 m (API, 2007)) (Weller et al., 2014); 3), the mooring system stiffness may affect energy extraction efficiency of the WEC devices (Johanning et al., 2007).

The guidelines for mooring designs of floating WECs are still under development because of the relatively new wave energy industry, while the guidelines for conventional floating structures are comprehensive and well developed (API, 1997; CMPT, 1998; DNV, 2013). Contents of current WEC mooring design guidelines include mainly the assessment of available mooring technologies (Harris et al., 2004; SST, 2009; Weller et al., 2014), general procedure of mooring design (Rodríguez et al., 2011; Zanuttigh, Martinelli, et al., 2013)

and applications of mooring design to specific WECs (Martinelli et al., 2012; Ruiz-Minguela et al., 2008).

To gain a better understanding of the characteristics of WEC mooring systems, experimental studies have been conducted, among which many have focused on wave tank tests while a few have focused in field tests. In the experimental studies based on wave tank tests, the following WEC mooring characteristics were examined: the dynamic tensions of mooring lines (Ambühl et al., 2014; Hald and Frigaard, 2001; Harnois et al., 2015; Martinelli et al., 2010; Palm et al., 2013; Parmeggiani et al., 2013; Wolf, 2012), the damping effect of a single catenary line (Johanning et al., 2007) and the influences of mooring systems on the motion responses of WECs (Ruiz-Minguela et al., 2008; Zanuttigh, Angelelli, et al., 2013).

Compared to the number of wave tank tests, there are fewer field tests because of their higher costs and operational difficulties. Additionally, only a few WEC devices have been mature enough to reach the stage of ocean test. However, the field test has its unique advantage of testing a prototype WEC in real ocean conditions with waves, wind and current. In the experimental studies based on field tests, their works are described as follows: the relationship between mooring tensions and significant wave heights was discussed based on a field test of the CALM (Catenary Anchor Leg Mooring) system of the Wave Dragon overtopping device (Kofoed et al., 2006); the mooring line fatigue damage, anchor movement and relationship between wave conditions and extreme mooring tensions were studied based on a field test of a three-leg catenary mooring of an instrumentation buoy at the South West Mooring Test Facility (SWMTF) (Thies et al.,

2014; Harnois et al., 2012; Harnois et al., 2013); and the field test of a multi-catenary spread mooring of the OCEANTEC WEC was described in Salcedo et al. (2009).

In the above field test studies the followings were not discussed: (1) influence of WEC excursion on mooring tension; (2) importance of dynamic mooring tension compared to mean mooring tension; (3) influences of wind and current conditions on mooring tensions; and (4) a procedure of mooring design to prevent anchor movement.

This study presents the field test of a multi-body catenary spread mooring system of a mobile ocean test berth (MOTB), the Ocean Sentinel, which is developed by the Northwest National Marine Renewable Energy Center (NNMREC) to facilitate ocean test of WECs (Amon et al., 2011; von Jouanne et al., 2013). Through the extensive field measurements of mooring tensions, OS positions and environmental conditions (waves, current and wind), as well as the results of quasi-static analysis, the global characteristics and survivability characteristics of the OS mooring system, which is similar to a conventional WEC point absorber mooring system, are evaluated: (1) The global characteristics include the influence of OS excursion to mooring tension, positional distribution of the OS, directional control of the OS and environmental contributions (waves, current and wind) to mooring tensions; and (2) The survivability characteristics include anchor movability and strength capacities of mooring lines under extreme environmental conditions. As the OS drifted significantly away from its position domain near the end of the OS field test, the anchor resistance was not adequate in the original mooring design. A systematic procedure of designing a new mooring system with adequate anchor resistance is developed and applied to design a new mooring configuration with the smallest maximum of effective force.

3.3 Background of the Mobile Ocean Test Berth Project

The NNMREC, a US Department of Energy (USDOE) Center headquartered at Oregon State University (OSU), seeks to facilitate the integration of marine renewables onto the utility grid. To facilitate ocean test of WECs that are ready for field trials, but are not sufficiently mature to be connected to the electrical grid, NNMREC pursued the development of a MOTB. The proposed MOTB would be moored in proximity to the WEC under test, connected by the WEC power cable, and provide power analysis and data acquisition, environmental monitoring, as well as power dissipation to an on-board electrical load.

Initially NNMREC pursued the design of a full/utility power scale (500 kW – 1 MW) MOTB, and went through an open request for proposal (RFP) process to select an industry team with subcontractors. Through the preliminary design process, two significant design challenges emerged rendering the full/utility scale system unfeasible at that time, namely grid mimic capabilities as well as the submarine power cable and the interconnection to the MOTB and the wave energy converter (WEC) under test.

NNMREC then assembled a group of outside experts to review alternatives and provide expert feedback to consider in planning the path forward. Through these discussions NNMREC was recommended to pursue a phased test facility process toward a cable-to-shore based test berth that can test multiple devices:

PHASE 1: Permitted Open-Ocean Test Site

- Phase 1a: Develop Permitted Open-Ocean Test Site
- Phase 1b: Develop Test Protocols for Open Ocean Test
- Phase 1c: Build 30 – 100 kW Test Platforms for Scaled Test

PHASE 2: Utility Scale, Grid-connected Wave Energy Test Site

- Up to four 4 separate cables, 5-8 miles from shore for testing individual WECs or arrays
- Grid Emulator for non grid-connect testing

For the Phase 1 MOTB 100 kW test platform, NNMREC chose the structural hull to be the 6-meter NOMAD (Navy Oceanographic Meteorological Automatic Device). The 6m NOMAD supplier on the west coast is AXYS Technologies, and NNMREC worked with AXYS on the development of what became the “Ocean Sentinel” instrumentation buoy for testing WEC devices. The original NOMAD has a single point mooring system designed to enable pivoting based on sea and wind conditions. However, for testing a WEC with a power cable connecting the WEC to the NOMAD test platform, an alternative mooring design needed to be developed to prevent twisting of the power cable in various sea conditions. Through design contracting with an ocean engineering firm, a three-point spread mooring system (three mooring legs) was developed for the Ocean Sentinel NOMAD test platform. The Ocean Sentinel was deployed offshore of Newport, OR, at the NNMREC North Energy Test Site (NETS) for the test of a WEC in the summer of 2012 (Lettenmaier et al., 2013), and deployed again in the summer of 2013 to analyze the mooring system and to provide insights for similar WEC mooring system designs (Baker, 2013).

3.4 The 2013 Field Test of OS Mooring System

3.4.1 Properties of the OS hull

The OS hull design originated from the NOMAD design in the late 1940s for U.S. Navy's (USN) offshore data collection program. Since 1974, a total of 15 NOMAD buoys of the USN were gradually transferred to the U.S. National Data Buoy Center (NDBC) to collect meteorological and wave data. Because of its performance regarding response, survivability and cost efficiency, the NOMAD hull design was chosen by NNMREC for the OS and fabricated by AXYS Technologies.

The geometry of the OS is shown in Figure 3-1. The dimensions and mass properties of the OS are listed in Table 3-1.



(a) Side view



(b) Front view



(c) Rear view

Figure 3-1. Geometry of Ocean Sentinel (photos by Dan Hellin)

Table 3-1. Dimensions and mass properties of the Ocean Sentinel

Ocean Sentinel	
Length	6.15 m (20.17 ft)
Width	3.20 m (10.50 ft)
Height	2.13 m (7.00 ft)
Draft	1.51 m (4.95 ft)
Center of gravity	0.81 m (2.66 ft) below MWL
Mass	8460 kg (18650 lb)

3.4.2 The OS mooring system design

Because the OS serves as a test platform for WECs and the OS dimensions are relatively small compared to ships and platforms in the oil industry, there are some specific requirements in designing the OS mooring system. Firstly, the mooring system provides directional control on the OS, so that the OS does not rotate 360 degrees and cause entanglement of mooring lines and an umbilical cable. Secondly, the moored OS moves inside a region which is limited in dimensions. The main purpose for this requirement is to reduce the distance variation between the OS and a WEC under ocean test. As the OS and a WEC are connected through an umbilical power cable, large distance variations can cause either an overly tensioned condition or a large deflection condition for the umbilical cable. Thirdly, the vertical downward mooring forces on the OS are small enough to prevent both submerging and flipping over of the OS. Note that some of these design requirements are also applicable to mooring systems of WECs. The directional control requirement is necessary for a WEC that is designed to face the primary direction of waves (e.g., the SeaRay WEC (Brekken et al., 2013)). The small space region requirement means that more WECs can be positioned inside a wave energy farm (e.g. (Ricci et al., 2012)).

Considering the design requirements above, a multi-body catenary mooring system with three mooring legs was designed for the OS in its 2013 field test. Plan view of the 2013 mooring system is plotted in Figure 3-2, with mooring components shown in detail. The mooring system has three mooring legs (bow, port and starboard (STBD) mooring legs) and an OS heading direction facing the summer average dominant wave direction. Side view of the mooring system is shown in Figure 3-3, with dimensional details of the mooring components: (1) The main catenary lines for the bow mooring leg are a 10 m top chain, a

70 m polyester line and an 82 m bottom chain; (2) The main catenary lines for the port (starboard) mooring leg are an 86 m polyester line and a 55 m bottom chain; and (3) The surface buoys are spheres with a diameter of 1.47 m.

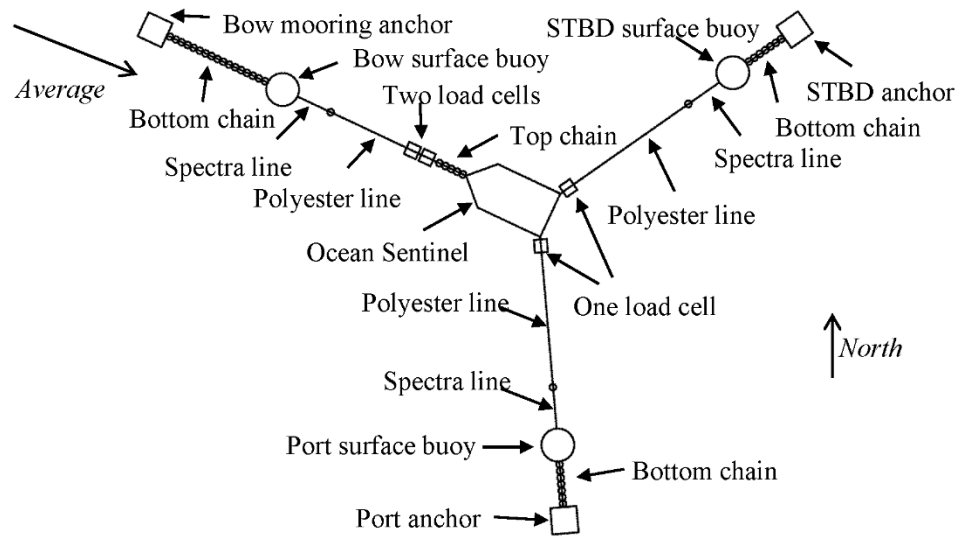


Figure 3-2. Plan view of the 2013 Ocean Sentinel mooring system

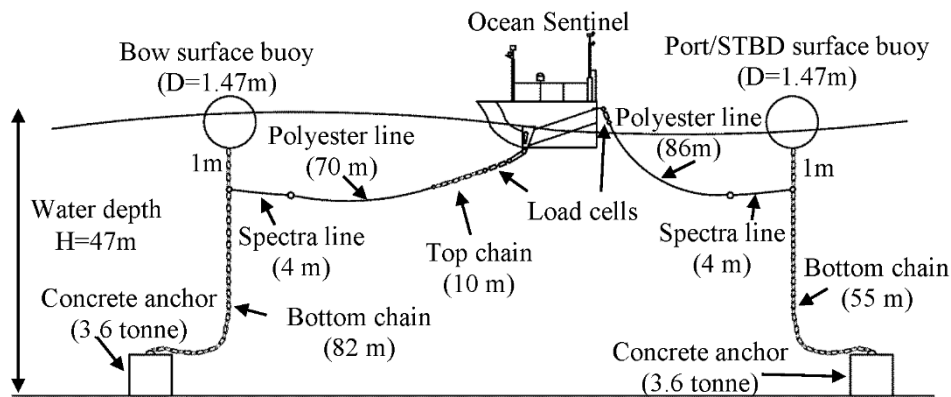


Figure 3-3. Side view of the 2013 Ocean Sentinel mooring system

The design details of the mooring system, which corresponds to the design requirements mentioned earlier, are listed as follows. Firstly, for the requirement of directional control on the OS, a spread mooring system with the bow, port and starboard mooring legs was selected. Secondly, for the requirement of small dimensions of OS position domain, the level of compliance for each mooring leg was small. This was accomplished by having small L/H ratios for the bottom chains (which ratio typically ranges from 3 to 8 (Fitzgerald and Bergdahl, 2007), where L is the chain length and H is the water depth. The L/H ratios for the bow and port (starboard) bottom chains were 1.8 and 1.2, respectively. Thirdly, for the requirement of small downward force on the OS, a surface buoy was attached to the top of every bottom chain, so that the polyester lines which connected the OS and the tops of bottom chains were almost horizontal.

3.4.3 Field test measurements and a notable event

The OS and its mooring system were deployed at the NETS in 2013 from 07/29 to 10/03 with load cells added to enable an additional task of measuring the mooring line tensions on the OS.

During the 2013 field test of the OS, the following field data were recorded:

- Wind data measured continuously and recorded every 10 minutes in the form of wind speed and direction
- GPS positions of the OS recorded every 10 minutes in the form of latitude and longitude

- Wave data measured continuously by the TRIAXYS buoy (deployed approximately 140m away from the OS) and recorded every 20 minutes in the form of wave height, wave period, wave direction and wave spectrum
- Current data measured continuously by the TRIAXYS buoy and recorded every 20 minutes in the form of current speed and direction along with water depth
- Mooring tension data measured by the load cells attached to the bow, port and starboard polyester lines and recorded at a frequency of 20 Hz.

On 09/22/13, the OS drifted significantly toward the north, which was likely caused by anchor movement. As shown in Figure 3-4, the OS positions before 09/22 indicated by the yellow points were inside a position domain marked by the red dashed lines; while the OS positions on 09/22 indicated by the blue points moved out of the position domain. For the studies presented later, global characteristics of the mooring system are studied for the period before the significant OS drift because the anchor movement likely changed the initial mooring configuration, and anchor movability is studied for the period during the significant OS drift.

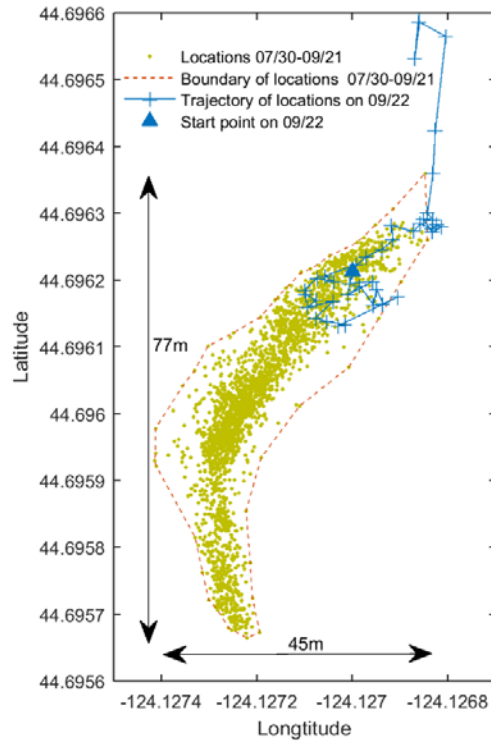


Figure 3-4. GPS positions of the Ocean Sentinel from 07/30 to 09/22

3.5 Quasi-Static Analysis of Catenary Mooring Chains

For the OS mooring system, each mooring leg has two major catenary lines, a polyester line and a bottom mooring chain. Because of the almost negligible submerged weights of polyester lines (0.08 kN for the bow polyester line, 0.10 kN for the port and starboard polyester lines) compared to the submerged weights of the mooring chains (9.08 kN for the bow chain, 6.11 kN for the port and starboard chains), the mooring tensions on the OS (restoring force) are mainly provided through the geometric compliance of the mooring chains.

The loaded forces and geometric parameters of a mooring chain are illustrated in Figure 3-5. In this figure, F_b is the total mooring tension at the bottom end of the mooring chain; F_{bh} and F_{bv} are the horizontal and vertical components of F_b , respectively; F_t is the total

mooring tension at the top end of the mooring chain; F_{th} and F_{tv} are the horizontal and vertical components of F_t , respectively; θ_b and θ_t are the vertical angles of F_b and F_t , respectively; L is the length of mooring chain; H is the water depth; D is the horizontal distance from the top of the mooring chain to the mooring anchor; and F_o is the total force on the OS.

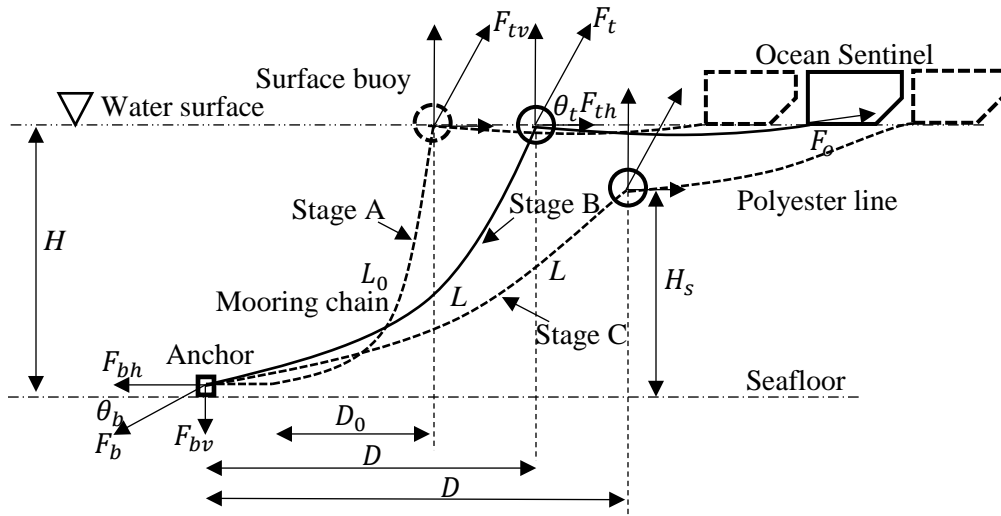


Figure 3-5. Geometric parameters and forces of the OS mooring system

As the horizontal force on the top of the mooring chain (F_{th}) increases, the mooring chain shape changes through three stages: (1) When F_{th} is relatively small, only part of the mooring chain is suspended with $\theta_b = 0$ (stage A); (2) When F_{th} is relatively moderate, the whole mooring chain is suspended ($\theta_b > 0$) and the surface buoy floats on the sea surface, at which scenario F_{tv} is smaller than the buoyancy of the surface buoy subtracted by its own weight (stage B); and (3) When F_{th} is relatively large, the whole mooring chain is suspended ($\theta_b > 0$) and the surface buoy is submerged under the sea surface, at which scenario F_{tv} equals to the buoyancy of the surface buoy subtracted by its own weight (stage C).

Because of the uniform weight distribution along the mooring chain, the suspended part of the mooring chain is governed by catenary equations in static analysis.

At stage A, the corresponding governing equations for the mooring chain are as follows:

$$\frac{F_{tv}}{w \cdot H} = \frac{\sin(\theta_t)}{1 - \cos(\theta_t)} \quad \text{Eq. (3.1)}$$

$$\frac{F_{th}}{w \cdot H} = \frac{\cos(\theta_t)}{1 - \cos(\theta_t)} \quad \text{Eq. (3.2)}$$

$$\frac{L_0}{H} = \cot(\theta_t/2) \quad \text{Eq. (3.3)}$$

$$\frac{D_0}{H} = \frac{\cos(\theta_t)}{1 - \cos(\theta_t)} \sqrt{-6 + \sqrt{36 + 12 \left\{ \tan(\theta_t)^2 - \left(\frac{1 - \cos(\theta_t)}{\cos(\theta_t)} \right)^2 \right\}}} \quad \text{Eq. (3.4)}$$

$$\theta_b = 0 \quad \text{Eq. (3.5)}$$

$$D = (L - L_0) + D_0 \quad \text{Eq. (3.6)}$$

where w is the submerged weight per unit length of mooring chain; L_0 is the suspended length of the mooring chain, D_0 is the horizontal distance between the two ends of the suspended part of the mooring chain.

At stage B, the corresponding governing equations for the mooring chain are as follows:

$$\frac{F_{tv}}{w \cdot H} = \frac{\sin(\theta_t) \cdot \cos(\theta_b)}{\cos(\theta_b) - \cos(\theta_t)} \quad \text{Eq. (3.7)}$$

$$\frac{F_{th}}{w \cdot H} = \frac{1}{\sec(\theta_t) - \sec(\theta_b)} \quad \text{Eq. (3.8)}$$

$$\frac{L}{H} = \frac{\tan(\theta_t) - \tan(\theta_b)}{\sec(\theta_t) - \sec(\theta_b)} \quad \text{Eq. (3.9)}$$

$$\frac{D}{H} = \frac{1}{\sec(\theta_t) - \sec(\theta_b)} \sqrt{-6 + \sqrt{36 + 12 \{ (\tan(\theta_t) - \tan(\theta_b))^2 - (\sec(\theta_t) - \sec(\theta_b))^2 \}}} \quad \text{Eq. (3.10)}$$

At stage C, the corresponding governing equations for the mooring chain are as follows:

$$\frac{F_{tv}}{w \cdot H_s} = \frac{\sin(\theta_t) \cdot \cos(\theta_b)}{\cos(\theta_b) - \cos(\theta_t)} \quad \text{Eq. (3.11)}$$

$$\frac{F_{th}}{w \cdot H_s} = \frac{1}{\sec(\theta_t) - \sec(\theta_b)} \quad \text{Eq. (3.12)}$$

$$\frac{L}{H_s} = \frac{\tan(\theta_t) - \tan(\theta_b)}{\sec(\theta_t) - \sec(\theta_b)} \quad \text{Eq. (3.13)}$$

$$\frac{D}{H_s} = \frac{1}{\sec(\theta_t) - \sec(\theta_b)} \sqrt{-6 + \sqrt{36 + 12\{(\tan(\theta_t) - \tan(\theta_b))^2 - (\sec(\theta_t) - \sec(\theta_b))^2\}}} \quad \text{Eq. (3.14)}$$

$$F_{tv} = 13.7 \text{ kN} \quad \text{Eq. (3.15)}$$

where H_s is the vertical elevation of the surface buoy relative to the seafloor; 13.7 kN is the buoyancy of the surface buoy subtracted by its own weight.

Based on the catenary equations (Eq. 3.1-3.15), the quasi-static relationship between the surface buoy excursion D and the horizontal force F_{th} can be calculated at stages A-C for the individual bow, port and starboard chains (see Figure 3-6), which presents the important stiffness characteristics of mooring chains. It is found that in each stage of the individual mooring chains, F_{th} gradually increases as D increases with an increasing slope. Additionally, the increasing slope of F_{th} in stages A, B or C for the port (starboard) chain ($L/H=1.2$) are different from the corresponding increasing slope for the bow chain ($L/H=1.8$).

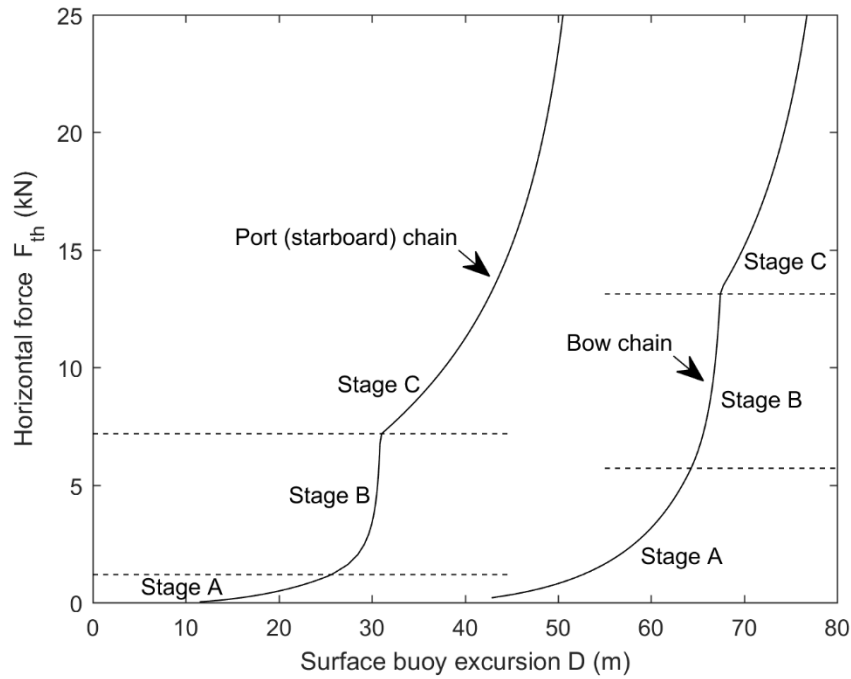


Figure 3-6. Quasi-static relationship between the top horizontal force F_{th} and surface buoy excursion D

3.6 Global Characteristics of the OS Mooring System

In this section, global characteristics of the OS mooring system under ocean environments including the influence of OS on mooring tension, position distribution of the OS, directional control of the OS and the waves, current and wind influences on mooring tensions, are studied.

3.6.1 Influence of OS excursion on mooring tension

3.6.1.1 Mean mooring tension vs. OS instantaneous position

During the field test of the OS, the mooring tension acting on the OS changes with the corresponding OS position. Figure 3-7 plots the space distribution of the mean mooring tension for every 20 minutes for the individual bow, port and starboard mooring lines. The

color of each point in the figure corresponds to the magnitude of mooring tension (unit in kN).

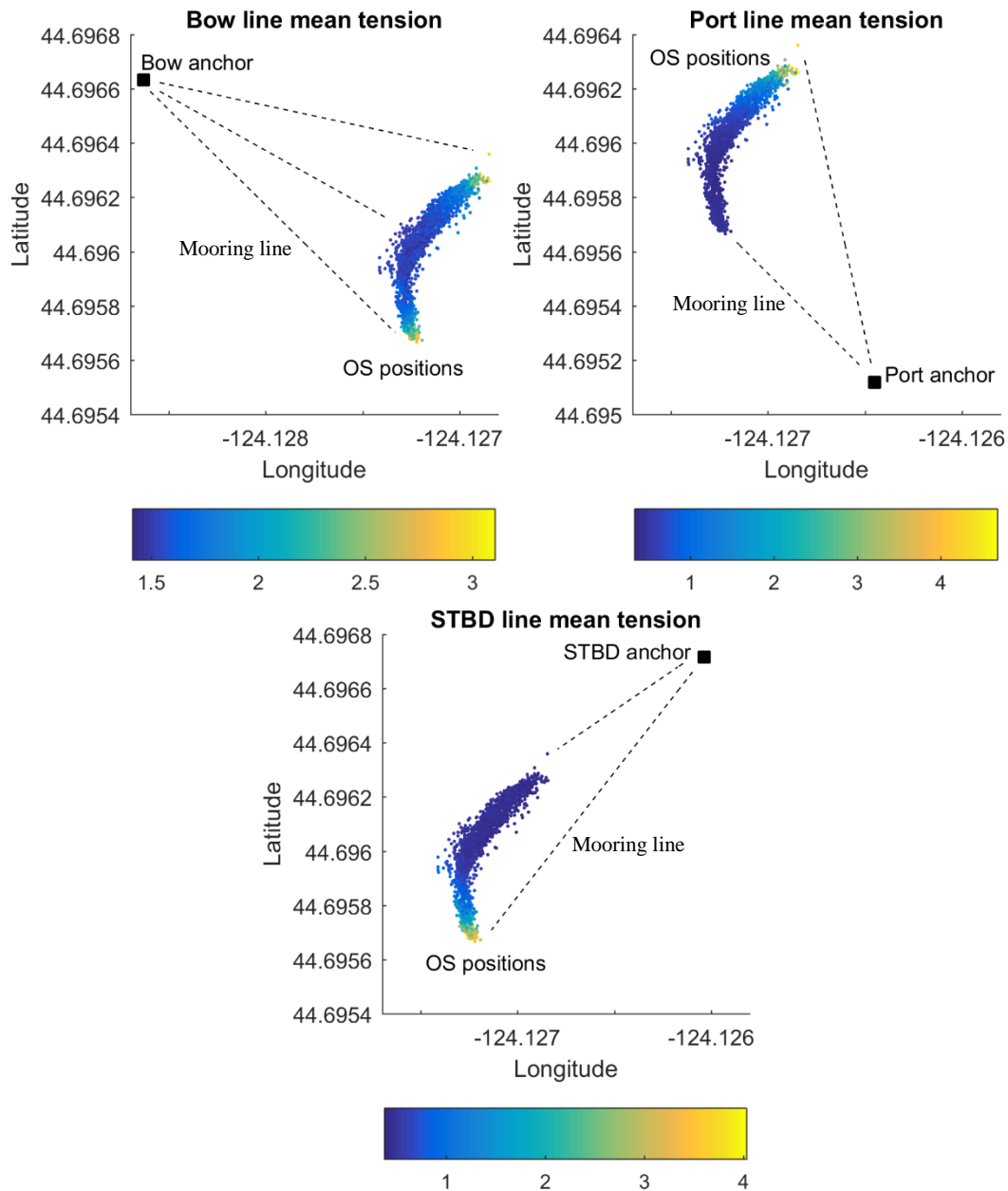


Figure 3-7. Mean mooring tensions of the bow, port and starboard lines with respect to Ocean Sentinel positions before the significant OS drift

The mean tensions of the bow, port and starboard mooring lines are shown to be closely related to the OS positions. For individual mooring lines, mean tensions of the bow line were relatively small when the OS was located at the center of its position domain, and increased when the OS moved toward either the northeast direction or the south direction; mean tensions of the port line were relatively small when the OS was located near the south edge of its position domain, and increased toward the northeast direction; and mean tensions of the starboard line were relatively small when the OS was located near northeast edge of its position domain, and increased toward the south direction. At different OS positions, the bow and port mooring tensions were at their largest at the northeast edge of the OS position domain while the starboard mooring tension was relatively small; the bow and starboard mooring tensions were at their largest at the south edge while the port mooring tension was relatively small; and all the bow, port and starboard mooring tensions were relatively small at the central region. Note that space distributions of the maximum and standard deviation of mooring tension are generally close to the space distribution of the mean mooring tension discussed earlier for individual mooring lines, except scale differences.

3.6.1.2 Trend of mean mooring tension vs. OS excursion

The above relationship between the mean mooring tension and OS position can also be demonstrated through the relationship between the mean mooring tension and excursion of the OS (horizontal distance from the OS to a mooring anchor), which is plotted in Figure 3-8 for individual bow, port and starboard moorings. It is shown that the mean mooring tension generally increases as the OS excursion increases, with an increasing slope.

Additionally, the slope increasing rate of the port (starboard) mooring leg ($L/H=1.2$) at large OS excursion is faster than that of the bow mooring leg ($L/H=1.8$) at large excursion, which indicates stronger stiffness hardening effect of the port (starboard) mooring leg.

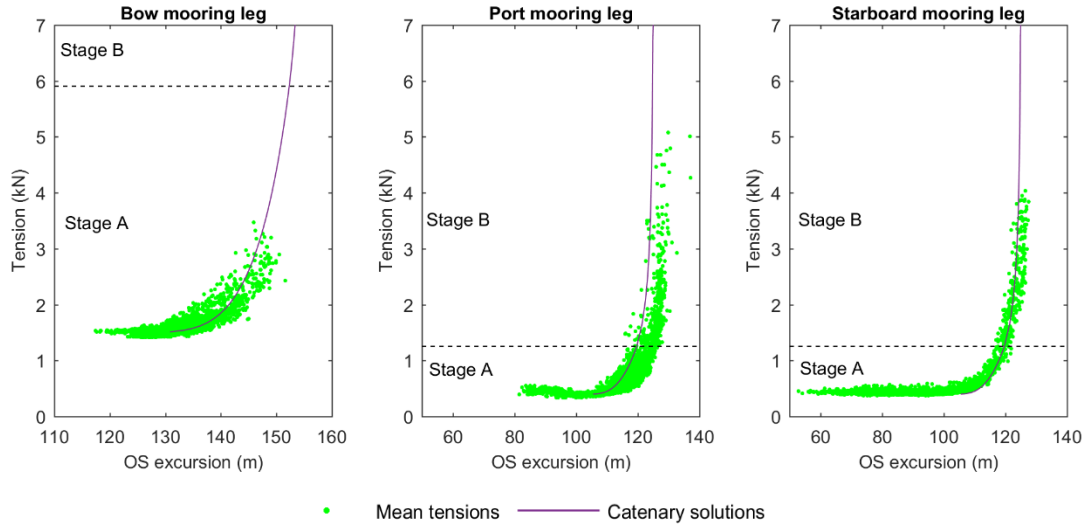


Figure 3-8. The relationship between the mean mooring tension and OS excursion compared to the quasi-static tension-excursion curve of the OS

In Figure 3-8, the measured relationship between the mean mooring tension and OS excursion is also compared to the quasi-static relationship between the mooring tension on the OS (F_o) and OS excursion (D_t), which is calculated using the catenary equations of Eq. 3.1-3.15 and the following Eq. 3.16-17:

$$F_o = \sqrt{F_{th}^2 + F_{ov}^2} \quad \text{Eq. (3.16)}$$

$$D_t = D + L_p \quad \text{Eq. (3.17)}$$

where F_{ov} is the vertical mooring force on the OS, which is related to the submerged weight of the mooring line connecting the surface buoy and the OS; L_p is the length of the mooring line.

The mean tension-OS excursion relationship is close to the quasi-static excursion-tension curve of the OS. Under the mean mooring tensions of the bow mooring line, the bow mooring chain is at stage A; under the mean mooring tensions of the port (starboard) mooring line, the port (starboard) mooring chain is at either stage A or B. Additionally, at large mean mooring tensions of the individual bow, port and starboard mooring legs, the increasing slope of mooring tension with respect to OS excursion is significant, which could induce strong dynamic response of mooring tension when the OS excursion oscillates under large-amplitude waves.

3.6.1.3 Trend of dynamic mooring tension vs. OS excursion

To investigate the dynamic mooring tensions acting on the OS, the mean, maximum and standard deviation of measured mooring tension with respect to the OS excursion are compared in Figure 3-9 for the individual bow, port and starboard legs. The green, blue and orange points in the figure indicate means, maximums and standard deviations of mooring tensions for every 20 minutes, respectively.

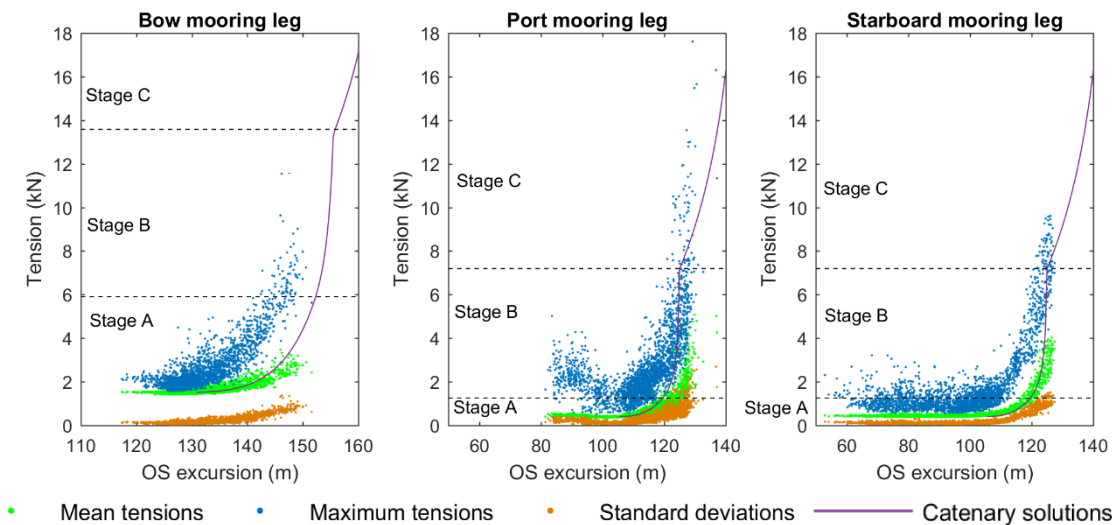


Figure 3-9. Means, maximums and standard deviations of mooring tensions with respect to OS excursions

The dynamic oscillations of measured bow, port and starboard mooring tensions are shown to be significant at large OS excursions: first, the differences between the maximums and means of mooring tensions are significant at large excursions; second, the ratios of standard deviation to mean tension can be as large as 0.4, 0.8 and 0.7 for the bow, port and starboard mooring legs, respectively.

Comparing the maximum mooring tensions with respect to OS excursions to the quasi-static mooring tension-OS excursion curve for the individual bow, port and starboard mooring legs (see Figure 3-9), the maximum mooring tensions are shown to differ from the quasi-static curve. In addition, under large maximum tensions of the port (starboard) mooring leg, the port (starboard) mooring chain is at stage C, in such scenario, the surface buoy may be submerged under the sea surface.

3.6.2 Position distribution of the OS

The numbers of OS occurrence at different positions are plotted in Figure 3-10, where the color of each point indicates the number of occurrence within a 1.5 m by 1.5 m area. Before the significant OS drift, the dimensions of the OS position domain are 77 m long and 45 m wide, which are 12.5 times and 7.3 times of the OS length (6.2 m), respectively. This shows that the OS mooring system can limit OS movements inside a relatively small region. Additionally, the number of OS occurrence was relatively large at the center of the position domain; and the number of OS occurrence was relatively small at the northeast and south edges of the position domain.

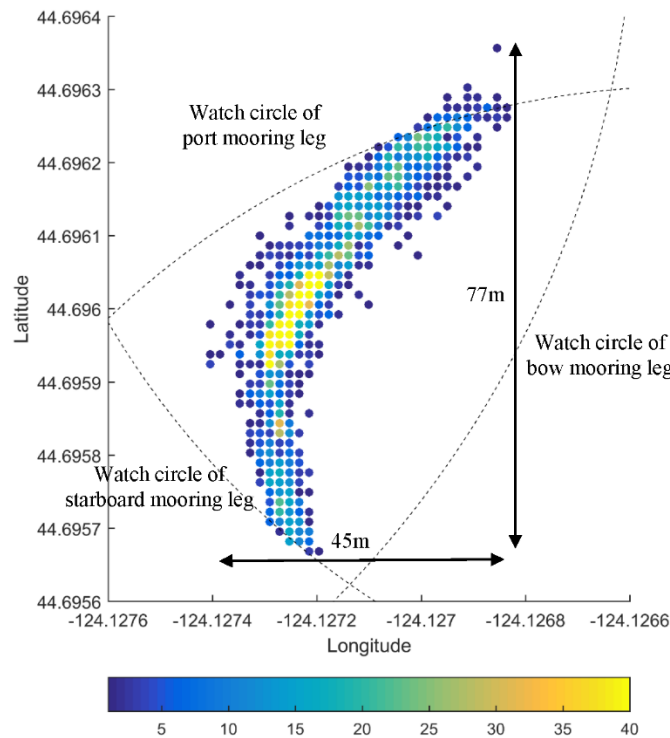


Figure 3-10. Number of occurrences of the Ocean Sentinel positions and watch circle

As mentioned earlier in Section 3.6.1.1, the bow, port and starboard mooring chains are at stage A or B under their largest mean mooring tensions. Therefore, the boundary of the OS position domain can be approximated by the watch circles of the bow, port and starboard mooring legs assuming that the surface buoys were mainly on the sea surface during the field test.

The watch circle of each mooring leg (black dashed line) is plotted in Figure 3-10 using the anchor position as the center point and the radius R calculated as:

$$R = L_p + \sqrt{L^2 - H^2} \quad \text{Eq. (3.18)}$$

Comparing the OS positions with the watch circles, the followings are found: first, the OS was quite close to the starboard watch circle when the OS moved to the south edge of its position domain; second, the OS was outside the port watch circle when the OS moved to the northeast edge with the largest distance of 11 m, which was probably caused by the submergence of the port surface buoy; and third, the OS was at least 5.8 m inside of the bow watch circle.

3.6.3 Directional control of the OS

To study the directional control of the OS, time history of the OS heading direction is plotted in Figure 3-11. The range of the heading direction was from 38° to 112° . This indicates a good direction control of the OS through the spread mooring system with three mooring legs which successfully prevented entanglement of mooring lines and umbilical cable. Note that 0° corresponds to the direction when the OS is pointing to the north and 90° corresponds to the direction when the OS is pointing to the west.

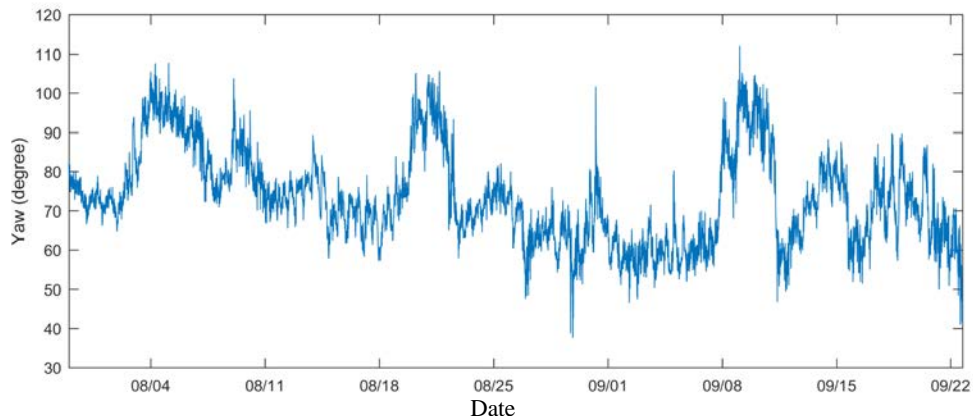
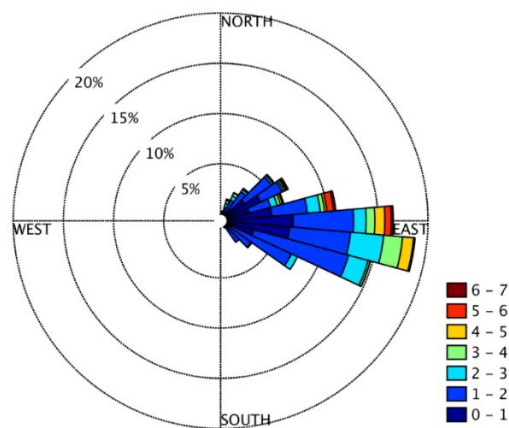


Figure 3-11. Time history of the OS heading direction

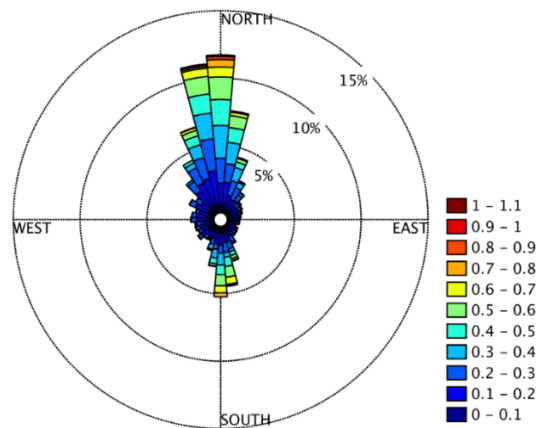
3.6.4 Wave, current and wind influences on mooring tensions

3.6.4.1 Directional distributions of waves, current and wind

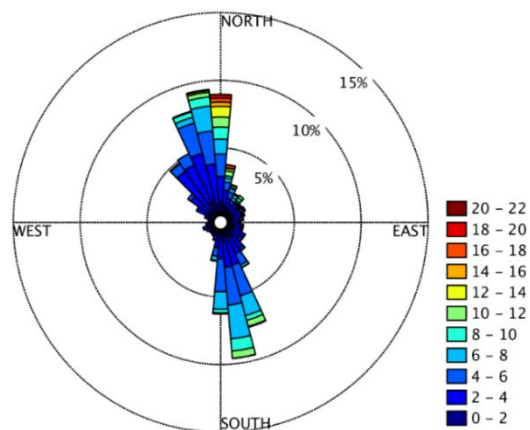
The directional distributions of waves, current and wind during the field test (from 07/29/13 to 10/03/13) are plotted in Figure 3-12 using corresponding rose diagrams. Each rose diagram shows the frequencies and magnitudes of significant wave height, surface current speed or wind speed in 36 angle bins: the color band of each bin indicates the magnitude range and its frequency; the total length of each bin indicates the total frequency in one direction range.



(a) Directional distribution of significant wave height (unit: m)



(b) Directional distribution of surface current speed (unit: m/s)



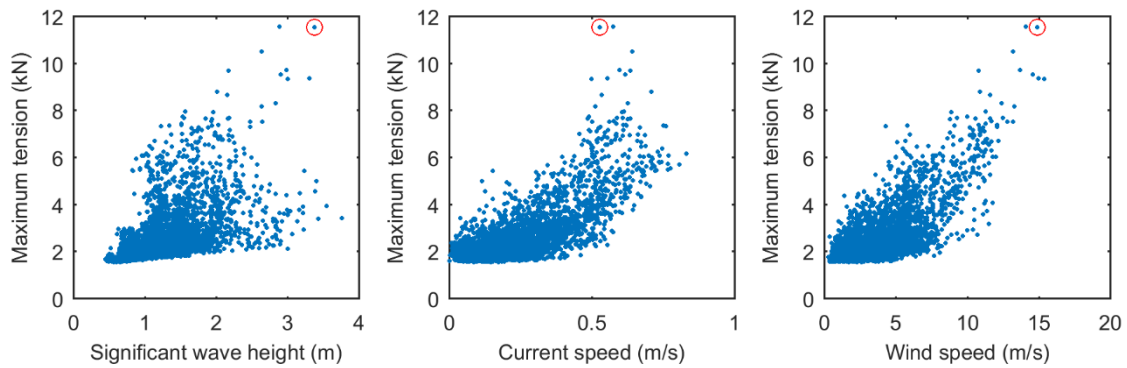
(c) Directional distribution of wind speed (unit: m/s)

Figure 3-12. Directional distribution of waves, current and wind during the field test of the Ocean Sentinel

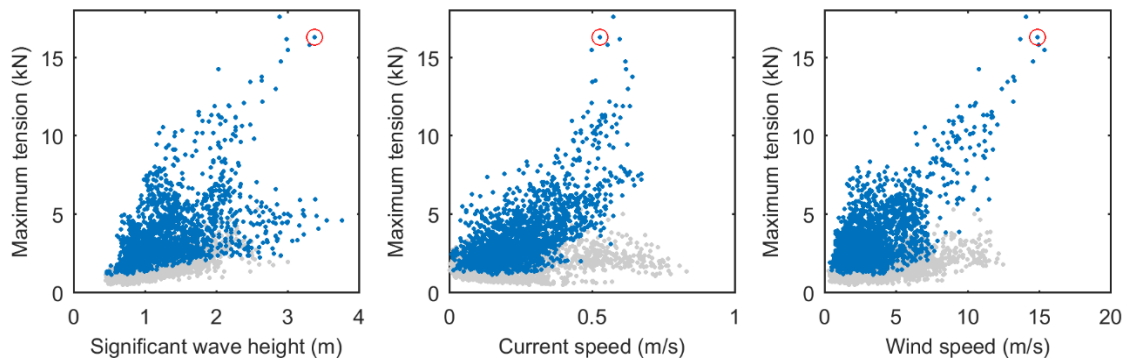
As demonstrated in Figure 3-12, the primary direction was toward the east for the waves, and it was toward either the north or south for both the current and wind. In addition, the extreme wave height most likely occurred when waves were propagating toward the east; the extreme current and wind speeds most likely occurred when they were propagating toward the north.

3.6.4.2 Correlations between mooring tensions and waves, current and wind conditions

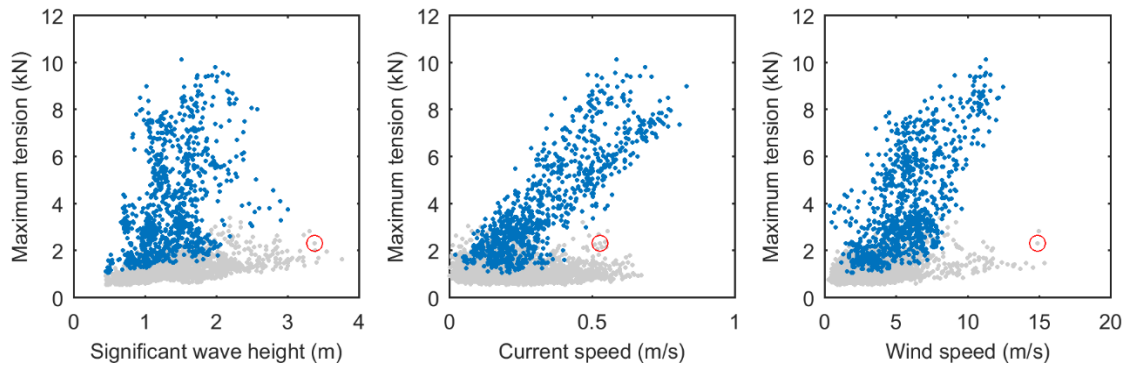
The correlation between environmental conditions and mooring tensions acting on the OS during the field test is investigated by comparing measured waves, current and wind conditions with measured mooring tensions. In Figure 3-13(a-c), the blue points plot the environmental conditions (significant wave heights, surface current speeds and wind speeds) and their corresponding maximum mooring tensions for every 20 minutes for the individual bow, port and starboard mooring legs. The red circles plot the bow, port and starboard mooring tensions and their corresponding environmental conditions when the OS started its significant drift at 17:20 on 09/22/2013. Note that when the OS moved to the south (north) region of its position domain (Figure 3-7) under strong current or wind propagating toward the south (north), the port (starboard) mooring leg was in slack condition, in such scenario the maximum mooring tension of the mooring leg was not correlated with environmental conditions. Therefore, instead of blue points, the maximum mooring tensions of slack port and starboard mooring legs (the average mooring tensions of which were less than 0.56 kN) are plotted as grey points in the figure.



(a) Bow mooring leg



(b) Port mooring leg



(c) Starboard mooring leg

- Maximum tension when mooring leg was in slack condition
- Maximum tension when mooring leg was in taut condition
- Maximum tension when significant OS drift started

Figure 3-13. Correlation between environmental conditions and maximum mooring tensions for every 20 minutes

The significant wave height, current speed and wind speed are shown to correlate closely to the mooring tensions on the OS, because the maximum mooring tension generally

increases with the significant wave height, current speed or wind speed respectively for each mooring leg. However, there are some relatively small maximums of bow, port or starboard mooring tensions under large significant wave height, which correspond to the scenarios with large waves but small current.

The strong correlation between each environmental condition (waves, current or wind) and mooring loads is also demonstrated by the large value of significant wave height, current speed or wind speed when the significant OS drift started. At the time of significant OS drift, the bow and port maximum mooring tensions (marked in red circles in Figure 3-13 a-b) almost reached their highest values. Meanwhile, the significant wave height and wind speed were quite close to their largest values; and the current speed was about $2/3$ of its largest value. Note that the maximum starboard mooring tension (marked by the red circles in Figure 3-13c) was relatively small when the significant OS drift started, because the starboard mooring leg was in slack condition.

Based on the above discussions, all the environmental conditions (waves, current and wind) should be taken into account for accurate prediction of mooring tensions in designing the OS mooring system and other similar WEC mooring systems.

3.7 Survivability Characteristics of the OS Mooring System

3.7.1 Quasi-static analysis of anchor movability

The OS drifted significantly out of its position domain near the end of the field test, which likely caused one or more anchors be dragged away from their original positions. To study the anchor movability, the reserved capacity of each anchor is calculated as

$$C_r = c(W_a - F_{bv}) - F_{bh} = \overbrace{c \cdot W_a}^{F_r} - \overbrace{(c \cdot F_{bv} + F_{bh})}^{F_e} \quad \text{Eq. (3.19)}$$

$$F_r = c \cdot W_a \quad \text{Eq. (3.20)}$$

$$F_e = c \cdot F_{bv} + F_{bh} \quad \text{Eq. (3.21)}$$

where C_r is the anchor reserved capacity; c is the friction coefficient between anchor and seafloor (0.74 for concrete anchor at Oolitic sand (SST, 2009)); W_a is the submerged weight of anchor (22.28 kN); F_r is defined as the static anchor resistance; and F_e is defined as the effective force.

If the anchor reserved capacity is positive, which means the effective force is smaller than the static anchor resistance, the anchor does not move; if the anchor reserved capacity is negative, which means the effective force is larger than the static anchor resistance, the anchor is dragged. Therefore, the anchor movability can be indicated by the ratio (r_a) of effective force to static anchor resistance, which is shown in the follow equations:

$$r_a = \frac{F_e}{F_r} = \frac{c \cdot F_{bv} + F_{bh}}{c \cdot W_a} \begin{cases} \leq 1 & \text{no anchor movement} \\ > 1 & \text{anchor movement} \end{cases} \quad \text{Eq. (3.22)}$$

Based on the catenary equations of mooring chain (Eq. 3.1-15), the quasi-static r_a can be calculated as a function of the mooring tension on the OS F_o for the individual bow, port and starboard mooring legs (see Figure 3-14). Comparing the quasi-static r_a with respect to the maximum of measured mooring tensions (during the period of the significant OS drift and the time before) to unity, movabilities of the bow, port and starboard anchors are discussed as follows: (1) The bow anchor likely stayed in its original position, because the value of r_a (0.85) with respect to the maximum of measured bow mooring tensions (11.6 kN) is smaller than one; (2) The starboard anchor likely stayed in its original position, because the value of r_a (0.95) with respect to the maximum of measured starboard mooring

tensions (10.1 kN) is small than one; (3) The port anchor was likely dragged out of its original position during the significant OS drift, because the value of r_a (1.33) with respect to the maximum of measured port mooring tensions during this period (16.3 kN) is larger than one. Note that the quasi-static value of r_a only provides preliminary investigation of anchor movement, for more accurate investigation of anchor movement, calculating the instantaneous value of r_a through dynamic analysis is suggested.

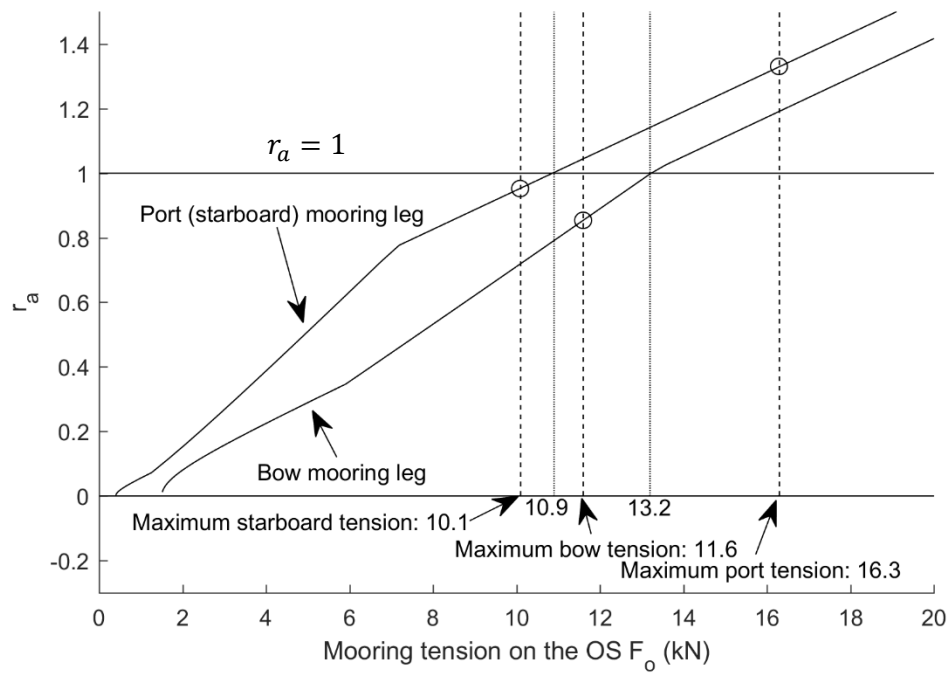


Figure 3-14. The quasi-static ratio (r_a) of effective force to anchor resistance with respect to the mooring tension on the OS (F_o)

In Figure 3-14, the L/H ratio is shown to be an important factor affecting the anchor movability indicated by the value of r_a : (1) Under the same mooring tension F_o , r_a of the bow mooring leg ($L/H = 1.8$) is larger than r_a of the port and starboard mooring legs (L/H

= 1.2); and (2) When $r_a = 1$, the corresponding F_o for the bow mooring leg (13.2 kN) is larger than the corresponding F_o for the port and starboard mooring legs (10.9 kN).

3.7.2 Strength capacities of mooring lines

The polyester lines of the mooring system had sufficient strength to survive the storms observed in the field test. The maximum measured tensions on the bow, port and starboard polyester lines are 13%, 13% and 5%, respectively, of the strength of the polyester lines (266.9 kN). They are significantly smaller than 60%, which corresponds to the required minimum safety factor of 1.67 in the mooring design guideline (BV, 2015). Other mooring lines (e.g., mooring chains and spectra lines) were shown to have sufficient strength by observation since they did not break in the field test.

Table 3-2. Ratios of maximum tension to mooring line strength

	Bow polyester line	Port polyester line	Starboard polyester line	Design value
Percentage	13%	13%	5%	60%

3.8 A Systematic Procedure of Mooring Design for Anchor Movement Prevention

Based on the above mooring evaluations, a systematic procedure of designing a mooring system with adequate anchor resistance is proposed to prevent anchor movement. The procedural steps and their applications to the OS mooring design are listed as follows:

- (1) Specify a set of extreme environmental conditions including waves, current and wind;

- (2) Estimate static drift forces on the moored structure under the specified extreme environmental conditions;
- (3) Specify new mooring configurations by selecting appropriate numbers of mooring legs and properties of mooring chains (e.g., the L/H ratio in this study) so that the following two goals are met: firstly, the mean mooring tension of any mooring leg is relatively small under the drift forces; secondly, the tension increasing slope of the quasi-static excursion-tension curve of any mooring leg is relatively small under the mean mooring tension;
- (4) Specify a relatively small pre-tension on each mooring leg to enable an easy mooring installation, and calculate the corresponding anchor positions for each mooring configuration using the quasi-static analysis;
- (5) Obtain the maximum of instantaneous effective force of each mooring configuration through dynamic simulations under the specified extreme environmental conditions, and determine the optimum mooring configuration with the smallest maximum; and
- (6) Determine the design value of static anchor resistance based on both the maximum of instantaneous effective force of the optimum mooring configuration and the design equation.

In step1, it has been shown earlier that the waves, current and wind all correlated closely to the maximum mooring tension. Therefore, an extreme value is specified for the waves, current and wind individually. The extreme environmental conditions for the OS mooring system are determined as follows (listed in Table 3-3): the extreme significant wave height,

wind speed and current speed are specified to be their corresponding 10 year return levels for the period from July to September, which is estimated using the extreme value theory; the directions of the wind, waves and current are collinear and range from 180° to 360° with a spacing of 30° . (180° corresponds to the direction when the waves, wind and current are propagating to the south; 270° corresponds to the direction when they are propagating to the east.) Note that the OS was deployed 3-5km west of the Oregon coast, so the waves with directions from 30° to 150° (generally propagating to the west) are negligible and not considered in this study.

Table 3-3. Specified extreme environmental conditions

Wave			Wind speed (m/s)	Current speed (m/s)	Collinear directions
Significant wave height (m)	Peak period (s)	Spectrum			
6.1	13.2	JONSWAP	14.7	0.76	$180^\circ, 270^\circ, \dots 360^\circ$

Comparing the extreme environmental conditions in the original design to both the statistically estimated extreme conditions and the measured extreme conditions during the field test (see Table 3-4), it is found that the extreme environmental conditions of average wind speed and current speed were underestimated in the original design.

Table 3-4. Extreme environmental conditions in the original design, field test and statistical estimation

	Original design values	Maximum of field test measurement	10 year return level
Significant wave height (m)	7.0	6.73	6.1
Average wind speed (m/s)	10.0	20.6	14.7
Current speed (m/s)	0.51	1.01	0.76

In step 2, based on the Morison equation and specified extreme conditions, the maximum static current loads on the OS are 0.97 kN and 3.00 kN in the surge and sway directions, respectively; and the static wind loads on the OS are 0.22 kN and 0.65 kN in the surge and sway directions, respectively. If both the current and wind loads are mainly supported by only one mooring leg, which could be the case for the original three-legs mooring design, the average tension on the OS acted by the mooring leg is approximated to be as large as 3.65 kN. According to the excursion-tension relationship of the OS (see Figure 3-9), the corresponding dynamic mooring tension is expected to be quite large under such average mooring tension. To reduce the dynamic mooring tension, more than three mooring legs are suggested for the new mooring configurations.

In step 3, for the new mooring configurations of the OS, six mooring legs are selected (see Figure 3-15). The heading direction of the OS faces the north, which is the primary direction of current and wind at the NETS. With different values of mooring chain length, the new mooring configurations are listed and numbered in Table 3-5. The selected mooring chain lengths are 55, 63, 72 and 82 m, which correspond to L/H ratios of 1.2, 1.4,

1.6 and 1.8, respectively. (Note that 55 and 82 m are the lengths of the port (starboard) and bow mooring chains respectively in the original mooring design.) To investigate the efficiency of six-leg mooring configurations in reducing anchor pulling force, the three-leg mooring configurations with L/H ratios of 1.2, 1.4, 1.6 and 1.8 are also studied (listed in Table 3-5).

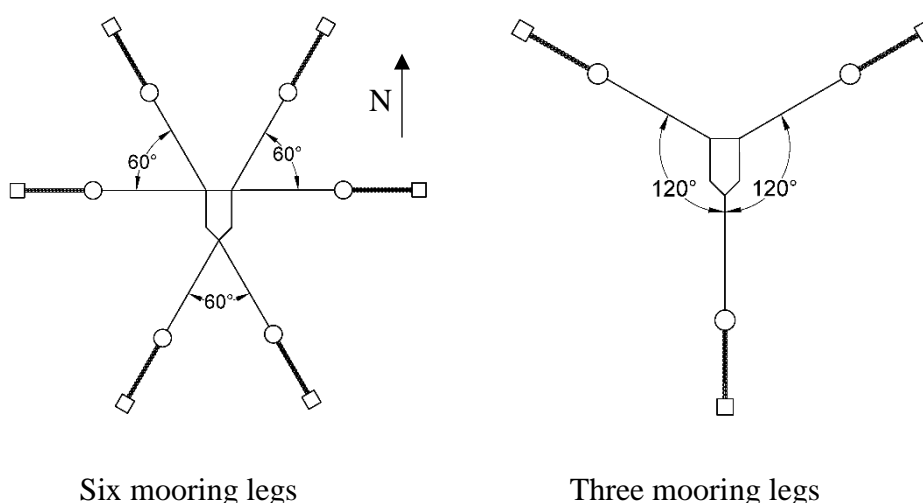


Figure 3-15. Mooring configurations of six and three legs

Table 3-5. Selected new mooring configurations

Number of mooring configuration	1	2	3	4
L/H ratio	1.2	1.4	1.6	1.8
Number of mooring legs	6			
Number of mooring configuration	5	6	7	8
L/H ratio	1.2	1.4	1.6	1.8
Number of mooring legs	3			

In step 4, for a relatively easy mooring installation, the initial tension on polyester lines during mooring installation is specified to be a small value (0.5 kN in this study). Based on this value of polyester line tension and catenary equations of mooring chains, the initial horizontal excursions of mooring anchors relative to the OS are calculated and listed in Table 3-6.

Table 3-6. Initial horizontal excursions of mooring anchors relative to the OS

L/H ratio of mooring chain	1.2	1.4	1.6	1.8
Initial excursion of mooring anchor (m)	20.1	28.5	37.6	47.1

In step 5, the instantaneous effective force of each selected mooring configuration is predicted through a numerical simulation of 3 hours under the specified extreme environmental conditions, using a commercial code OrcaFlex. Comparing the maximums of instantaneous effective force for all the mooring configurations (listed in Table 3-7), the mooring configuration with the smallest maximum is selected, which is the six-leg mooring configuration with L/H ratio of 1.2. The maximum of instantaneous effective force of this configuration is 33.2 kN.

Table 3-7. Maximum of instantaneous effective force for each new mooring configuration

	Number of mooring configuration			
	1	2	3	4
Maximum of instantaneous effective force (kN)	33.2	38.1	40.8	38.1
	Number of mooring configuration			
	4	5	6	7
Maximum of instantaneous effective force (kN)	45.8	47.9	48.1	43.6

Finally, in step 6, the design value of static anchor resistance is calculated based on both the maximum of instantaneous effective force of the optimum mooring configuration and the design equation, which takes into account the safety factor of 1.5 (API, 1997):

$$r_a = \frac{F_e}{F_r} = \frac{c \cdot F_{bv} + F_{bh}}{c \cdot W_a} \leq \frac{2}{3} \quad \text{Eq. (3.23)}$$

Through the above equation, the new design value of static anchor resistance for the OS mooring system is 49.8 kN (its comparison to the value of static anchor resistance in the original design is listed in Table 3-8). This new design value can be provided by a concrete gravity anchor of 67.3 kN submerged weight deployed at the NETS (with friction coefficient $c = 0.74$).

Table 3-8. Mooring anchor design for the optimum mooring configuration #1

Calculated maximum of instantaneous effective force (kN)	New design value of static anchor resistance (kN)	Original design value of static anchor resistance (kN)
33.2	49.8	16.5

3.9 Concluding Remarks

This study presented a multi-body catenary spread mooring system design of a mobile ocean test berth, the Ocean Sentinel (OS) instrumentation buoy, deployed to facilitate ocean testing of wave energy converters (WECs). Then the mooring design was evaluated through both the results of a quasi-static study and the systematic analysis of extensive data of OS positions, mooring tensions and field waves, wind and current conditions obtained in the 2013 OS field test. The global characteristics and survivability characteristics of the mooring system were examined, which provided insights for further designs of the OS and similar WEC mooring systems.

The global characteristics of the OS mooring system were determined as follows:

- i. The relationship between the OS excursion and mean mooring tension for every 20 minutes is close to the quasi-static excursion-tension curve of the OS for the individual bow, port and starboard mooring legs. As the OS excursion increases, the mean mooring tension gradually increases with a steeper increasing slope.
- ii. The relationship between the OS excursion and maximum mooring tension for every 20 minutes differs from the quasi-static excursion-tension curve of the OS for the individual bow, port and starboard mooring legs. At large excursion the mooring stiffness of each leg (deployed at shallow water depth) becomes very steep, in which scenario the dynamic mooring tension is quite significant under the large-amplitude OS motions induced by strong waves. This phenomenon is demonstrated by the large difference between the maximum and mean mooring tensions at large OS excursion.

- iii. The three-leg spread mooring design of the OS limited the buoy movement inside a small position domain of 77 m long and 45 m wide, and limited the weathervane angle of the OS heading direction within a range of 38-112 degrees. The OS position domain can be approximated by the watch circles of the bow, port and starboard mooring legs, because the surface buoys of the mooring system were mainly on the sea surface under the mean mooring tensions of the field test.
- iv. In the field test, the primary direction was toward the east for the waves, and toward either the north or south for both the current and wind. The wave, wind and current conditions all correlated closely to the mooring tensions during the field test. Therefore, all these environmental conditions should be taken into account in the mooring design to estimate mooring tensions accurately.

The survivability characteristics of the OS mooring system were determined as follows:

- i. Through calculating the quasi-static ratio r_a of effective force to static anchor resistance with respect to the individual maximums of bow, port and starboard mooring tensions on the OS, the movability of each anchor is estimated as follows: the port anchor was likely dragged during the significant OS drift; and the bow and starboard anchors likely experienced no movements. Note that the quasi-static value of r_a only provides preliminary investigation of anchor movement, for more accurate investigation of anchor movement, calculating the instantaneous value of r_a through dynamic analysis is suggested.
- ii. The polyester lines of the mooring system had sufficient strength to survive the storms observed in the field test. The measured maximum loads on the bow, port and starboard polyester lines were only 13%, 13% and 5%, respectively, of the

designed mooring line strength. They are significantly smaller than 60%, which corresponds to the minimum safety factor of 1.67 in the mooring design guideline. Based on the mooring evaluations and analysis above, a new systematic procedure of designing a mooring system with adequate anchor resistance is developed independently. The design procedure incorporates the major findings of this study. Specifically, the design values of the extreme current and wind conditions, which were underestimated in the original design, need to be selected judiciously besides the well estimated extreme wave condition; secondly, the quasi-static analysis is useful in preliminary selections of the appropriate numbers of mooring legs and mooring chains properties for new mooring configurations; thirdly, dynamic simulations are important in predicting instantaneous effective force and determining the optimum mooring configuration with the smallest maximum of effective force.

Applying the new mooring design procedure to the OS mooring system, the resulting mooring configuration facing the south with six mooring legs and L/H ratio of 1.2 was found to have the smallest maximum of effective force (33.2 kN). Taking into account the 1.5 safety factor in the anchor design, the design value of static anchor resistance is 49.8 kN. This frictional resistance force would be provided by a concrete gravity anchor of 67.3 kN submerged weight deployed at the NETS.

3.10 Acknowledgements

Financial support from the Department of Energy Grant No. DE-FG36-08GO18179-M001 is gratefully acknowledged.

3.11 References

- Ambühl, S., Sterndorff, M., & Sørensen, J. D. (2014). Extrapolation of Extreme Response for Different Mooring Line Systems of Floating Wave Energy Converters. *International Journal of Marine Energy*, 7, 1-19.
- Amon, E., Brekken, T. K. A., & von Jouanne, A. (2011). A Power Analysis and Data Acquisition System for Ocean Wave Energy Device Testing. *Renewable Energy*, 36(7), 1922-1930. doi:10.1016/j.renene.2010.12.016
- API. (1997). API-RP-2SK Recommended Practice for Design and Analysis of Stationkeeping Systems for Floating Structures.
- API. (2007). API BULLETIN 2INT-MET Interim Guidance on Hurricane Conditions in the Gulf of Mexico.
- Baker, J. L. (2013). *Mooring Analysis of the Ocean Sentinel through Field Observation and Numerical Simulation*. (Master of Science), Oregon State University.
- Brekken, T. K. A., Rhinefrank, K., von Jouanne, A., Schacher, A., Prudell, J., & Hammagren, E. (2013). Scaled Development of a Novel Wave Energy Converter Including Numerical Analysis and High-Resolution Tank Testing. *Proceedings of the Ieee*, 101(4), 866-875. doi:10.1109/jproc.2012.2234711
- BV. (2015). NR 493 DT R03 E Classification of Mooring Systems for Permanent and Mobile Offshore Units.
- CMPT. (1998). Floating Structures: A Guide for the Design and Analysis.
- DNV. (2013). DNV-OS-E301 Position Mooring: DET NORSKE VERITAS.
- Fitzgerald, J., & Bergdahl, L. (2007). *Considering Mooring Cables for Offshore Wave Energy Conversions*. Paper presented at the 7th European Wave and Tidal Energy Conference, Oporto.
- Hald, T., & Frigaard, P. B. (2001). *Forces and Overtopping on 2. Generation Wave Dragon for Nisum Bredning*. Aalborg University.
- Harnois, V., Johanning, L., & Thies, P. R. (2013). Wave Conditions Inducing Extreme Mooring Loads on a Dynamically Responding Moored Structure.
- Harnois, V., Parish, D., & Johanning, L. (2012). *Physical Measurement of a Slow Drag of a Drag Embedment Anchor during Sea Trials*. Paper presented at the 4th International Conference on Ocean Energy, Dublin.
- Harnois, V., Weller, S. D., Johanning, L., Thies, P. R., Le Boulluec, M., Le Roux, D., Soule, V., & Ohana, J. (2015). Numerical Model Validation for Mooring Systems: Method and Application for Wave Energy Converters. *Renewable Energy*, 75, 869-887. doi:10.1016/j.renene.2014.10.063
- Harris, R. E., Johanning, L., & Wolfram, J. (2004). *Mooring Systems for Wave Energy Converters: A Review of Design Issues and Choices*. Paper presented at the Marec2004.
- Johanning, L., Smith, G. H., & Wolfram, J. (2007). Measurements of Static and Dynamic Mooring Line Damping and their Importance for Floating WEC Devices. *Ocean Engineering*, 34(14-15), 1918-1934. doi:10.1016/j.oceaneng.2007.04.002
- Kofoed, J. P., Frigaard, P., Friis-Madsen, E., & Sorensen, H. C. (2006). Prototype Testing of the Wave Energy Converter Wave Dragon. *Renewable Energy*, 31(2), 181-189. doi:10.1016/j.renene.2005.09.005

- Lettenmaier, T., von Jouanne, A., Amon, E., Moran, S., & Gardiner, A. (2013). Testing the WET-NZ Wave Energy Converter Using the Ocean Sentinel Instrumentation Buoy. *Marine Technology Society Journal*, 47(4), 164-176.
- Martinelli, L., Ruol, P., & Cortellazzo, G. (2012). On Mooring Design of Wave Energy Converters: the Seabreath Application. *Coastal Engineering Proceedings*, 1(33), 3.
- Martinelli, L., Spiandorello, A., Lamberti, A., & Ruol, P. (2010). *Dynamic Model for Catenary Mooring: Experimental Validation of the Wave Induced Load*. Paper presented at the The COMSOL Conference.
- Palm, J., Paredes, G. M., Eskilsson, C., Pinto, F. T., & Bergdahl, L. (2013). *Simulation of Mooring Cable Dynamics Using a Discontinuous Galerkin Method*. Paper presented at the In Proceedings of 5th International Conference on Computational Methods in Marine Engineering, Hamburg, Germany.
- Parmeggiani, S., Kofoed, J. P., & Friis-Madsen, E. (2013). Experimental Study Related to the Mooring Design for the 1.5 MW Wave Dragon WEC Demonstrator at DanWEC. *Energies*, 6(4), 1863-1886. doi:10.3390/en6041863
- Ricci, P., Rico, A., Ruiz-Minguela, P., Boscolo, F., & Villate, J. L. (2012). *Design, Modelling and Analysis of an Integrated Mooring System for Wave Energy Arrays*. Paper presented at the In Proceedings of the 4th International Conference on Ocean Energy.
- Rodríguez, R., Gorroategui, I., Vidal, C., Guanche, R., Cañizal, J., Fraguera, J. A., & Díaz, V. (2011). *Anchoring Systems for Marine Renewable Energies Offshore Platforms.* Paper presented at the In OCEANS, 2011 IEEE-Spain.
- Ruiz-Minguela, J. P., Rodríguez, R., Ricci, P., Marón, A., Prieto, M. E., & Taboada, M. (2008). *Design and Testing of the Mooring System for a New Offshore Wave Energy Converter*. Paper presented at the In Proc. 2nd International Conference on Ocean Energy.
- Salcedo, F., Ruiz-Minguela, P., Rodriguez, R., Ricci, P., & Santos, M. (2009). *Oceantec: Sea Trials of a Quarter Scale Prototype*. Paper presented at the In Proceedings of 8th European Wave Tidal Energy Conference.
- SST. (2009). Advanced Anchoring and Mooring Study.
- Thies, P. R., Johanning, L., Harnois, V., Smith, H. C. M., & Parish, D. N. (2014). Mooring Line Fatigue Damage Evaluation for Floating Marine Energy Converters: Field Measurements and Prediction. *Renewable Energy*, 63, 133-144. doi:10.1016/j.renene.2013.08.050
- von Jouanne, A., Lettenmaier, T., Amon, E., Brekken, T., & Phillips, R. (2013). A Novel Ocean Sentinel Instrumentation Buoy for Wave Energy Testing. *Marine Technology Society Journal*, 47(1), 47-54.
- Weller, S., Hardwick, J., Johanning, L., Karimirad, M., Teillant, B., Raventos, A., . . . Sheng, W. (2014). *Deliverable 4.1: A Comprehensive Assessment of the Applicability of Available and Proposed Offshore Mooring and Foundation Technologies and Design Tools for Array Applications*.
- Wolf, N. B. (2012). *The Dynamic Mooring Force on a Wave Energy Converter Moored in a Single Point*. (M.S.), Chalmers University of Technology.

- Zanuttigh, B., Angelelli, E., & Kofoed, J. P. (2013). Effects of Mooring Systems on the Performance of a Wave Activated Body Energy Converter. *Renewable Energy*, 57, 422-431. doi:10.1016/j.renene.2013.02.006
- Zanuttigh, B., Martinelli, L., & Castagnetti, M. (2013). *Screening of Suitable Mooring Systems*.

CHAPTER 4

4. **Dynamic Analysis and Field Test Evaluation of the Catenary Spread Mooring System Design of a Wave Energy Converter Test Platform**

Junhui Lou ^a, Solomon Yim ^{a*}, Joshua Baker ^b, Ean Amon^c and Annette von Jouanne^a

^a Oregon State University, ^b US Navy, ^c Columbia Power Technologies

4.1 Abstract

This study evaluates a multi-catenary spread mooring system design of a mobile ocean test berth (MOTB) for wave energy converters (WECs), the Ocean Sentinel (OS) instrumentation buoy, through a dynamic analysis model based on the fully coupled method. First, the accuracies of the numerical model in predicting the mooring tensions of the OS mooring system and the OS positions are validated by comparing the numerical results to the field data collected during the 2013 OS field test. Then, the anchor movability, fatigue damage and extreme mooring tension of the OS mooring system are investigated using the mooring tensions predicted by the numerical model. The results of the above studies are summarized as follows: (1) The numerical model provides accurate predictions of the mooring tensions and OS positions under harsh environmental conditions; (2) When the OS drifted significantly near the end of the field test, the bow, port and starboard anchors were likely not dragged, dragged significantly and dragged slightly, respectively; (3) The fatigue damages of mooring lines are predicted for environmental conditions from low to high sea states; and (4) The strengths of mooring lines in the original mooring design are adequate compared to the predicted extreme mooring tensions.

Keywords: Wave energy converter, mooring design, field test, fully coupled method, anchor movement, fatigue damage, extreme mooring tension

4.2 Introduction

Wave energy converters (WECs), which harvest energy from the ocean via various mechanisms (e.g., oscillation or rotation), have been developing progressively toward commercialization over the last decades. Among the various types of WECs, floating WECs operating at or near the ocean surface need to be kept in position by installing mooring systems.

Because of the relatively high cost of mooring system (mooring components and installation) for the floating WEC (was estimated to be 20% of the total cost for a representative floating WEC system (LCICG, 2012)), the cost efficiency of mooring design becomes very important. One important tool to design such a mooring system is a numerical model which can predict mooring tensions accurately. Based on the numerical model, we can determine the minimum strengths of mooring lines and hold capacities of anchors, and select the corresponding mooring lines and anchors. Additionally, we can estimate and verify the fatigue damages of the selected mooring lines.

The numerical model applied in this study is based on the fully coupled method. This method calculates the dynamic responses of the floating structure and its mooring system simultaneously (Ormberg and Larsen, 1998). Comparing to the uncoupled method which calculates the dynamic response of the floating structure in one step and

the dynamic response of its mooring system in another step, the fully coupled method is more accurate when the dynamic interaction between the floating structure and mooring system is strong. The fully coupled method has been implemented based on different numerical algorithms, including the finite element, finite difference and lumped parameter algorithms (Gobat and Grosenbaugh, 2006), among which the finite element algorithm is the most widely used. The finite element based fully coupled method has been implemented for many types of conventional floating structures in the oil industry, including turret moored tanks (Ormberg et al., 1997; Ormberg and Larsen, 1998), spars (Chen et al., 2001; Colby et al., 2000; Sethuraman and Venugopal, 2013; Tahar and Kim, 2008), Floating Production and Storage Offloading vessels (FPSOs) (Correa et al., 2002; Garrett, 2005; Garrett et al., 2002; Heurtier et al., 2001), and tension-leg platforms (TLPs) (Ma et al., 2000; Ran, 2000). The numerical codes applied in the above studies include a tool box comprised of SIMO (vessel) and RIFLEX (mooring), DeepCAT (comprised of COUNAT (vessel) + CABLE3D (mooring)), WINPOST, COUPLE, RAMS, Dynasim-A, Prosim and OrcaFlex.

Accuracies of the fully coupled method in predicting mooring tensions of the conventional floating structures have been validated through both wave tank tests (Ormberg et al., 1997; Ran, 2000), and field tests (Tahar et al., 2006). It was found that there were many factors that affect the accuracy of the fully coupled method, for example, level of sea states, type of moored structure (turret moored tank or truss spar), type of mooring lines (catenary or taut mooring) and ratio of mooring line length L to water depth H .

Comparing to conventional floating structures, floating WECs have their own characteristics. For example, floating WECs generally have relatively small dimensions compared to the typical ocean wind generated wave lengths (60 m to 150 m), and are deployed in shallow to intermediate water depths (less than 150 m (API, 2007)) (Weller et al., 2014). To validate accuracies of the fully coupled method for floating WECs, wave tank tests were conducted for a catenary mooring line of a cylindrical drum buoy (Johanning et al., 2007) and a three-leg catenary mooring system of an instrumented buoy (Harnois et al., 2015). However, there are some limitations in these two wave tank tests: in Johanning et al. (2007), the displacement of the drum buoy was prescribed, which means that the mooring system does not affect the motion of the drum buoy; in Harnois et al. (2015), only waves were generated (no wind and current).

Other than the approximated environmental conditions in the wave tank tests, field tests of WEC mooring systems can validate the fully coupled method in true ocean environments with waves, wind and current. In Harnois et al. (2015), a field test was used to validate the fully couple method. However, large differences between predicted and measured mooring tensions were found because of the unknown anchor position.

In this study, the multi-body catenary spread mooring system design of a mobile ocean test berth (MOTB) for wave energy converters (WECs) (Amon et al., 2011; von Jouanne et al., 2013), named the Ocean Sentinel (OS), with a mooring system similar to conventional point absorber WEC mooring systems, is evaluated through dynamic analysis using a numerical model based on the fully coupled method. In Section 4.3, algorithms of the numerical model are presented in detail. In Section 4.4, the accuracies

of the numerical model in predicting mooring tensions and OS positions are validated through comparing the numerical predictions to field data collected in the 2013 OS field test. Four typical scenarios with harsh environmental conditions are selected for validation. The factors affecting the prediction accuracy of the numerical model are discussed through the studies of the OS mooring system and other mooring systems in the literature (Harnois et al., 2015; Ormberg et al., 1997; Ran, 2000; Tahar et al., 2006). In section 4.5, the fully coupled method is used to predict the unknown mooring tensions on the anchors to investigate the anchor movability when the OS drifted significantly near the end of the field test. In Section 4.6, fatigue damages of the mooring system are evaluated by predicting dynamic mooring tensions using the fully coupled method. The predicted fatigue damages are compared to the measured fatigue damages during the field test. In Section 4.7, extreme mooring tensions of the mooring system are estimated under specified extreme environmental conditions, which are obtained using the extreme value theory.

4.3 Numerical Model Based on the Fully Coupled Method

In this study, we use a numerical code based on the fully coupled method (OrcaFlex). There are three types of structures in the numerical model: the large volume structure (e.g., ships), the slender structure (e.g., mooring lines and risers) and the small volume structure (e.g., floating buoys). The large volume structure is modeled as a nodal component with 6 degrees of freedom (DOF); the small volume structure is modeled as a nodal component with 3 or 6 DOF; and the slender structure is discretized into a series of line segments (shown in Figure 4-1). Note that each line segment of the slender

structure is a composition of a massless segment and two nodes lumped with segment mass, where the massless segment models the axial, torsional and bending properties of the line segment and the two nodes (located at the two ends of each line segment) model the other properties of the line segment (mass, gravity weight and buoyance).

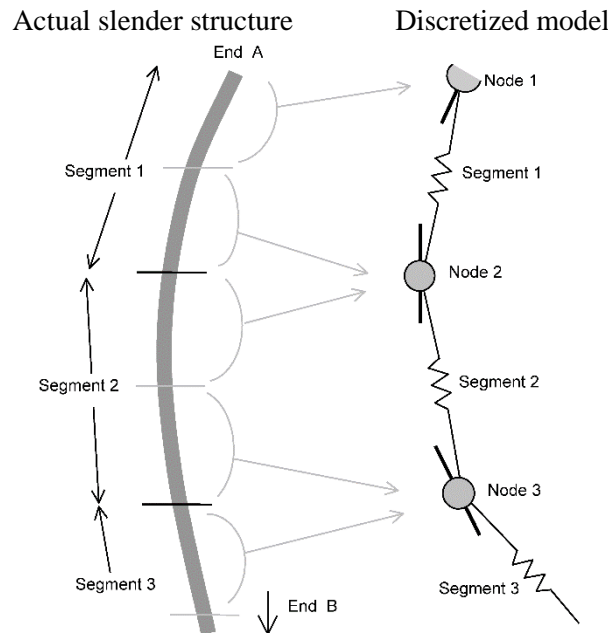


Figure 4-1. Finite element discretization of a slender structure (Orcina, 2009)

The slender structure is connected to the large or small volume structure based on a master-slave scheme. When an end node of a slender structure (slave object) is connected to a large or small volume structure (master object), the position of the end node is determined by the connected large or small volume structure, while in response the end node of the slender structure applies force and moment to the connected large or small volume structure.

The equation of motion for the entire structural system is

$$\mathbf{M}(\mathbf{x})\ddot{\mathbf{x}} + \mathbf{C}(\mathbf{x})\dot{\mathbf{x}} + \mathbf{K}(\mathbf{x})\mathbf{x} = \mathbf{F}_e(\mathbf{x}, \dot{\mathbf{x}}) \quad \text{Eq. (4.1)}$$

where \mathbf{M} is the system mass matrix including structural mass and hydrodynamic mass; \mathbf{C} is the system damping matrix (internal structural damping); \mathbf{K} is the system stiffness matrix (internal structural stiffness); \mathbf{F}_e is external force vector; and \mathbf{x} is structural displacement vector.

For the three types of structures, the external force \mathbf{F}_e are calculated differently:

1) For large volume structures, the external force \mathbf{F}_e is calculated as

$$\mathbf{F}_e = \mathbf{F}_g + \mathbf{F}_h + \mathbf{F}_f + \mathbf{F}_d + \mathbf{F}_r + \mathbf{F}_{\text{drag}_w} + \mathbf{F}_{\text{drag}_a} + \mathbf{F}_m \quad \text{Eq. (4.2)}$$

where \mathbf{F}_g is the gravity force vector; \mathbf{F}_h is the hydrostatic force vector (buoyancy force); \mathbf{F}_f is the Froude-Krylov force vector; \mathbf{F}_d is the diffraction force vector; \mathbf{F}_r is the radiation damping force vector; $\mathbf{F}_{\text{drag}_w}$ is the hydrodynamic force vector; $\mathbf{F}_{\text{drag}_a}$ is the aerodynamic drag force vector; and \mathbf{F}_m is the other forces including connection force, specified force and so on. Note that the added mass is included in the system mass matrix \mathbf{M} of Equation 4.1 for all the three types of structures.

The hydrostatic force \mathbf{F}_h is assumed to be linear and calculated as a product of a hydrostatic stiffness matrix \mathbf{K}_h and a displacement vector \mathbf{x} ; the wave force components (Froude-Krylov force \mathbf{F}_f , diffraction force \mathbf{F}_d , radiation damping \mathbf{F}_r and added mass) are calculated by an external 3D radiation and diffraction program, such as AQWA; the hydrodynamic drag force $\mathbf{F}_{\text{drag}_w}$ and aerodynamic drag force $\mathbf{F}_{\text{drag}_a}$ on each structure node are calculated using the Morison equation

$$\mathbf{F}_{\text{drag}_w} = 1/2 \cdot \rho_w C_d A (u_w - v) |u_w - v| \quad \text{Eq. (4.3)}$$

$$\mathbf{F}_{\text{drag}_a} = 1/2 \cdot \rho_a C_d A (u_a - v) |u_a - v| \quad \text{Eq. (4.4)}$$

where ρ_w is the density of water; ρ_a is the density of air; u_w is the water velocity; u_a is the air velocity; v is the structural velocity; C_d is the drag coefficient and A is the cross-section area.

2) For slender structures, the external force \mathbf{F}_e is calculated as

$$\mathbf{F}_e = \mathbf{F}_g + \mathbf{F}_h + (\mathbf{F}_i + \mathbf{F}_{\text{drag}_w} + \mathbf{F}_{\text{lift}}) \cdot \mathbf{P}_w + \mathbf{F}_{\text{drag}_a} \cdot \mathbf{P}_a + \mathbf{F}_m \quad \text{Eq. (4.5)}$$

where \mathbf{P}_w is the proportion wet of the structure; \mathbf{P}_a is the proportion dry of the structure; \mathbf{F}_{lift} is the hydrodynamic lift force (not included in this study); and \mathbf{F}_i is the fluid inertia force.

The fluid inertia force \mathbf{F}_i on each structure node is calculated as

$$\mathbf{F}_i = \rho V C_m \dot{u} \quad \text{Eq. (4.6)}$$

where V is the volume of the structure, C_m is the inertia coefficient.

3) For small volume structures (6 DOF lumped buoys in this study), the external force \mathbf{F}_e is calculated as

$$\mathbf{F}_e = \mathbf{F}_g + \mathbf{F}_h + (\mathbf{F}_i + \mathbf{F}_r + \mathbf{F}_{\text{drag}_w}) \cdot \mathbf{P}_w + \mathbf{F}_m \quad \text{Eq. (4.7)}$$

4.4 Numerical Model Validation through the Ocean Sentinel (OS) Field test

4.4.1 The OS mooring system field test

The OS was deployed offshore of Newport, OR, at the Northwest National Marine Renewable Energy Center (NNMREC) North Energy Test Site (NETS, which is 3-5 km offshore of the city of Newport, Oregon) in the summer of 2013 to improve understanding of the OS mooring system and validate the numerical model (Baker,

2013). The measured data during the field test include mooring tensions, OS positions, and environmental conditions of wind, current and waves.

Figure 4-2 and Figure 4-3 show the plan and side views of the OS and its multi-body catenary mooring system respectively, with details of mooring components including mooring chains, surface buoys, polyester lines, spectra lines and anchors.

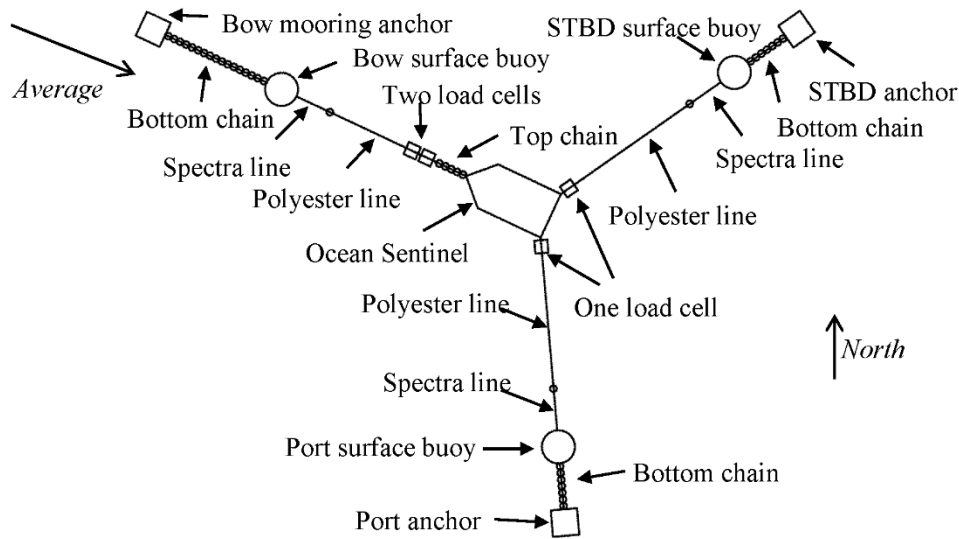


Figure 4-2. Plan view of the three-leg mooring system of the Ocean Sentinel

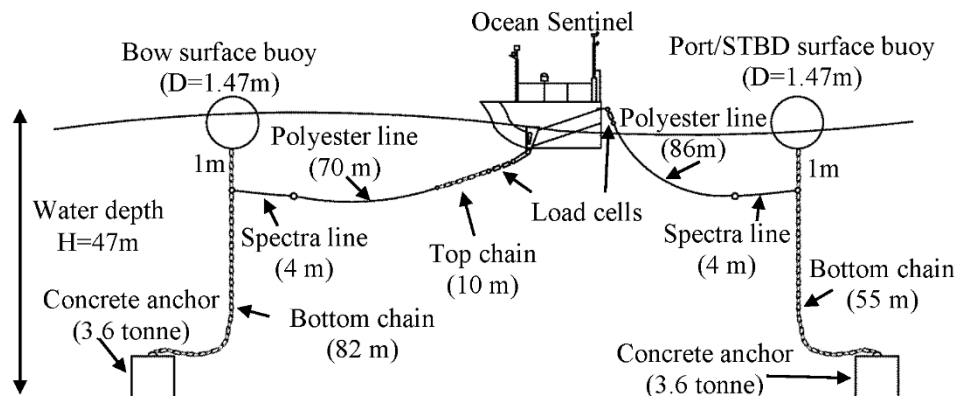


Figure 4-3. Side view of the three-leg mooring system of the Ocean Sentinel

4.4.2 Numerical simulations

4.4.2.1 Modeling of the OS and mooring system

The modeling of the OS and its mooring components are listed as follows: (1) The OS is modeled as a large volume structure; (2) The mooring lines (chains, poly lines and spectra lines) are modeled as slender structures; (3) The surface buoys are modeled as 6 DOF lumped structures; and (4) The anchors are modeled as points fixed on the sea floor. The dimensions, masses and stiffness properties of the OS and its mooring components are listed in Table 4-1 and Table 4-2.

Table 4-1. Dimensions and mass properties of the Ocean Sentinel

Ocean Sentinel	
Length	6.15 m (20.17 ft.)
Width	3.20 m (10.50 ft.)
Height	2.13 m (7.00 ft.)
Draft	1.51 m (4.95 ft.)
Center of gravity	0.81 m (2.66 ft.) below MWL
Mass	8460 kg (18650 lb.)

Table 4-2. Modeling details of mooring components

	Diameter (cm)	Length (m)	# of segments	Mass (kg)	Mass in water (kg)
Bow chain #1	2.5 (wire)	10	33	130	113
Bow chain #2	2.5 (wire)	82	61	1062	927
Starboard (Port) chain	2.5 (wire)	55	48	714	623
Bow polyester line	3.8	70	39	58.9	8.5
Starboard (Port) polyester line	3.8	86	56	72.4	10.4
Spectra line	2.5	4	13	1.5	0.2
Surface buoy	147			308	-1397
Anchor				3600	2273

4.4.2.2 Typical scenarios with harsh waves, wind and current conditions

The OS met various harsh environmental conditions (strong wind, current and waves) including two storms during its 2013 field test. The positions of the OS over the duration of the field test (07/30 through 09/22) are plotted in Figure 4-4. Before 09/22, the OS was located inside a position domain marked by red dashed lines. On 09/22, the OS drifted significantly out of the position domain under a storm. The trajectory of OS positions on 09/22 is shown by blue solid lines in Figure 4-4.

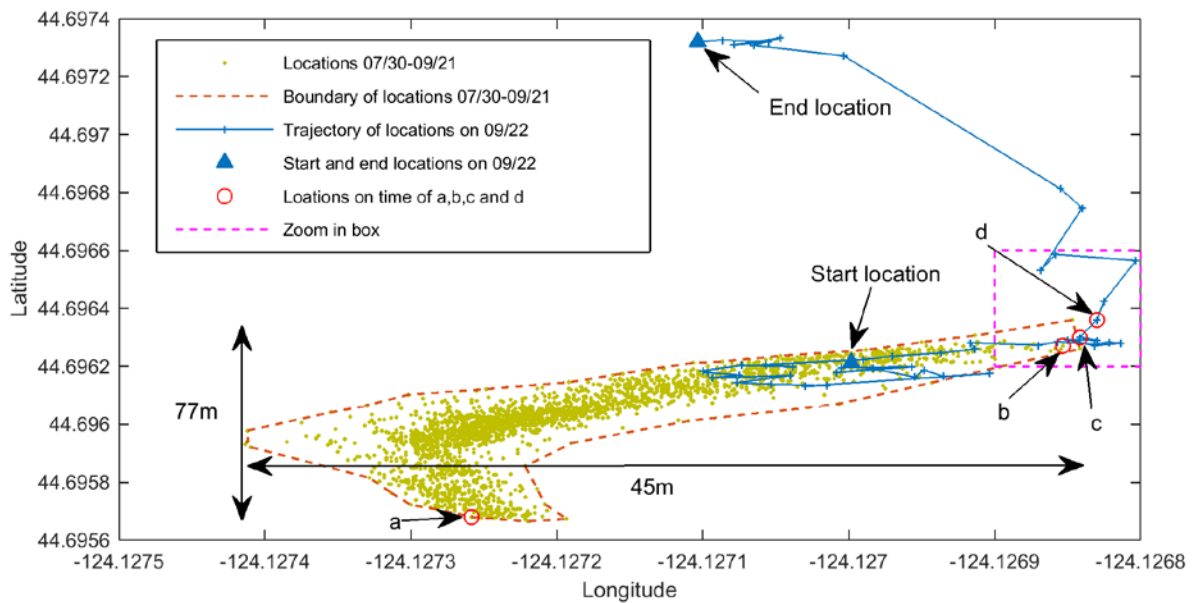


Figure 4-4. GPS positions of the Ocean Sentinel from 07/30 to 09/22 and four typical positions (a, b, c and d) where the Ocean Sentinel was close to or outside its position boundary

To study the dynamic responses of the OS and its mooring system under harsh environmental conditions, four typical scenarios before the significant OS drift, namely A, B, C and D, which correspond to the OS GPS positions a, b, c and d respectively in Figure 4-4, are selected as follows:

- At scenario A (from 14:40pm to 15:00pm on 08/04), the OS was located near the south edge of its space domain. The OS was at position a at both 14:40pm and 15:00pm on 08/04. Therefore, environmental conditions are assumed to be unchanged during this period and the anchors are assumed to be unmoved.
- At scenario B (from 19:40pm to 20:00pm on 08/29), the OS was located near the northeast edge of its position domain. The OS was at position b at both 19:40pm and 20:00pm on 08/29. Therefore, environmental conditions are assumed to be unchanged during this period and the anchors are assumed to be unmoved.
- At scenario C (from 16:40pm to 17:00pm on 09/22), the OS was located near the northeast edge of its position domain. The OS was at position c at both 16:40pm and 17:00pm on 09/22. Therefore, environmental conditions are assumed to be unchanged during this period the anchors are assumed to be unmoved.
- At scenario D (from 17:00pm to 17:20pm on 09/22), the OS was at position c at 17:00pm and drifted a large distance of 6.7 m to position d (outside its position domain) at 17:20pm (see Figure 4-5). In addition, the OS continued drifting another 7.2 m in the following 20 minutes. Therefore, one or more anchors are assumed to be moved significantly during this period.

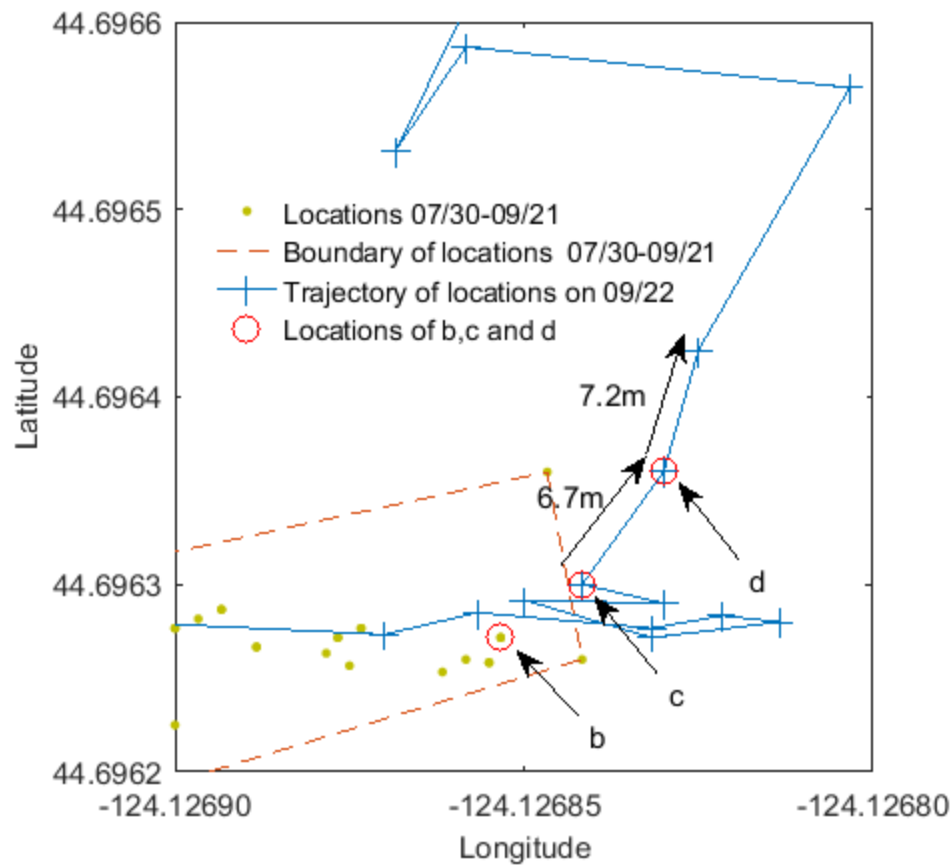


Figure 4-5. Zoom in view of three typical positions (b, c and d) of the Ocean Sentinel

The environmental conditions at these four scenarios are listed in Table 4-3. At scenario A, strong environmental conditions (wind, current and wave) mainly pointing to the south were present; at scenario B, C and D, strong environmental conditions mainly pointing to the north were present. Note that the wind, current and waves directions in this paper are defined as the directions in which they are moving. The direction angle is 0° when the direction is pointing to the north and increases as the direction rotates counter clockwise, e.g., the direction angle is 90° when the direction is pointing to the west.

Table 4-3. Environmental conditions at scenarios of A, B, C and D

Scenario	A	B	C	D
Significant wave height (m)	1.40	2.08	3.17	3.49
Zero crossing period (s)	5.82	5.25	6.27	6.22
Average wave direction (degree)	222	332	313	326
Average wave spread (degree)	36	32	37	33
Average wind speed (m/s)	6.66	13.54	17.68	17.10
Average wind direction (degree)	191	359	365	363
Surface current speed (m/s)	0.80	0.58	0.56	0.53
Surface current direction (degree)	196	355	349	351

The ocean random waves are modeled by a series of wave components with different directions, periods and phases, which produce the same wave frequency spectrum and directional spread spectrum as the measured waves. The modeled wave frequency spectrum at scenario C is demonstrated in Figure 4-6.

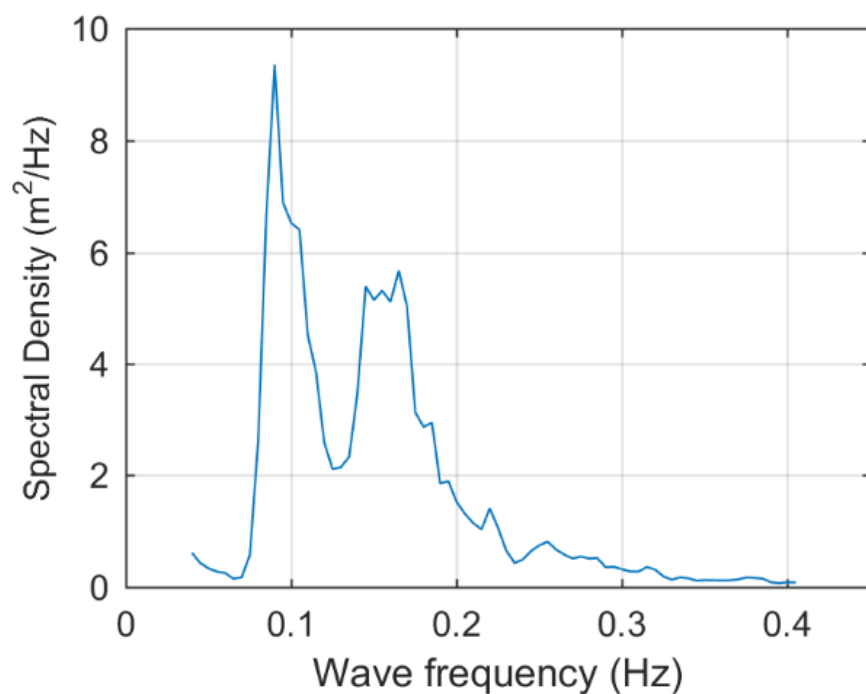


Figure 4-6. Wave spectrum at scenario C

The current is modeled according to the measured current directions and speeds at different water depths. Note that the current profile was only measured at water depths from -2.15 m to -26.65 m. The current speed profile above -2.15 m is based on the interpolation of second order polynomials; and the current profile below -26.65 m is assumed to change linearly until zero speed at the seafloor. The modeled current speed profile at scenario C is demonstrated in Figure 4-7.

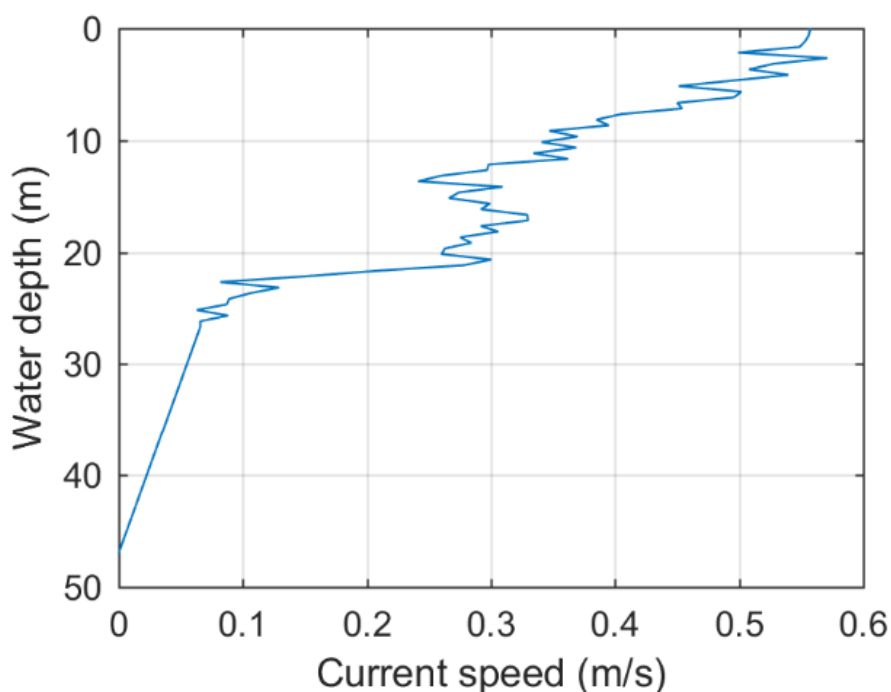


Figure 4-7. Current speed profile along water depth at scenario C

4.4.2.3 Anchor positions adjustment

During the deployment of the OS mooring system, the anchor positions were recorded when anchors were dropped from the utility vessel. Because of the initial horizontal speed of the anchors (close to the vessel speed), the current drift effect and the delay between the time of anchor dropping and the time of GPS recording, the recorded anchor positions can be different from the actual anchor positions on the seafloor (the differences were estimated to be within 11 m (Baker, 2013)).

To investigate the differences between the recorded and actual anchor positions, the numerical excursion-tension curve, which is the quasi-static relationship between the mooring tension on the OS and the horizontal distance (excursion) from the OS to the mooring anchor, is calculated through static analysis of the numerical model and

compared to the experimental excursion-tension curve using the recorded anchor positions.

Figure 4-8 presents the comparison between the numerical excursion-tension curve and the experimental excursion-tension curve with recorded anchor position for individual bow, port and starboard mooring lines. The shapes of the numerical and experimental curves are generally similar to each other. However, there are offsets in excursion between the numerical and experimental curves for the port and starboard mooring lines; and the experimental curve for the bow mooring line bifurcates at larger excursions. Note that each green dot in Figure 4-8 shows the excursion of the OS and the mean mooring tension for every 20 minutes.

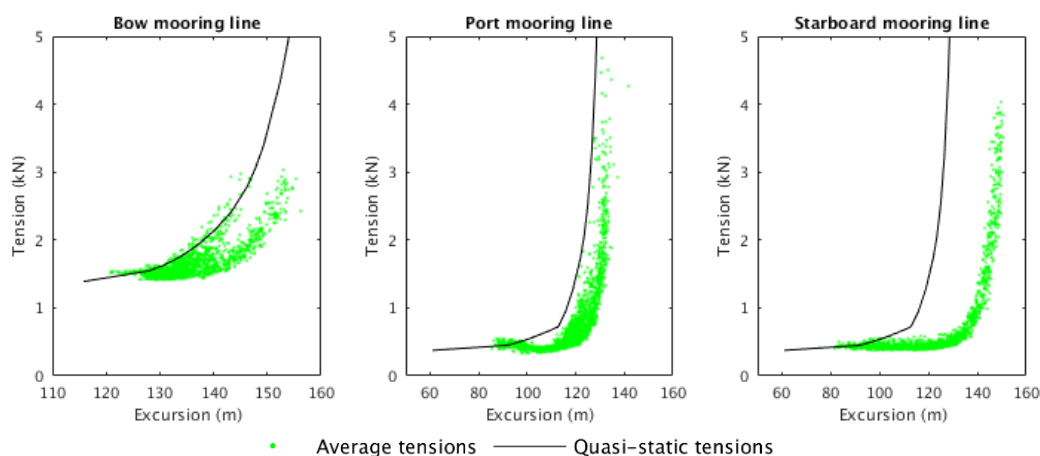


Figure 4-8. Comparison between the numerical excursion-tension curve and the experimental excursion-tension curve with recorded anchor position for individual bow, port and starboard mooring lines

Assuming that the experimental excursion–tension curve with the actual anchor position should be close to the corresponding numerical excursion–tension curve, the horizontal distance from the OS to the actual anchor position can be calculated based on the numerical excursion-tension curve and the average of measured mooring tensions. As illustrated in Figure 4-9, the port (starboard) line excursion is calculated at scenarios B (scenario A) based on the numerical excursion-tension for the port (starboard) mooring line and its corresponding average of measured mooring tensions; and the bow line excursions are calculated at both scenario A and scenario B based on the numerical excursion-tension for the bow mooring line and the corresponding averages of measured mooring tensions.

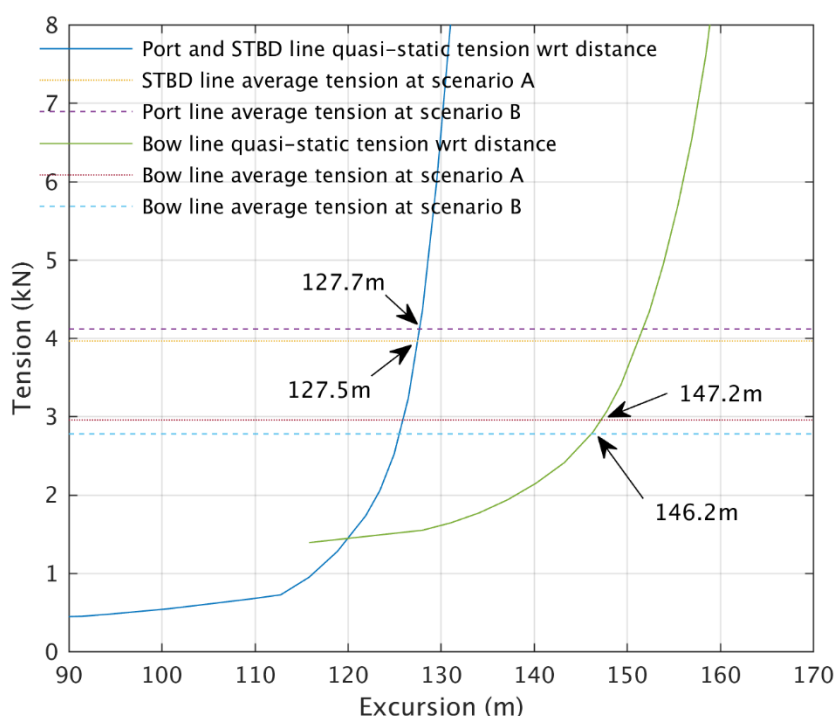


Figure 4-9. Calculation of horizontal distances from Ocean Sentinel to the bow, port and starboard anchors based on the numerical excursion-tension curves and average measured mooring tensions acting on the Ocean Sentinel at scenarios A and B

Based on the calculated horizontal distances for the bow, port and starboard anchors, the adjusted anchor positions can be obtained as illustrated in Figure 4-10. The adjusted positions of the bow, port and starboard anchors are 9.1 m, 4.6 m and 23.2 m away from their recorded positions, respectively. Comparing to the anticipated maximum difference between the measured and actual anchor positions (11 m), the difference between the adjusted and recorded positions for the starboard anchor exceed the anticipated difference significantly, which may be caused by errors in measuring or recording the GPS position of the starboard anchor. Note that the finding of this excessive difference for the starboard anchor demonstrates the importance of the anchor position adjustment method, which was also used in Harnois et al. (2012) to estimate anchor positions.

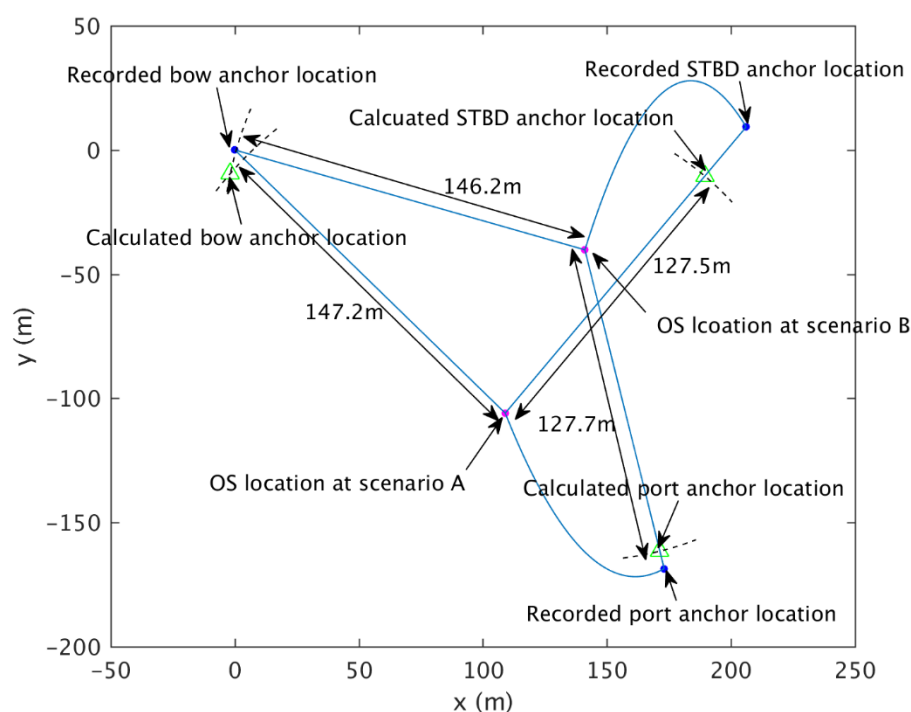


Figure 4-10. Estimation of anchor positions using the calculated horizontal distances from the Ocean Sentinel to the bow, port and starboard anchors

After adjusting the anchor positions, the new experimental excursion-tension curve compares quite well with the numerical excursion-tension curve for individual bow, port and starboard mooring lines (demonstrated in Figure 4-11). The new experimental curves for the port and starboard mooring lines move toward the left of the original experimental curves, making them closer to the numerical curves. In addition, the bifurcation of the original experimental curve for the bow mooring line (see Figure 4-8) vanishes after the bow anchor position is adjusted.

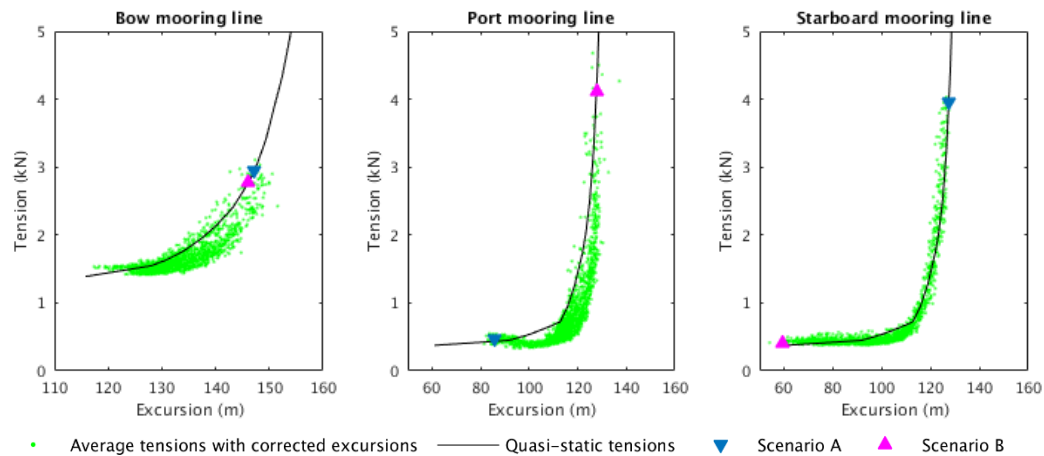


Figure 4-11. Comparison between the numerical excursion-tension curve and the experimental excursion-tension curve with adjusted anchor position for individual bow, port and starboard mooring lines

4.4.3 Results

The responses of the OS and its mooring system are simulated at adjusted anchor positions at field test scenarios of A, B, C and D. Instead of 20 minute time intervals in the field test, the simulation time for each scenario is increased to 3 hours and 40 minutes so that the low frequency responses of the OS and its mooring system can be

captured (Chen et al., 2001). The last 3 hours of each simulation is considered to be a steady state period, which follows 20 minutes of ramping period and 20 minutes of transient period. All the following numerical results are processed from the steady state period.

4.4.3.1 Accuracy in predicting mooring tensions on the OS

4.4.3.1.1 Mean, standard deviation and maximum of mooring tensions

To study the accuracy of the fully coupled method, the predicted means, standard deviations and maximums of mooring tensions under the four typical scenarios (A-D) are compared to those of field measurements respectively (see Table 4-4). Note that the port mooring line at scenario A and the starboard mooring line at scenario B, C and D were in slack conditions, so their corresponding mooring tensions are not listed in the table.

Table 4-4. Comparison of measured and predicted mooring tensions acting on the Ocean Sentinel at four scenarios (A, B, C and D)

	Mooring lines	L/H ratio	Tension (N)	Field data	Numerical predictions	Relative difference
Scenario A	Bow	1.8	mean	2,953	3,615	22%
			STD	770	1,058	37%
			MAX	7378	9318	26%
	Starboard	1.2	mean	3,963	4,307	9%
			STD	1,050	695	-34%
			MAX	7,407	7,486	1%
Scenario B	Bow	1.8	mean	2,777	3,165	14%
			STD	814	754	-7%
			MAX	6,043	7,847	30%
	Port	1.2	mean	4,115	4,102	0%
			STD	1,693	1,870	10%
			MAX	11,239	11,757	5%
Scenario C	Bow	1.8	mean	3,127	3,716	19%
			STD	1,233	1,101	-11%
			MAX	9,346	10,326	10%
	Port	1.2	mean	4,709	5,032	7%
			STD	2,535	1,821	-28%
			MAX	15,487	12,981	-16%
Scenario D	Bow	1.8	mean	3,326	3,865	16%
			STD	1,373	1,195	-13%
			MAX	11,550	14,006	21%
	Port	1.2	mean	5,012	5,195	4%
			STD	2,691	2,438	-9%
			MAX	16,308	18,139	11%

* STD and MAX are the abbreviations of standard deviation and maximum, respectively.

The relative difference in Table 4-4 is defined as

$$d_{\text{rel}} = (T_{\text{num}} - T_{\text{exp}})/T_{\text{exp}} \quad \text{Eq. (4.8)}$$

where T_{num} is the predicted mooring tension and T_{exp} is the measured mooring tension.

The relative differences between the predicted and measured mean mooring tensions are in the range of 0% to 22%. These differences are thought to be mainly caused by the discrepancies in estimating wind and water drag forces and second order wave drift force. The relative differences between the predicted and measured standard deviations and maximums of dynamic mooring tensions are in the range of -34% to 37% and -16% to 30%, respectively. These differences are thought to be mainly caused by the assumption of linear relationship between the first order wave forces (hydrostatic force, Froude-Krylov force, diffraction force and radiation force) and wave height, the simplified modeling of the surface buoys (modeled as 6 DOF lumped structures) and the approximation of viscous damping on the OS mooring system.

The L/H ratios of the mooring lines are shown to affect the accuracy in predicting mooring tensions. Comparing scenario B, C and D, the relative differences between the predicted and measured standard deviations for the bow mooring line (range from -13% to -7%), whose L/H ratio is 1.8, are smaller than the relative differences for the port line (range from -28% to 10%), whose L/H ratio is 1.2. This is because, at large OS excursions, the port line tension is more sensitive to the dynamic motion of the OS than the bow line tension (demonstrated in Figure 4-11).

4.4.3.1.2 Factors affecting the accuracies of mooring tension predictions for the OS mooring system and other mooring systems in the literature

The accuracies of the fully coupled method in predicting mooring tensions for applications of this study and other literature (Harnois et al., 2015; Ormberg et al., 1997; Ran, 2000; Tahar et al., 2006) are compared in Table 4-5. Note that S1, S2 and S3 are

the abbreviations of scenario 1, scenario 2 and scenario 3 respectively. S1, S2 and S3 of the OS mooring system correspond to the scenarios of A, B and C respectively. Scenario D is not included in the comparison because of the possible anchor movement during that period. Line1, line2 and line3 of the OS mooring system corresponds to bow, port and starboard lines respectively.

Table 4-5. Accuracy of the fully coupled method in predicting mooring line tensions

Moored structure	Mooring line type	Water depth (full scale, unit m)	Experiment	Environmental loads	Environmental conditions	Mooring lines	L/H ratio	Relative difference	
								Mean	STD
turret moored tank (Ormberg et al., 1997)	catenary	330	tank test S1	irregular waves and wind	Extreme sea conditions	line 1 (windward line)	4.4	13%	7%
			tank test S2	irregular waves, wind and current	Extreme sea conditions	line 1 (windward line)	4.4	11%	18%
truss spar (Ran, 2000)	taut	988	tank test S1	regular waves	Extreme sea conditions	line 1 (downwave line)	2.0	-2%	535%
						line 2 (upwave line)	2.0	5%	243%
			tank test S2	irregular waves, wind and current	Extreme sea conditions	line 1 (downwave line)	2.0	-1%	227%
						line 2 (upwave line)	2.0	6%	311%
truss spar (Tahar et al., 2006)	taut	1654	field test S1	irregular waves, wind and current	Extreme sea conditions	line 1 (least loaded line)	1.4	4%	166%
						line 2 (most loaded line)	1.4	16%	189%
buoy (Harnois et al., 2015)	catenary	30	tank test S1	irregular waves	Operational sea conditions	line 1	1.7	1%	-28%
						line 2	1.7	1%	-26%
						line 3	1.7	-1%	-29%
OS	catenary	47	field test S1	irregular waves, wind and current	Extreme sea conditions	line 1	1.8	22%	37%
						line 3	1.2	9%	-34%
			field test S2	irregular waves, wind and current	Extreme sea conditions	line 1	1.8	14%	-7%
						line 2	1.2	0%	10%
			field test S3	irregular waves, wind and current	Extreme sea conditions	line 1	1.8	19%	-11%
						line 2	1.2	7%	-28%

The relative differences of the studies above are affected significantly by the types of mooring systems (taut and catenary moorings). While the relative differences of mean mooring tensions for the taut moorings (-2%~16%) are close to those for the catenary moorings (-1%~22%), the relative differences of standard deviations for the taut moorings (166%~535%) are much larger than those for the catenary moorings (-34%~37%). This may be because mooring stiffness of the taut moorings were stronger than stiffness of the catenary moorings.

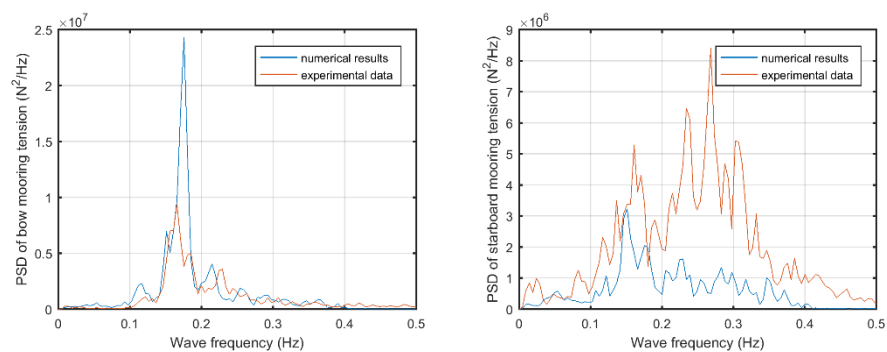
The relative differences for the catenary moorings are affected moderately by the water depths (shallow and deep water depths). While the relative differences of mean mooring tensions for the catenary moorings of 30 m and 47 m water depths (-1%~22%) are close to those for the catenary mooring of 330 m water depth (11%~13 %), the relative differences of standard deviations for the catenary moorings of 30 m and 47 m water depths (-34%~37%) are large than those for the catenary mooring of 330 m water depth (7%~18%). This may be because large portions of the mooring lines deployed in shallow water (water depth less than 70 m (API, 2007)) were affected by waves and current, while only the top portions of the mooring lines deployed in deep water (water depth larger than 150 m (API, 2007)) were affected by waves and current.

In Table 4-5, the mooring systems of the OS and the buoy studied in Harnois et al. (2015) are considered to be typical WEC mooring systems because of the following: (1) The dimensions of both the OS and the buoy are close to the dimensions of typical WECs, which are relatively small compared to typical ocean wind generated wave lengths (60 m to 150 m); and (2) The water depths of both the OS and the buoy mooring systems were relatively small.

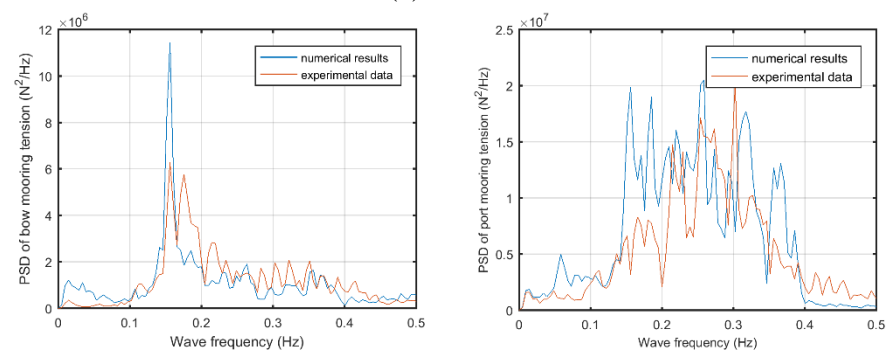
The relative differences for the above WEC moorings are affected by the experimental test conditions (field test under ocean conditions or tank test under waves only). While the relative differences of standard deviations for the OS mooring (-34%~37%) are close to those for the buoy mooring (-29%~-26%), the relative differences of mean tensions for the OS mooring (0%~22%) are much larger than those for the buoy mooring (-1%~1%). This may be because the components of drift force on the OS (generated from waves, current and wind in the field test) was different from the component of drift force on the buoy (generated from waves only in the tank test).

4.4.3.1.3 Power spectral densities (PSDs) of mooring tensions

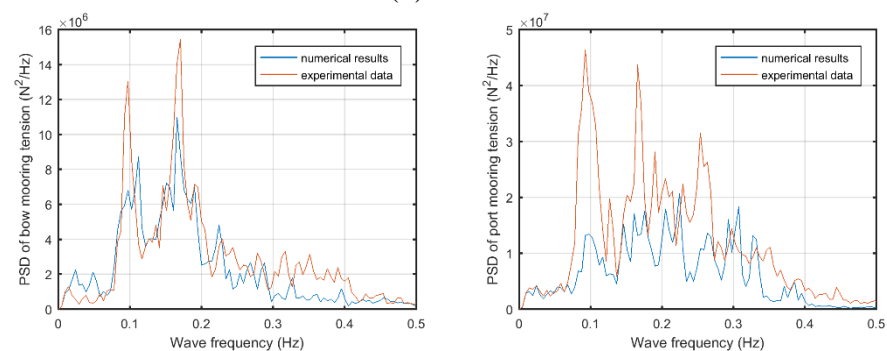
The power spectral densities (PSDs) of the predicted and measured mooring tensions on the OS are compared in Figure 4-12.



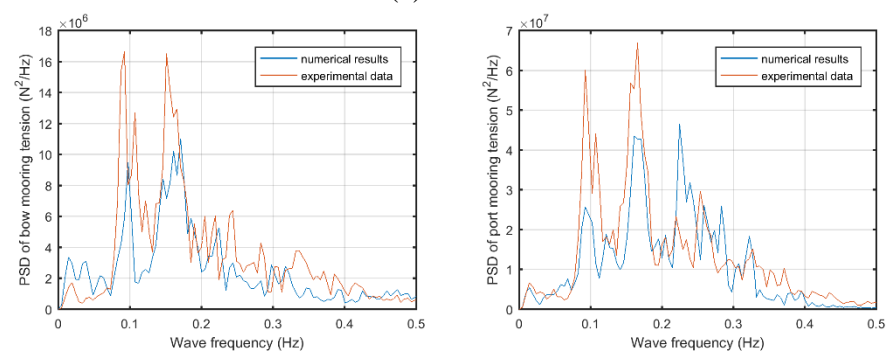
(a) Scenario A



(b) Scenario B



(c) Scenario C



(d) Scenario D

Figure 4-12. Comparison of power spectral densities between the predicted and measured mooring tensions

The shapes of the PSDs of the predicted mooring tensions are close to those of the corresponding measured mooring tensions. The resonant frequencies with the peak PSD values are generally the same for the predicted and measured mooring tensions.

The magnitudes of the PSDs of the predicted mooring tensions are generally smaller than those of the corresponding measured mooring tensions. This is because additional linear damping is added to the surface buoy motions in the horizontal directions. Without the additional damping, the predicted mooring tensions would have significant super-harmonic response. For example, as shown in Figure 4-13, the peak frequencies of the measured port line mooring tension with the two largest PSD values at scenario D are 0.09 Hz and 0.17 Hz, while the peak frequency of the predicted port line mooring tension with the largest PSD value is 0.28 Hz when no additional damping is added.

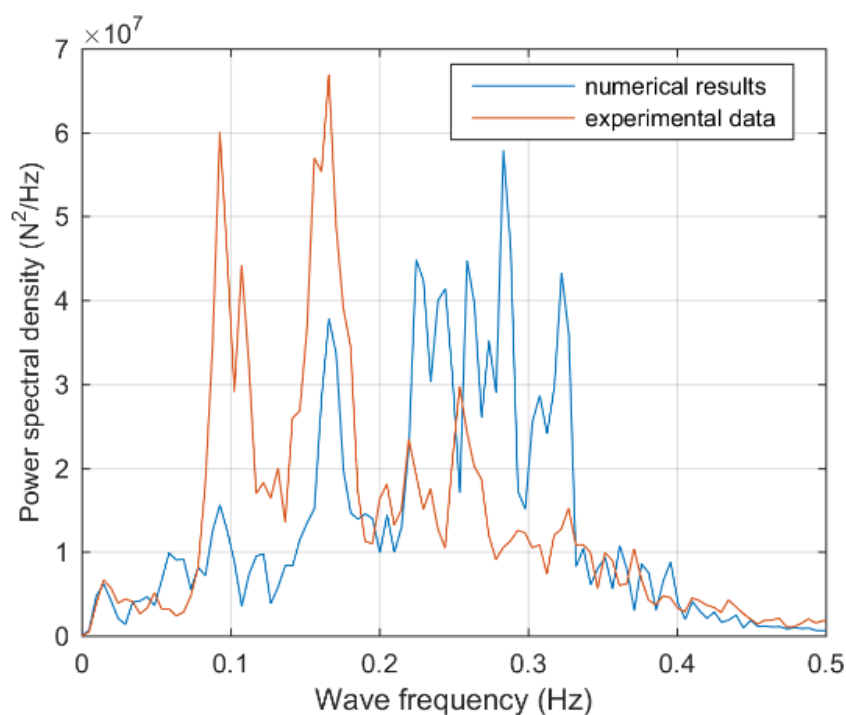


Figure 4-13. Super-harmonic response of the predicted mooring tensions of the port line at Scenario D, when there is no additional linear damping in the horizontal directions of the port surface buoy

The super-harmonic response of the numerical port line mooring tension in Figure 4-13 is found to be correlated to the super-harmonic response of the horizontal motion of the port surface buoy, which motion is governed by the Morison equation. Therefore, the accuracies of the predicted mooring tensions on the OS are not only affected by the modeling of the OS (large volume structure), which is based on linear wave force assumption, but also affected by the modeling of the surface buoy (6 DOF lumped buoy), which is based on the Morison equation.

4.4.3.2 Accuracy in predicting OS positions

The measured and predicted OS positions for scenarios A, B, C and D are compared in Figure 4-14. The measured OS positions b and c are inside the predicted boundaries of the OS positions at scenarios B and C, respectively. The measured OS position d is about 6 m away from the predicted boundary of the OS positions at scenario D. Considering that all the anchors are fixed in each numerical simulation, the above comparisons indicate that the anchors were probably not moved at scenario B and C, and one or more anchors were probably moved at scenario D. These findings of anchor movements are consistent with the previous assumptions in Section 4.4.2.2.

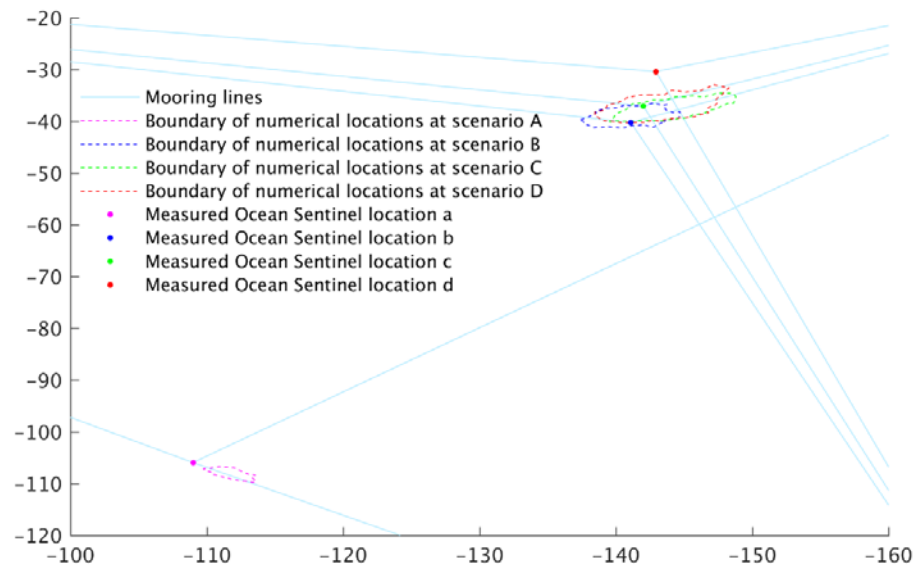


Figure 4-14. Comparison of measured and numerical positions of Ocean Sentinel at four scenarios (a, b, c and d)

The measured position a is also outside its predicted boundary at scenario A. However, this is not related to anchor movement, which will be explained later through comparing the dynamic anchor pulling forces to anchor holding capacity in Section 4.5. The discrepancy is mainly caused by the significant uncertainty of the starboard anchor position. As the difference between the recorded and adjusted positions for the starboard anchor (23.2 m) was much greater than the differences for the bow and port anchors (9.1 m, 4.6 m, demonstrated in Figure 4-10), the uncertainty of the actual starboard anchor position is expected to be much larger than the uncertainties of the actual bow and port anchors. Since the OS position was mainly controlled by the bow and starboard anchor positions at scenario A, while the OS position was mainly controlled by the bow and port anchor positions at scenario B, the numerical prediction

of the OS position at scenario A is expected to be less accurate than the numerical prediction of the OS position at scenario B.

4.5 Mechanics of Anchor Movement

The movability of mooring anchor can be indicated by the anchor reserved capacity, which is defined as the static anchor resistance minus the effective force:

$$C_r = c(W_a - F_{bv}) - F_{bh} = \overbrace{c \cdot W_a}^{F_r} - \overbrace{(c \cdot F_{bv} + F_{bh})}^{F_e} \quad \text{Eq. (4.9)}$$

$$F_r = c \cdot W_a \quad \text{Eq. (4.10)}$$

$$F_e = c \cdot F_{bv} + F_{bh} \quad \text{Eq. (4.11)}$$

where C_r is the anchor reserved capacity; c is the friction coefficient between anchor and seafloor (e.g. 0.74 for concrete anchor at Oolitic sand (SST, 2009)); W_a is the submerged weight of anchor (22.28 kN); F_{bv} and F_{bh} are the vertical and horizontal pulling forces on the anchor; F_r is defined as the static anchor resistance; and F_e is defined as the effective force.

If the anchor reserved capacity is positive, which means the effective force is smaller than the static anchor resistance, the anchor does not move; if the anchor reserved capacity is negative, which means the effective force is larger than the static anchor resistance, anchor movement would initiate. Therefore, the anchor movability can also be indicated by the ratio (r_a) of effective force to static anchor resistance, which is shown in the follow equations:

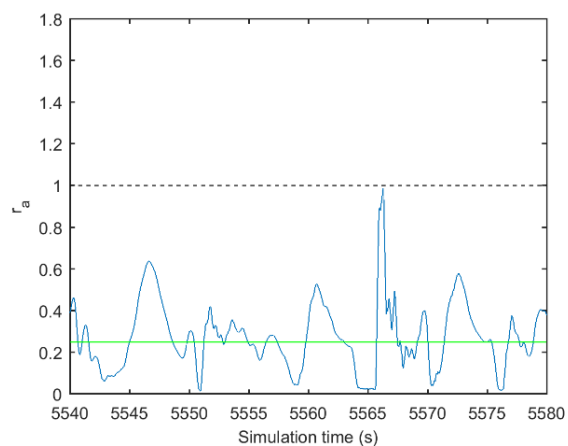
$$r_a = \frac{F_e}{F_r} = \frac{c \cdot F_{bv} + F_{bh}}{c \cdot W_a} \begin{cases} \leq 1 & \text{no anchor movement} \\ > 1 & \text{anchor movement} \end{cases} \quad \text{Eq. (4.12)}$$

As mentioned earlier, the OS drifted significantly in scenario D. To study the anchor movement during this period, the instantaneous values of r_a for the bow, port and starboard anchors are calculated using the numerical model.

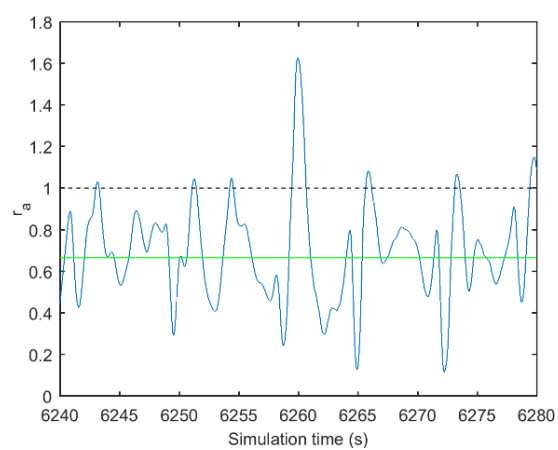
Since the anchor movement is related to both the magnitude and duration of the effective force on the anchor, the mean and maximum values of r_a for the individual bow, port and starboard anchors are listed in Table 4-6. In addition, the instantaneous r_a of each mooring anchor is plotted in Figure 4-15 for the period including the time of maximum r_a . The solid blue line indicates the instantaneous r_a , and the solid green line indicates the mean value of r_a .

Table 4-6. Statistics of the ratio (r_a) of instantaneous effective force to static resistance

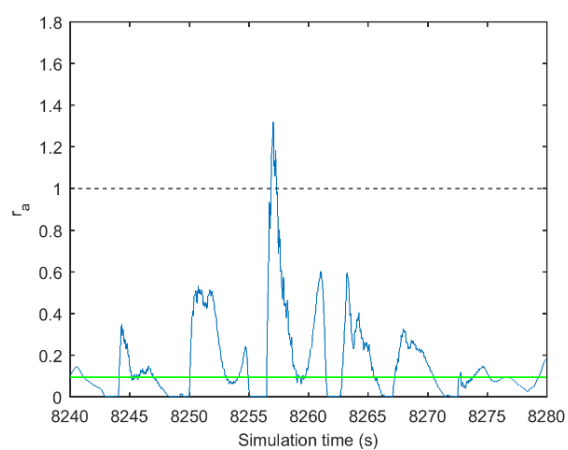
r_a		Mean	Maximum
Scenario D	Bow anchor	0.25	0.98
	Port anchor	0.67	1.63
	Starboard anchor	0.09	1.32



(a) Bow anchor



(b) Port anchor



(c) Starboard anchor

Figure 4-15. Time history of the ratio r_a for the bow, port and starboard anchors

Based on both Table 4-6 and Figure 4-15, the movability of each anchor is discussed as follows: (1) the port anchor was likely dragged during the significant OS drift because the maximum value of r_a for port anchor (1.67) is significantly larger than one, and r_a frequently reaches to values larger than one within the duration of 40s in the figure; (2) the starboard anchor was likely dragged slightly because r_a increases rapidly from almost zero to its maximum value (1.32) and drops rapidly after that, this phenomenon is typically caused by a short-duration snap load of the mooring chain, while r_a is smaller than one for the rest of the 40s interval; (3) the bow anchor was likely not dragged because the maximum value of r_a (0.98) is smaller than one, and is also caused by a snap load of the mooring chain.

Dynamic analysis of the anchor movement is shown to be important, because the instantaneous value of r_a for the individual bow, port and starboard mooring anchor oscillates in a relatively large amplitude compared to the mean value of r_a .

As defined in Equation 4.12, the value of r_a is also affected by the friction coefficient c , which ranges from 0.20 to 0.74 depending on sand type, anchor material and surface smoothness (Taylor, 1982). Figure 4-16 plots the maximum values of r_a corresponding to some typically friction coefficients, for the bow, port and starboard anchors at scenario D. Based on the figure, the followings are found: (1) The maximum value of r_a correlates closely to the friction coefficient, which means that the friction coefficient needs to be judiciously selected for each numerical study based on the sea floor type, anchor material and surface smoothness as shown in Taylor (1982); and (2) The friction coefficient of the anchors in this study (rough concrete anchors deployed at Oolitic sand) is 0.74. This value is generally larger than the anchor friction coefficients of other

sea floor types and anchor materials. Therefore, to prevent anchor movement in future anchor design of the OS mooring system, the way to reduce the value of r_a should be increasing the submerged weight of anchor rather than increasing the anchor friction coefficient.

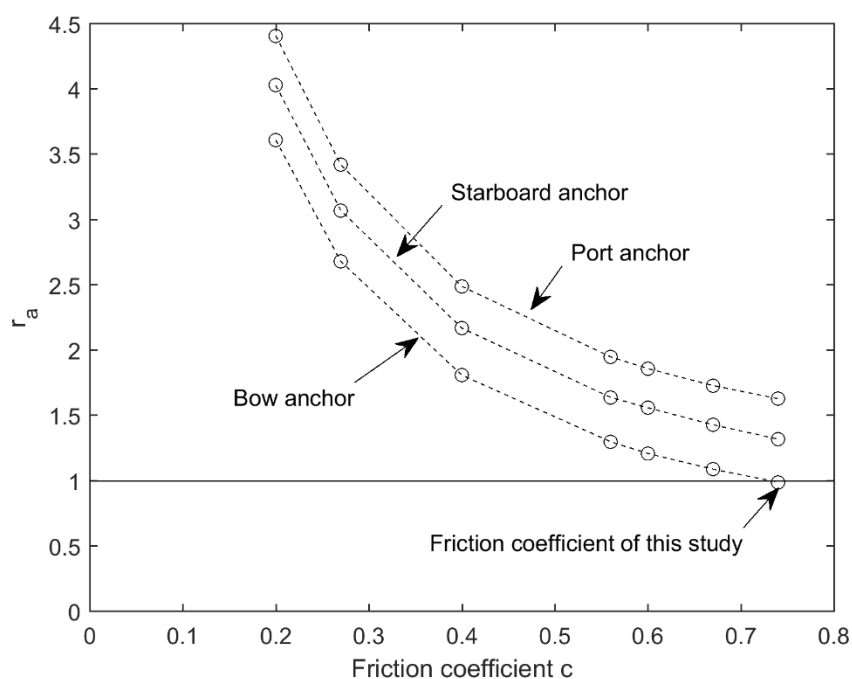


Figure 4-16. Sensitivity study of r_a with respect to friction coefficient c for the bow, port and starboard anchors

4.6 Fatigue Damage Estimation

After the fully coupled method is validated, mooring tensions of the OS can be predicted through dynamic simulations for a series of statistical environmental conditions of the whole year at the NETS. Then the corresponding fatigue damages of the OS mooring system can be estimated based the mooring tension predictions.

4.6.1 Fatigue properties and accumulation rule

To estimate the fatigue damage, the power law model of the material S-N curve

$$N(s) = K^{-1}s^{-\beta} \quad \text{Eq. (4.13)}$$

and the Palmgren-Miner linear damage accumulation rule are used:

$$D(t) = \sum_{t_k \leq t} \frac{1}{N(s_k)} = K \sum_{t_k \leq t} s_k^\beta \quad \text{Eq. (4.14)}$$

where $N(s)$ is the number of loading cycles until failure; s is the ratio of tension range to average strength of each mooring line; K and β are the material dependent parameters (according to DNV (2013)), $K = 3.861$, $\beta = 13.46$ for the polyester rope); $D(t)$ is the total damage at time t ; s_k is the value of s of the k^{th} circle; and t_k is the time of the k^{th} circle.

4.6.2 Specification of statistical waves, wind and current conditions

The simulated whole year statistical environmental conditions at the NETS including wind, waves and current conditions are listed in Table 4-7. The statistical wind and waves conditions, based on the historical wind and waves data of the NDBC buoy 46050 located 30 km west of the NETS, were provided by ABS (2013). The current profile is based on the measured current speed along water depth during the field test: the current speed changes linearly with water depth from 0.6 m/s at the sea surface to 0 m/s at the water depth of 30m; and the current speed below the water depth of 30 m is 0 m/s. The directions of the wind, waves and current are collinear.

Table 4-7. Summary of specified statistical environmental conditions at the NETS
(whole year)

Bin of fatigue design conditions	Wind speed	Significant Wave height	Peak period	Surface current speed	Directions
#	(m/s)	(m/s)	(s)	(m/s)	(degrees)
1	4.93	2.10	10.74	0.6	0,45,90,...,315
2	8.87	2.76	11.32	0.6	0,45,90,...,315
3	12.80	3.96	12.20	0.6	0,45,90,...,315
4	16.71	5.68	13.09	0.6	0,45,225,315
5	20.59	7.93	13.57	0.6	0,315

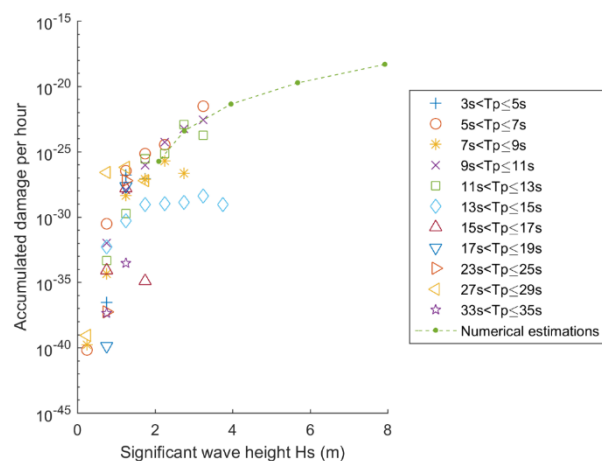
In each bin of the environmental conditions listed in Table 4-7, the magnitudes of the wind, waves and current speeds are constant, while the direction changes from 0° to 315° with a 45° spacing. Each direction corresponds to one environmental condition of the bin and is simulated for 30 minutes. The probabilities of occurrence for the directions in each bin were provided by ABS (2013) and are listed in Table 4-8. Note that the direction definition in ABS (2013) is different from the direction definition in this study.

Table 4-8. Probabilities of occurrence for specified statistical environmental conditions

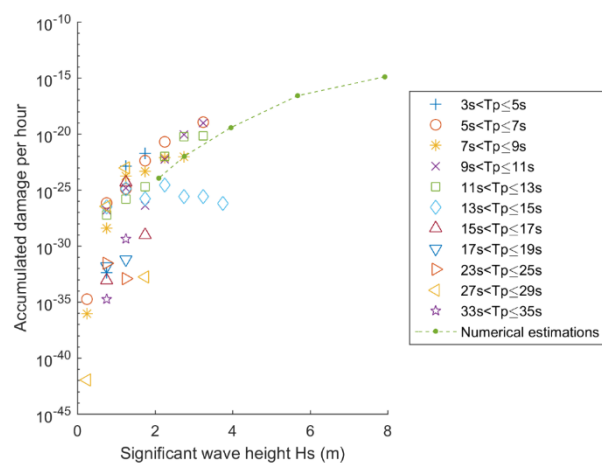
[illegible]

4.6.3 Predicted fatigue damages for polyester lines

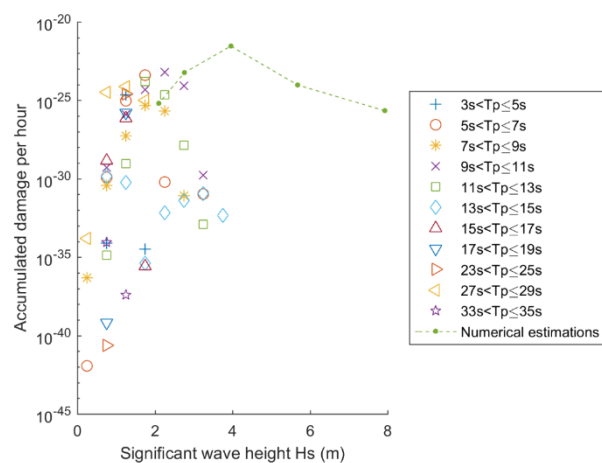
Using the MATLAB toolbox WAFO (Brodtkorb et al., 2000), the rainflow cycles of both the simulated and measured mooring tensions on the Ocean Sentinel are extracted with a threshold of 4.45 N (1 lbf.). Then the fatigue damage per hour of the individual mooring lines are estimated for both the statistical whole year environmental conditions and the measured environmental conditions during the field test (shown in Figure 4-17). The ways to calculate the fatigue damages for the two sets of environmental conditions are summarized as follows: (1) The fatigue damage for each bin of statistical environmental conditions (listed in Table 4-7) is calculated as a summation of the fatigue damages of all directions in the bin multiplied by their corresponding probability of occurrences. (For the convenience of comparing the fatigue damages between different bins, the total probability of occurrence for each bin is scaled up to 100%.); and (2) The fatigue damage for each bin of measured environmental conditions (grouped by both wave height and peak wave period) is calculated as the average of the fatigue damages of the measured environmental conditions within the bin.



(a) Bow polyester line



(b) Port polyester line



(c) Starboard polyester line

Figure 4-17. Fatigue damages per hour of field measurements and numerical predictions

For the bins of the whole year environmental conditions, the significant wave heights of which are 2.10, 2.76 and 3.96 m, the corresponding fatigue damage predictions are close to the fatigue damages before the significant OS drift (the maximum measured significant wave height during this period is 4 m). For the bins with significant wave heights of 5.68 and 7.93 m, the corresponding fatigue damage predictions provide estimations for the wave conditions that are stronger than the measured wave conditions.

The predicted fatigue damage for individual mooring lines generally increases as the significant wave height increases. However, for the starboard mooring line, the predicted fatigue damages of the significant wave height $H_s = 5.68$ m and $H_s = 7.93$ m are smaller than that of the significant wave height $H_s = 3.96$ m. This is because the environmental directions associated with $H_s = 5.68$ m and $H_s = 7.93$ are generally toward the north, under such conditions the starboard mooring line was in slack condition.

4.7 Extreme Mooring Tension Estimation

4.7.1 Design tension

In BV (2015), the design tension of a mooring line under a specified set of extreme environmental conditions is calculated as follows:

$$T_D = T_M + a \cdot T_S \quad \text{Eq. (4.15)}$$

where T_D is the design tension; T_M is the mean of the maximum tensions of n numerical simulations with random seed in wave generation; T_S is the standard deviation of the

maximum tensions; and a is a factor depending on the method of numerical analysis and number of simulations (listed in Table 4-9).

Table 4-9. Values of factor a with respect to the number of simulations

Method of numerical analysis	Number of simulations			
	n=5	n=10	n=20	n>30
Dynamic	0.6	0.3	0.1	0

4.7.2 Specification of extreme waves, wind and current conditions

In mooring design guidelines, the return period of extreme environmental conditions is at least 10 years for mobile floating units in the vicinity of other structures (API, 1997; BV, 2015). If the design return period is 100 years, combining all independent extremes (wave, wind and current) at the same return period is normally conservative. In such case reduction factors can be applied to individual independent extremes of 100-year return period (API, 2007); or a 100-year return period is applied to each candidate (wave, wind or current) in turn and fairly realistic, unfavorable levels are applied to other effects (DNV, 2013); or both the reduction factor and multiple levels of return period methods can be used together (BV, 2015).

To establish the maximum design (extreme) environmental conditions at the NETS, we first extract the monthly maxima for significant wave height, wind speed and current speed from their historical data. Then the monthly maximum values are modeled as independent observations from the generalized extreme value (GEV) distribution (Coles, 2001):

$$G(z) = \exp \left\{ - \left[1 + \xi \left(\frac{z - \mu}{\sigma} \right) \right]^{-1/\xi} \right\} \quad \text{Eq. (4.16)}$$

where z is the value of observation; μ is the position parameter; σ is a scale parameter; and ξ is a shape parameter.

Under the assumption that z_1, \dots, z_m are independent variables with GEV distribution, the log-likelihood for the GEV parameters is

$$l(\mu, \sigma, \xi) = -m \cdot \log \sigma - \left(1 + \frac{1}{\xi}\right) \sum_{i=1}^m \log \left[1 + \xi \frac{z_i - \mu}{\sigma}\right] - \sum_{i=1}^m \left[1 + \xi \frac{z_i - \mu}{\sigma}\right]^{-\frac{1}{\xi}}, \text{ for } \xi \neq 0 \quad \text{Eq. (4.17)}$$

$$l(\mu, \sigma) = -m \cdot \log \sigma - \sum_{i=1}^m \left(\frac{z_i - \mu}{\sigma}\right) - \sum_{i=1}^m \exp \left[-\left(\frac{z_i - \mu}{\sigma}\right)\right]^{-\frac{1}{\xi}}, \text{ for } \xi = 0 \quad \text{Eq. (4.18)}$$

The parameters $\hat{\mu}$, $\hat{\sigma}$ and $\hat{\xi}$ are estimated numerically through the maximization of the likelihood Equations 4.15 and 4.16. Using these parameters, the maximum likelihood estimate of z_p , with $1/p$ return level, is obtained as

$$\hat{z}_p = \begin{cases} \hat{\mu} - \frac{\hat{\sigma}}{\hat{\xi}} \left[1 - y_p^{-\hat{\xi}}\right], & \text{for } \xi \neq 0 \\ \hat{\mu} - \hat{\sigma} \log(y_p), & \text{for } \xi = 0 \end{cases} \quad \text{Eq. (4.19)}$$

where $y_p = -\log(1 - p)$.

Based on the historical data of waves and wind recorded hourly by the NDBC buoy 46050 from 1991 to 2015, the monthly extreme values of significant wave height and wind speed with 10 and 100 years of return level are estimated for the NETS and plotted in Figure 4-18 and Figure 4-19, respectively. Both the significant wave height and the wind speed vary significantly among different months of a year. For example, the 10 year return levels for the significant wave height and the wind speed are 3.5 m and 13.3 m/s, respectively, in July, while they are 10.7 m and 22.5 m/s, respectively, in December. These monthly extreme environmental conditions are useful for designing

a new mooring system of the Ocean Sentinel if it is going to be deployed in certain months of a year.

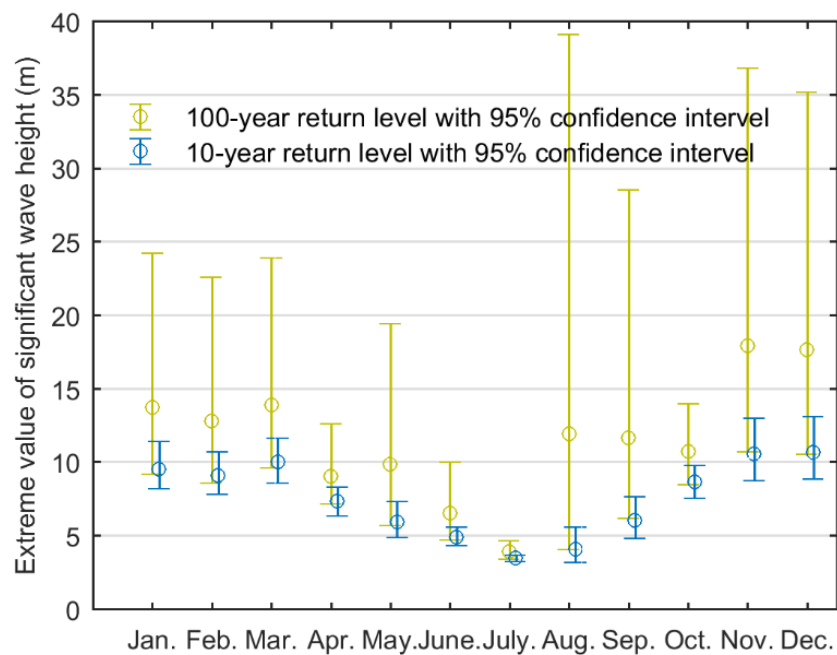


Figure 4-18. Extreme values of significant wave height with return periods of 10 and 100 years at the position of NDBD buoy 46050 (located 30 km west of the NETS)

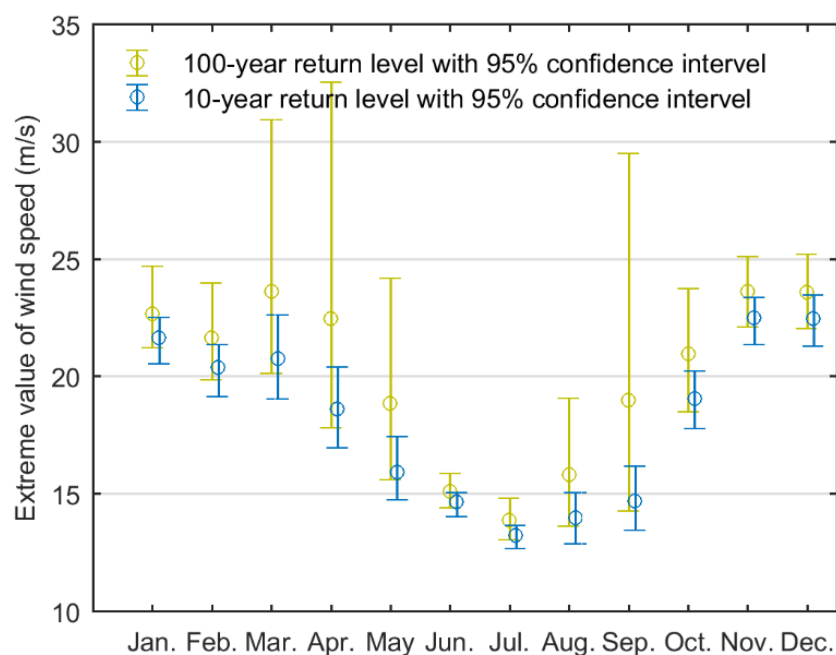


Figure 4-19. Extreme values of average wind speed with return periods of 10 and 100 years at NDBD buoy 46050 (located 30 km west of the NETS)

The maximum of the monthly 100-year significant wave heights estimated in this study is 17.9 m (corresponding to the month of November). It is in good agreement with the 100-year significant wave height of 17.5m given by Dallman and Neary (2014). The latter value is the largest significant wave height on the 100-year contour (significant wave height with respect to wave period) estimated based on the inverse first order reliability method with the wave data from the same NDBC buoy 46050.

Note that some waves and wind conditions were not observed over certain time periods during the whole deployment of the NDBC buoy 46050, which phenomenon may be caused by the harsh environmental conditions in storms. In Serafin and Ruggiero (2014), larger values of extreme significant wave height were estimated after taking into account those missing observations.

Based on the historical data of current speed recorded by NH10 buoy from 1997 to 2004 (OSU, 2004), the monthly extreme values of current speed with 10 years of return level are estimated and plotted in Figure 4-20. Note that the 100-year current speeds are not presented, because the duration of measured current data (7 years) are relatively small.

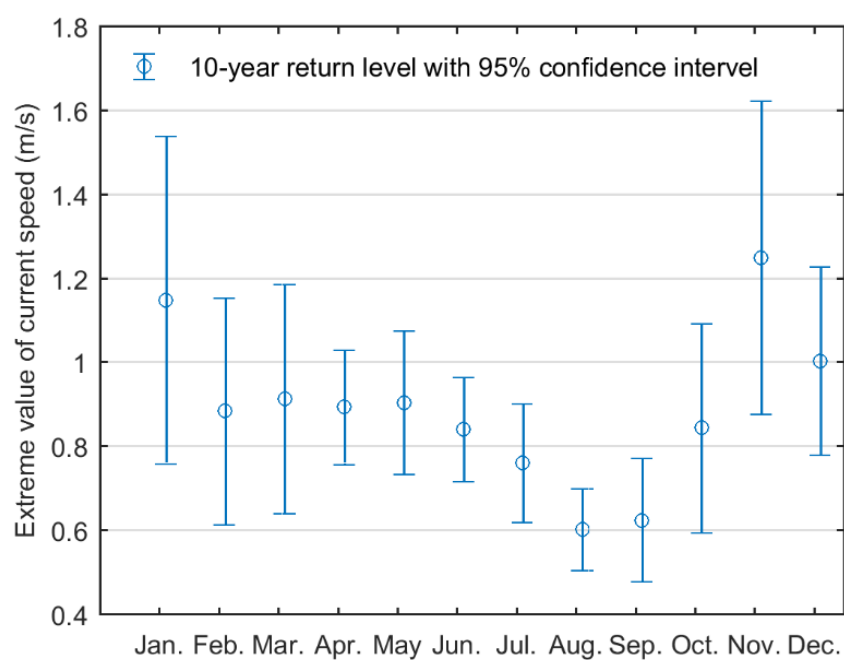


Figure 4-20. Extreme values of current speed with return period of 10 years at the position of NH10 (located 13 km east of the NETS)

The specified extreme environmental conditions of this study are as follows (listed in Table 4-10): the extreme significant wave height, wind and current speeds are specified to be their corresponding 10 year return levels for the period from July to September; and the directions of the wind, waves and current are collinear and range from 180° to 360° with a spacing of 30°. Note that the OS was deployed 3-5km west of the Oregon

coast, so the waves directions from 30° to 150° (generally propagating to the west) are not considered.

Table 4-10. Simulated extreme environmental conditions

Significant wave height (m)	Wave		Wind speed (m/s)	Current speed (m/s)	Collinear directions
	Peak period (s)	Spectrum			
6.1	13.2	JONSWAP	14.7	0.76	180°, 270°, ... 360°

4.7.3 Predicted extreme mooring tensions for polyester line and mooring chain

In predicting extreme mooring tensions of the OS, simulations are conducted in two steps. First, the dynamic responses of the OS mooring system under the specified extreme environmental conditions are simulated for 3 hours in each environmental direction (180°, 270°, ..., 360°). Second, in the direction with the maximum predicted mooring tensions, the simulations are conducted for a total of 10 times (each time the simulation is specified with a different random seed in wave generation). Based on the maximum tensions predicted by the simulations in step 2, the design tensions T_D of the polyester line and mooring chain are calculated and listed in Table 4-11. With a safety factor of 1.67 for the dynamic simulation using the fully coupled method (BV, 2015), the design strengths of the polyester line and mooring chain are calculated and compared to their strengths in the original design (see Table 4-11).

Table 4-11. Design tensions and strengths of the polyester line and mooring chain

	Design tension (kN)	Design strength (kN)	Strength in the original design (kN)
Polyester line	41.64	69.54	266.9
Mooring chain	44.47	74.27	258.0

4.8 Concluding Remarks and Future Work

In this study, the accuracies of a fully coupled method based numerical model in predicting dynamic mooring tensions and positions of wave energy converters were demonstrated in its application for the mooring system of a mobile ocean test berth, the Ocean Sentinel (OS) instrumentation buoy. The numerical model, which was validated by field test measurements, was shown to provide accurate predictions of the mooring tensions acting on the OS at four typical scenarios A-D with harsh waves, current and wind conditions. The relative differences between the predicted and measured mooring tensions are 0% ~ 22%, -34% ~ 37% and -16% ~ 30% for the mean, standard deviation and maximum of mooring tensions, respectively. The predicted and measured power spectral densities of mooring tensions are generally in good agreements, with additional damping added on the surface buoys to reduce its over-predicted super-harmonic response. In addition, the numerical model was also shown to generally provide accurate predictions of the OS positions for the scenarios of A, B and C, when the mooring anchors were likely not dragged.

Comparing studies of the OS mooring system and other mooring systems in the literature, the accuracy of the fully coupled method in prediction mooring tensions was found to be affected by the mooring type (catenary mooring or taut mooring), the water

depth (shallow water or deep water) and the experimental test conditions (field test under ocean conditions or tank test under waves only).

After the numerical model was validated, anchor movability, fatigue damage and extreme mooring tension of the OS mooring system were evaluated as follows:

- i. At scenario D, which corresponded to the significant OS drift, the port anchor was likely dragged significantly; the starboard anchor was likely dragged slightly; and the bow anchor was likely not dragged. The anchor movability of each anchor was investigated through studying the ratio r_a of instantaneous effective force to static anchor resistance predicted by the numerical model. The large-amplitude oscillation of the instantaneous value of r_a compared to its mean value demonstrates the importance of dynamics analysis in studying anchor movement. The close correlation between the value of r_a and friction coefficient shows that the friction coefficient needs to be judiciously selected for each numerical study based on the sea floor type, anchor material and surface smoothness.
- ii. Fatigue damages of the polyester lines can be estimated for environmental conditions from low sea state (with small range of mooring tension but large probability of occurrence) to high sea state (with large range of mooring tension but small probability of occurrence) through the numerical model. The predicted fatigue damages were shown to be in good agreements with the fatigue damages during the field test, when high sea state (significant wave height larger than 4 m) was not observed.

- iii. The extreme mooring tensions of the polyester line and mooring chain can be predicted through dynamic simulations under the estimated extreme waves, wind and current conditions at the NETS. After calculating the design strengths of the polyester line and mooring chain using the predicted extreme mooring tensions and design equation, the strengths of the polyester line and mooring chain in the field test were shown to be adequate.

The following two topics are suggested for future study:

- (1) Validation of the parameters in the mooring design equations in their applications for wave energy converters (WECs) through studying the reliability index of the mooring system based on the measured mooring tensions during the OS field test. The parameters used in this study were developed mainly for conventional floating structures in the oil industry and may not be optimal for WEC device design.
- (2) Influence of power take off (PTO) on the behaviors of a WEC mooring system, which is important as energy extraction by the PTO may affect the hydrodynamic responses of the WEC device significantly under a variety of environmental conditions. This can be examined using the numerical code employed in this study or open source codes such as WEC-Sim which has advanced PTO modeling capacity.

4.9 Acknowledgements

Financial support from the Department of Energy Grant No. DE-FG36-08GO18179-M001 is gratefully acknowledged.

4.10 References

- ABS. (2013). Design Guideline for Stationkeeping Systems of Floating Offshore Wind Turbines: American Bureau of Shipping.
- Amon, E., Brekken, T. K. A., & von Jouanne, A. (2011). A Power Analysis and Data Acquisition System for Ocean Wave Energy Device Testing. *Renewable Energy*, 36(7), 1922-1930. doi:10.1016/j.renene.2010.12.016
- API. (1997). API-RP-2SK Recommended Practice for Design and Analysis of Stationkeeping Systems for Floating Structures.
- API. (2007). API BULLETIN 2INT-MET Interim Guidance on Hurricane Conditions in the Gulf of Mexico.
- Baker, J. L. (2013). *Mooring Analysis of the Ocean Sentinel through Field Observation and Numerical Simulation*. (Master of Science), Oregon State University.
- Brodtkorb, P. A., Johannesson, P., Lindgren, G., Rychlik, I., Rydén, J., & Sjö, E. (2000). *WAF0-a Matlab Toolbox For Analysis of Random Waves and Loads*. Paper presented at the The Tenth International Offshore and Polar Engineering Conference, Seattle, USA, .
- BV. (2015). NR 493 DT R03 E Classification of Mooring Systems for Permanent and Mobile Offshore Units.
- Chen, X. H., Zhang, J., & Ma, W. (2001). On Dynamic Coupling Effects between a Spar and its Mooring Lines. *Ocean Engineering*, 28(7), 863-887. doi:10.1016/s0029-8018(00)00026-3
- Colby, C., Sodahl, N., Katla, E., & Okkenhaug, S. (2000). *Coupling Effects for a Deepwater Spar*. Paper presented at the Offshore Technology Conference.
- Coles, S. (2001). *An Introduction to Statistical Modeling of Extreme Values* (Vol. 208). London: Springer.
- Correa, F. N., Senra, S. F., Jacob, B. P., Masetti, I. Q., & Mourelle, M. M. (2002). *Towards the Integration of Analysis and Design of Mooring Systems and Risers: Part II - Studies on a DICAS System*. Paper presented at the ASME 2002 21st International Conference on Offshore Mechanics and Arctic Engineering.
- Dallman, A. R., & Neary, V. S. (2014). *Characterization of U.S. Wave Energy Converter (WEC) Test Sites: A Catalogue of Met-Ocean Data*. No. SAND2014-18206. Sandia National Laboratories (SNL-NM), Albuquerque, NM (United States)
- DNV. (2013). DNV-OS-E301 Position Mooring: DET NORSKE VERITAS.
- Garrett, D. L. (2005). Coupled Analysis of Floating Production Systems. *Ocean Engineering*, 32(7), 802-816. doi:10.1016/j.oceaneng.2004.10.010
- Garrett, D. L., Chappell, J. F., & Gordon, R. B. (2002). *Global Performance of Floating Production Systems*. Paper presented at the Offshore Technology Conference.

- Gobat, J. I., & Grosenbaugh, M. A. (2006). Time-domain Numerical Simulation of Ocean Cable Structures. *Ocean Engineering*, 33(10), 1373-1400. doi:10.1016/j.oceaneng.2005.07.012
- Harnois, V., Parish, D., & Johanning, L. (2012). *Physical Measurement of a Slow Drag of a Drag Embedment Anchor During Sea Trials*. Paper presented at the 4th International Conference on Ocean Energy, Dublin.
- Harnois, V., Weller, S. D., Johanning, L., Thies, P. R., Le Boulluec, M., Le Roux, D., Soule, V., & Ohana, J. (2015). Numerical Model Validation for Mooring Systems: Method and Application for Wave Energy Converters. *Renewable Energy*, 75, 869-887. doi:10.1016/j.renene.2014.10.063
- Heurtier, J. M., Le Buhan, P., Fontaine, E., Le Cunff, C., Biolley, F., & Berhault, C. (2001). *Coupled Dynamic Response of Moored FPSO with Risers*. Paper presented at the Proceedings of the ISOPE.
- Johanning, L., Smith, G. H., & Wolfram, J. (2007). Measurements of Static and Dynamic Mooring Line Damping and their Importance for Floating WEC Devices. *Ocean Engineering*, 34(14-15), 1918-1934. doi:10.1016/j.oceaneng.2007.04.002
- LCICG. (2012). *Technology Innovation Needs Assessment (TINA): Marine Energy Summary Report*.
- Ma, W., Lee, M.-Y., Zou, J., & Huang, E. W. (2000). *Deepwater Nonlinear Coupled Analysis Tool*. Paper presented at the Offshore Technology Conference.
- Orcina. (2009). *OrcaFlex Manual version 9.3a*.
- Ormberg, H., Fylling, I., Larsen, K., & Sodahl, N. (1997). *Coupled Analysis of Vessel Motions and Mooring and Riser System Dynamics*. Paper presented at the International Conference on Ocean, Offshore and Arctic Engineering.
- Ormberg, H., & Larsen, K. (1998). Coupled Analysis of Floater Motion and Mooring Dynamics for a Turret-moored Ship. *Applied Ocean Research*, 20(1-2), 55-67. doi:10.1016/s0141-1187(98)00012-1
- OSU, C. (2004). NH10 Buoy Current Data. College of Earth, Ocean, and Atmospheric Sciences (CEOAS), Oregon State University (OSU): <http://bragg.coas.oregonstate.edu/>.
- Ran, Z. (2000). *Coupled Dynamic Analysis of Floating Structures in Waves and Current*. (PhD), Texas A&M University.
- Serafin, K. A., & Ruggiero, P. (2014). Simulating Extreme Total Water Levels using a Time-dependent, Extreme Value Approach. *Journal of Geophysical Research-Oceans*, 119(9), 6305-6329. doi:10.1002/2014jc010093
- Sethuraman, L., & Venugopal, V. (2013). Hydrodynamic Response of a Stepped-spar Floating Wind Turbine: Numerical Modelling and Tank Testing. *Renewable Energy*, 52, 160-174. doi:10.1016/j.renene.2012.09.063
- SST. (2009). *Advanced Anchoring and Mooring Study*.
- Tahar, A., Halkyard, J., & Irani, M. (2006). *Comparison of Time and Frequency Domain Analysis With Full Scale Data for the Horn Mountain Spar During Hurricane Isidore*. Paper presented at the 25th International Conference on Offshore Mechanics and Arctic Engineering.

- Tahar, A., & Kim, M. H. (2008). Coupled-dynamic Analysis of Floating Structures with Polyester Mooring lines. *Ocean Engineering*, 35(17-18), 1676-1685. doi:10.1016/j.oceaneng.2008.09.004
- Taylor, R. J. (1982). Interaction of Anchors with Soil and Anchor Design. No. NCEL-TN-1627. NAVAL CIVIL ENGINEERING LAB PORT HUENEME CA.
- von Jouanne, A., Lettenmaier, T., Amon, E., Brekken, T., & Phillips, R. (2013). A Novel Ocean Sentinel Instrumentation Buoy for Wave Energy Testing. *Marine Technology Society Journal*, 47(1), 47-54.
- Weller, S., Hardwick, J., Johanning, L., Karimirad, M., Teillant, B., Raventos, A., . . . Sheng, W. (2014). *Deliverable 4.1: A Comprehensive Assessment of the Applicability of Available and Proposed Offshore Mooring and Foundation Technologies and Design Tools for Array Applications*.

CHAPTER 5

5. General Conclusions

This dissertation studied three topics for wave energy converters:

- A. The performances (strength and limitation) of one explicit finite element Navier-Stokes (NS) solver (ALE), one implicit finite element NS solver (ICFD) and one nonlinear potential flow solver (AQWA) in predicting the highly nonlinear hydrodynamic response of a FPA under large-amplitude waves;
- B. The global characteristics and survivability characteristics of the multi-catenary spread mooring system of the Ocean Sentinel (OS) during the 2013 OS field test, and procedure of designing a mooring system with adequate anchor resistance; and
- C. The accuracy of the numerical model based on the fully coupled method in predicting mooring tensions and OS positions of a field test under harsh ocean environments, and the applications of the numerical model in evaluating the anchor movability, fatigue damage and extreme mooring tension of the OS mooring system.

The main findings of these topics are provided below.

A. Concluding remarks on the performances of one explicit finite element NS solver (ALE), one implicit finite element NS solver (ICFD) and one nonlinear potential flow solver (AQWA)

- The predicted response amplitudes of the FPA using the three solvers are found to compare well with the experimental data for wave periods from 8.8 s to 14.9 s. The accuracies of the three numerical solvers in the heave, surge and pitch directions can be summarized as follows:

(1) In the heave direction, the averaged relative differences between the numerical predictions and the experimental data for the ALE and ICFD NS solvers, which are 8.3% and 10.8% respectively, are close to the averaged relative difference for the nonlinear potential flow solver of 8.5%.

(2) In the surge direction, the averaged relative differences between the numerical predictions and the experimental data for the ALE and ICFD NS solvers are 16.1% and 24.0%, respectively. These values are smaller than the averaged relative difference for the nonlinear potential flow solver, which is 67.4%. The better accuracies of these two NS solvers are mainly due to their ability to calculate the fully nonlinear wave force, while only the individual wave force components are calculated in the nonlinear potential flow solver.

(3) In the pitch direction, the averaged relative difference between the numerical predictions and the experimental data for the ALE NS solver is 42.2%, which is close to the averaged relative difference for the nonlinear potential flow solver of 35.7%. For the ALE NS solver, an eddy-making damping term is added in the governing equations of the FPA motions to compensate the vortices induced damping that are underestimated in solving the NS equations. For the nonlinear potential flow solver, a corresponding eddy-making damping term is also added in the governing equations of the FPA motions to calculate the whole vortex-induced damping in the pitch direction that cannot be obtained by solving the potential flow equations.

- The computational cost for the implicit ICFD NS solver is approximated 1.6 times as large as the computational cost for the explicit ALE NS solver, which is a result of the larger number of elements and re-meshing process in the ICFD NS solver. The computational cost for the potential flow solver is much smaller than the computational costs for the two NS solvers.
- Through the quantitative analysis of the inviscid wave force components (the hydrostatic force, the Froude-Krylov force, the radiation force and the diffraction force), the viscous force, the mooring force and the total force in the time domain calculated by the nonlinear potential flow solver, it is found that for any wave period from 8.1 s to 17.6 s, the restoring force and the Froude-Krylov force are important for the highly nonlinear responses of the FPA in all the heave, surge and pitch directions. The viscous force is found to be important in the heave and pitch directions.
- Through comparing the nonlinear restoring and Froude-Krylov forces in the time domain to the linear restoring and Froude-Krylov forces in the frequency domain respectively, the nonlinearities of the restoring and Froude-Krylov forces are shown to be important for the motion responses of the FPA in the heave and pitch directions.
- Based on the performances of the three numerical solvers in this study, the following are suggested: a). the nonlinear potential flow solver can be used for preliminary studies of the highly nonlinear hydrodynamic responses of floating WECs under large-amplitude waves, with careful modeling of the viscous force; b). the two NS solvers, because of their high computational costs, should be employed

to study the highly nonlinear hydrodynamic responses for extreme scenarios, keeping in mind the high computational effort required. For further study, the hydro-elastic responses of a floating WEC under large-amplitude waves can be analyzed using the two NS solvers.

B. Concluding remarks on the global characteristics and survivability characteristics of the Ocean Sentinel (OS) mooring system, and the procedure of designing a mooring system with adequate anchor resistance

- The global characteristics of the OS mooring system were determined as follows:
 - i. The relationship between the OS excursion and mean mooring tension for every 20 minutes is close to the quasi-static excursion-tension curve of the OS for the individual bow, port and starboard mooring legs. As the OS excursion increases, the mean mooring tension gradually increases with a steeper increasing slope.
 - ii. The relationship between the OS excursion and maximum mooring tension for every 20 minutes differs from the quasi-static excursion-tension curve of the OS for the individual bow, port and starboard mooring legs. At large excursion the mooring stiffness of each leg (deployed at shallow water depth) becomes very steep, in which scenario the dynamic mooring tension is quite significant under the large-amplitude OS motions induced by strong waves. This phenomenon is demonstrated by the large difference between the maximum and mean mooring tensions at large OS excursion.

- iii. The three-legs spread mooring design of the OS limited the buoy movement inside a small position domain of 77 m long and 45 m wide, and limited the weathervane angle of the OS heading direction within a range of 38-112 degrees. The OS position domain can be approximated by the watch circles of the bow, port and starboard mooring legs, because the surface buoys of the mooring system were mainly on the sea surface under the mean mooring tensions of the field test.
 - iv. In the field test, the primary direction was toward the east for the waves, and toward either the north or south for both the current and wind. The wave, wind and current conditions all correlated closely to the mooring tensions during the field test. Therefore, all these environmental conditions should be taken into account in the mooring design to estimate mooring tensions accurately.
- The survivability characteristics of the OS mooring system were determined as follows:
 - i. Through calculating the quasi-static ratio r_a of effective force to static anchor resistance with respect to the individual maximums of bow, port and starboard mooring tensions on the OS, the movability of each anchor is estimated as follows: the port anchor was likely dragged during the significant OS drift; and the bow and starboard anchors likely experienced no movements. Note that the quasi-static value of r_a only provides preliminary investigation of anchor movement, for more accurate investigation of anchor movement, calculating the instantaneous value of r_a through dynamic analysis is suggested.

- ii. The polyester lines of the mooring system had sufficient strength to survive the storms observed in the field test. The measured maximum loads on the bow, port and starboard polyester lines were only 13%, 13% and 5%, respectively, of the designed mooring line strength. They are significantly smaller than 60%, which corresponds to the minimum safety factor of 1.67 in the mooring design guideline.
- Based on the mooring evaluations and analysis above, a new systematic procedure of designing a mooring system with adequate anchor resistance is developed independently. The design procedure incorporates the major findings of this study. Specifically, the design values of the extreme current and wind conditions, which were underestimated in the original design, need to be selected judiciously besides the well estimated extreme wave condition; secondly, the quasi-static analysis is useful in preliminary selections of the appropriate numbers of mooring legs and mooring chains properties for new mooring configurations; thirdly, dynamic simulations are important in predicting instantaneous effective force and determining the optimum mooring configuration with the smallest maximum of effective force.
- Applying the new mooring design procedure to the OS mooring system, the resulting mooring configuration facing the south with six mooring legs and L/H ratio of 1.2 was found to have the smallest maximum of effective force (33.2 kN). Taking into account the 1.5 safety factor in the anchor design, the design value of static anchor resistance is 49.8 kN. This frictional resistance force would be

provided by a concrete gravity anchor of 67.3 kN submerged weight deployed at the NETS.

C. Concluding remarks on the accuracy of the numerical model based on the fully coupled method, and applications of the numerical model in evaluating the anchor movability, fatigue damage and extreme mooring tension of the OS mooring system

- The numerical model, which was validated by field test measurements, is shown to provide accurate predictions of the mooring tensions acting on the OS at four typical scenarios A-D with harsh waves, current and wind conditions. The relative differences between the predicted and measured mooring tensions are 0% ~ 22%, -34% ~ 37% and -16% ~ 30% for the mean, standard deviation and maximum of mooring tensions, respectively. The predicted and measured power spectral densities of mooring tensions are generally in good agreements, with additional damping added on the surface buoys to reduce its over-predicted super-harmonic response. In addition, the numerical model is also shown to generally provide accurate predictions of the OS positions for the scenarios of A, B and C, when the mooring anchors were likely not dragged.
- Comparing studies of the OS mooring system and other mooring systems in the literature, the accuracy of the fully coupled method in prediction mooring tensions is found to be affected by the mooring type (catenary mooring or taut mooring), the water depth (shallow water or deep water) and the experimental test conditions (field test under ocean conditions or tank test under waves only).

- After the numerical model was validated, anchor movability, fatigue damage and extreme mooring tension of the OS mooring system were evaluated as follows:
 - i. At scenario D, which corresponded to the significant OS drift, the port anchor was likely dragged significantly; the starboard anchor was likely dragged slightly; and the bow anchor was likely not dragged. The anchor movability of each anchor was investigated through studying the ratio r_a of instantaneous effective force to static anchor resistance predicted by the numerical model. The large-amplitude oscillation of the instantaneous value of r_a compared to its mean value demonstrates the importance of dynamics analysis in studying anchor movement. The close correlation between the value of r_a and friction coefficient shows that the friction coefficient needs to be judiciously selected for each numerical study based on the sea floor type, anchor material and surface smoothness.
 - ii. Fatigue damages of the polyester lines can be estimated for environmental conditions from low sea state (with small range of mooring tension but large probability of occurrence) to high sea state (with large range of mooring tension but small probability of occurrence) through the numerical model. The predicted fatigue damages are shown to be in good agreements with the fatigue damages during the field test, when high sea state (significant wave height larger than 4 m) was not observed.
 - iii. The extreme mooring tensions of the polyester line and mooring chain can be predicted through dynamic simulations under the estimated extreme waves, wind and current conditions at the NETS. After calculating the design strengths

of the polyester line and mooring chain using the predicted extreme mooring tensions and design equation, the strengths of the polyester line and mooring chain in the field test are shown to be adequate.

Bibliography

- ABS. (2013). Design Guideline for Stationkeeping Systems of Floating Offshore Wind Turbines: American Bureau of Shipping.
- Agamloh, E. B., Wallace, A. K., & von Jouanne, A. (2008). Application of Fluid-Structure Interaction Simulation of an Ocean Wave Energy Extraction Device. *Renewable Energy*, 33(4), 748-757. doi:10.1016/j.renene.2007.04.010
- Ambühl, S., Sterndorff, M., & Sørensen, J. D. (2014). Extrapolation of Extreme Response for Different Mooring Line Systems of Floating Wave Energy Converters. *International Journal of Marine Energy*, 7, 1-19.
- Amon, E., Brekken, T. K. A., & von Jouanne, A. (2011). A Power Analysis and Data Acquisition System for Ocean Wave Energy Device Testing. *Renewable Energy*, 36(7), 1922-1930. doi:10.1016/j.renene.2010.12.016
- Ann R. Dallman, V. S. N. (2014). *Characterization of U.S. Wave Energy Converter (WEC) Test Sites: a Catalogue of Met-Ocean Data*.
- API. (1997). API-RP-2SK Recommended Practice for Design and Analysis of Stationkeeping Systems for Floating Structures.
- API. (2007). API BULLETIN 2INT-MET Interim Guidance on Hurricane Conditions in the Gulf of Mexico.
- Babarit, A., Mouslim, H., Clement, A., & Laporte-Weywada, P. (2009). *On the Numerical Modelling of the Non Linear Behaviour of a Wave Energy Converter*. Paper presented at the ASME 28th 2011 International Conference on Ocean, Offshore and Arctic Engineering.
- Badia, S., Quaini, A., & Quarteroni, A. (2008). Modular vs. Non-Modular Preconditioners for Fluid-Structure Systems with Large Added-Mass Effect. *Computer Methods in Applied Mechanics and Engineering*, 197(49-50), 4216-4232. doi:10.1016/j.cma.2008.04.018
- Baker, J. L. (2013). *Mooring Analysis of the Ocean Sentinel through Field Observation and Numerical Simulation*. (Master of Science), Oregon State University.
- Bearman, P. W., Graham, J. M. R., Obasaju, E. D., & Drossopoulos, G. M. (1984). The Influence of Corner Radius on the Forces Experienced by Cylindrical Bluff Bodies in Oscillatory Flow. *Applied Ocean Research*, 6(2), 83-89.
- Bhinder, M. A., Clive G. Mingham, Derek M. Causon, Mohammad T. Rahmati, George A. Aggidis, and Robert V. Chaplin. (2009). *A Joint Numerical and Experimental Study of a Surging Point Absorbing Wave Energy Converter (WRASPA)*. Paper presented at the ASME 2009 28th International Conference on Ocean, Offshore and Arctic Engineering.
- Brekken, T. K. A., Rhinefrank, K., von Jouanne, A., Schacher, A., Prudell, J., & Hammagren, E. (2013). Scaled Development of a Novel Wave Energy Converter Including Numerical Analysis and High-Resolution Tank Testing. *Proceedings of the Ieee*, 101(4), 866-875. doi:10.1109/jproc.2012.2234711
- Bretl, J. G. (2009). *A Time Domain Model for Wave Induced Motions Coupled to Energy Extraction*. (PhD), The University of Michigan.

- Brodtkorb, P. A., Johannesson, P., Lindgren, G., Rychlik, I., Rydén, J., & Sjö, E. (2000). *WAFO-a Matlab Toolbox For Analysis of Random Waves and Loads*. Paper presented at the The Tenth International Offshore and Polar Engineering Conference, Seattle, USA, .
- BV. (2015). NR 493 DT R03 E Classification of Mooring Systems for Permanent and Mobile Offshore Units.
- Causin, P., Gerbeau, J. F., & Nobile, F. (2005). Added-Mass Effect in the Design of Partitioned Algorithms for Fluid-Structure Problems. *Computer Methods in Applied Mechanics and Engineering*, 194(42-44), 4506-4527. doi:10.1016/j.cma.2004.12.005
- Chakrabarti, S. (2001). Empirical Calculation of Roll Damping for Ships and Barges, *Ocean Engineering*, 28, 915-932.
- Chen, X. H., Zhang, J., & Ma, W. (2001). On Dynamic Coupling Effects between a Spar and its Mooring Lines. *Ocean Engineering*, 28(7), 863-887. doi:10.1016/s0029-8018(00)00026-3
- CMPT. (1998). *Floating Structures: A Guide for the Design and Analysis*.
- Colby, C., Sodahl, N., Katla, E., & Okkenhaug, S. (2000). *Coupling Effects for a Deepwater Spar*. Paper presented at the Offshore Technology Conference.
- Coles, S. (2001). *An Introduction to Statistical Modeling of Extreme Values* (Vol. 208). London: Springer.
- Correa, F. N., Senra, S. F., Jacob, B. P., Masetti, I. a. Q., & Mourelle, M. M. (2002). *Towards the Integration of Analysis and Design of Mooring Systems and Risers: Part II - Studies on a DICAS System*. Paper presented at the ASME 2002 21st International Conference on Offshore Mechanics and Arctic Engineering.
- Dallman, A. R., & Neary, V. S. (2014). *Characterization of U.S. Wave Energy Converter (WEC) Test Sites: A Catalogue of Met-Ocean Data*. No. SAND2014-18206. Sandia National Laboratories (SNL-NM), Albuquerque, NM (United States)
- DNV. (2013). DNV-OS-E301 Position Mooring: DET NORSKE VERITAS.
- EMEC. (2014). Wave Devies. Retrieved from <http://www.emec.org.uk/marine-energy/wave-devices/>
- Faltinsen, O. (1990). *Sea Loads on Ships and Offshore Structures*: Cambridge university press.
- Fenton, J. D. (1985). A Fifth-Order Stokes Theory for Steady Waves. *Journal of waterway, port, coastal, and ocean engineering*, 111(2), 216-234.
- Finnegan, W., & Goggins, J. (2012). Numerical Simulation of Linear Water Waves and Wave-Structure Interaction. *Ocean Engineering*, 43, 23-31. doi:10.1016/j.oceaneng.2012.01.002
- Fitzgerald, J., & Bergdahl, L. (2007). *Considering Mooring Cables for Offshore Wave Energy Conversions*. Paper presented at the 7th European Wave and Tidal Energy Conference, Oporto.
- Garrett, D. L. (2005). Coupled Analysis of Floating Production Systems. *Ocean Engineering*, 32(7), 802-816. doi:10.1016/j.oceaneng.2004.10.010

- Garrett, D. L., Chappell, J. F., & Gordon, R. B. (2002). *Global Performance of Floating Production Systems*. Paper presented at the Offshore Technology Conference.
- Gilloteaux, J. C., Bacelli, G., & Ringwood, J. (2008). *A Non-Linear Potential Model to Predict Large-Amplitudes-Motions: Application to a Multi-Body Wave Energy Converter*. Paper presented at the World Renewable Energy Congress.
- Gobat, J. I., & Grosenbaugh, M. A. (2006). Time-Domain Numerical Simulation of Ocean Cable Structures. *Ocean Engineering*, 33(10), 1373-1400. doi:10.1016/j.oceaneng.2005.07.012
- Graham, J. M. R. (1980). The Forces on Sharp-Edged Cylinders in Oscillatory Flow at Low Keulegan–Carpenter Numbers. *Journal of Fluid Mechanics*, 97(2), 331-346.
- Guérinel, M., Alves, M., & Sarmiento, A. (2011). *Nonlinear Modelling of the Dynamics of a Free Floating Body*. Paper presented at the European Wave and Tidal Energy Conference.
- Hald, T., & Frigaard, P. B. (2001). *Forces and Overtopping on 2. Generation Wave Dragon for Nisum Bredning*. Aalborg University.
- Harnois, V., Johannning, L., & Thies, P. R. (2013). Wave Conditions Inducing Extreme Mooring Loads on a Dynamically Responding Moored Structure.
- Harnois, V., Parish, D., & Johannning, L. (2012). *Physical Measurement of a Slow Drag of a Drag Embedment Anchor During Sea Trials*. Paper presented at the 4th International Conference on Ocean Energy, Dublin.
- Harnois, V., Weller, S. D., Johannning, L., Thies, P. R., Le Boulluec, M., Le Roux, D., . . . Ohana, J. (2015). Numerical Model Validation for Mooring Systems: Method and Application for Wave Energy Converters. *Renewable Energy*, 75, 869-887. doi:10.1016/j.renene.2014.10.063
- Harris, R. E., Johannning, L., & Wolfram, J. (2004). *Mooring Systems for Wave Energy Converters: a Review of Design Issues and Choices*. Paper presented at the Marec2004.
- Heurtier, J. M., Le Buhan, P., Fontaine, E., Le Cunff, C., Biolley, F., & Berhault, C. (2001). *Coupled Dynamic Response of Moored FPSO with Risers*. Paper presented at the Proceedings of the ISOPE.
- Himeno, Y. (1981). *Prediction of Ship Roll Damping — State of the Art (No. 239)*.
- Idelsohn, S. R., Del Pin, F., Rossi, R., & Onate, E. (2009). Fluid-Structure Interaction Problems with Strong Added-Mass Effect. *International Journal for Numerical Methods in Engineering*, 80(10), 1261-1294. doi:10.1002/nme.2659
- Ikeda, Y., Fujiwara, T., & Katayama, T. (1993). *Roll Damping of a Sharp-Cornered Barge and Roll Control by a New-Type Stabilizer*. Paper presented at the in Proceedings of the 3rd International Offshore and Polar Engineering Conference.
- Johanning, L., Smith, G. H., & Wolfram, J. (2007). Measurements of Static and Dynamic Mooring Line Damping and their Importance for Floating WEC Devices. *Ocean Engineering*, 34(14-15), 1918-1934. doi:10.1016/j.oceaneng.2007.04.002

- Kofoed, J. P., Frigaard, P., Friis-Madsen, E., & Sorensen, H. C. (2006). Prototype Testing of the Wave Energy Converter Wave Dragon. *Renewable Energy*, 31(2), 181-189. doi:10.1016/j.renene.2005.09.005
- LCICG. (2012). *Technology Innovation Needs Assessment (TINA): Marine Energy Summary Report*.
- Lettenmaier, T., von Jouanne, A., Amon, E., Moran, S., & Gardiner, A. (2013). Testing the WET-NZ Wave Energy Converter using the Ocean Sentinel Instrumentation Buoy. *Marine Technology Society Journal*, 47(4), 164-176.
- Li, Y., Yu, Y.-H., Previsic, M., Epler, J., Nelson, E., & Lawson, M. (2016). Laboratory Experimental Investigation of Power Generation Capability and Survivability of Two-Body Floating Point Absorbers. *Journal of Oceanic Engineering*.
- Ma, W., Lee, M.-Y., Zou, J., & Huang, E. W. (2000). *Deepwater Nonlinear Coupled Analysis Tool*. Paper presented at the Offshore Technology Conference.
- Martinelli, L., Ruol, P., & Cortellazzo, G. (2012). On Mooring Design of Wave Energy Converters: the Seabreath Application. *Coastal Engineering Proceedings*, 1(33), 3.
- Martinelli, L., Spiandorello, A., Lamberti, A., & Ruol, P. (2010). *Dynamic Model for Catenary Mooring: Experimental Validation of the Wave Induced Load*. Paper presented at the The COMSOL Conference.
- Merigaud, A., Gilloteaux, J.-C., & Ringwood, J. V. (2012). *A Nonlinear Extension for Linear Boundary Element Methods in Wave Energy Device Modelling*. Paper presented at the ASME 2012 31st International Conference on Ocean, Offshore and Arctic Engineering.
- Monroy, C., Ducrozet, G., Bonnefoy, F., Babarit, A., Gentaz, L., & Ferrant, P. (2010). *RANS Simulations of a CALM Buoy in Regular and Irregular Seas using the SWENSE Method*. Paper presented at the Proceedings of the Twentieth (2010) International Offshore and Polar Engineering Conference.
- Omidvar, P., Stansby, P. K., & Rogers, B. D. (2013). SPH for 3D Floating Bodies using Variable Mass Particle Distribution. *International Journal for Numerical Methods in Fluids*, 72(4), 427-452. doi:10.1002/fld.3749
- Orcina. (2009). *OrcaFlex Manual version 9.3a*.
- Ormberg, H., Fylling, I., Larsen, K., & Sodahl, N. (1997). *Coupled Analysis of Vessel Motions and Mooring and Riser System Dynamics*. Paper presented at the International Conference on Ocean, Offshore and Arctic Engineering.
- Ormberg, H., & Larsen, K. (1998). Coupled Analysis of Floater Motion and Mooring Dynamics for a Turret-Moored Ship. *Applied Ocean Research*, 20(1-2), 55-67. doi:10.1016/s0141-1187(98)00012-1
- OSU, C. (2004). NH10 Buoy Current Data. College of Earth, Ocean, and Atmospheric Sciences (CEOAS), Oregon State University (OSU): <http://bragg.coas.oregonstate.edu/>.
- Palm, J., Paredes, G. M., Eskilsson, C., Pinto, F. T., & Bergdahl, L. (2013). *Simulation of Mooring Cable Dynamics using a Discontinuous Galerkin Method*. Paper presented at the In Proceedings of 5th International Conference on Computational Methods in Marine Engineering, Hamburg, Germany.

- Park, J. C., Kim, M. H., & Miyata, H. (1999). Fully Non-Linear Free-Surface Simulations by a 3D Viscous Numerical Wave Tank. *International Journal for Numerical Methods in Fluids*, 29(6), 685-703. doi:10.1002/(sici)1097-0363(19990330)29:6<685::aid-fld807>3.0.co;2-d
- Parmeggiani, S., Kofoed, J. P., & Friis-Madsen, E. (2013). Experimental Study Related to the Mooring Design for the 1.5 MW Wave Dragon WEC Demonstrator at DanWEC. *Energies*, 6(4), 1863-1886. doi:10.3390/en6041863
- Ran, Z. (2000). *Coupled Dynamic Analysis of Floating Structures in Waves and Current*. (PhD), Texas A&M University.
- Ricci, P., Rico, A., Ruiz-Minguela, P., Boscolo, F., & Villate, J. L. (2012). *Design, Modelling and Analysis of An Integrated Mooring System for Wave Energy Arrays*. Paper presented at the In Proceedings of the 4th International Conference on Ocean Energy.
- Rodríguez, R., Gorrochategui, I., Vidal, C., Guanche, R., Cañizal, J., Fraguera, J. A., & Díaz, V. (2011). *Anchoring Systems for Marine Renewable Energies Offshore Platforms*. Paper presented at the In OCEANS, 2011 IEEE-Spain.
- Rogne, Ø. Y. (2014). *Numerical and Experimental Investigation of a Hinged 5-Body Wave Energy Converter*. (PhD), Norwegian University of Science and Technology.
- Ruiz-Minguela, J. P., Rodríguez, R., Ricci, P., Marón, A., Prieto, M. E., & Taboada, M. (2008). *Design and Testing of the Mooring System for a New Offshore Wave Energy Converter*. Paper presented at the In Proc. 2nd International Conference on Ocean Energy.
- Salcedo, F., Ruiz-Minguela, P., Rodriguez, R., Ricci, P., & Santos, M. (2009). *Oceantec: Sea Trials of a Quarter Scale Prototype*. Paper presented at the In Proceedings of 8th European Wave Tidal Energy Conference.
- Sarpkaya, T. (1976). *Vortex Shedding and Resistance in Harmonic Flow About Smooth and Rough Circular Cylinders at High Reynolds Numbers*. Paper presented at the In Proceedings of the International Conference on Behavior of Offshore Structures BOSS'76.
- Sclavounos, P. D. (2012). Nonlinear Impulse of Ocean Waves On Floating Bodies. *Journal of Fluid Mechanics*, 697, 316-335. doi:10.1017/jfm.2012.68
- Serafin, K. A., & Ruggiero, P. (2014). Simulating Extreme Total Water Levels using a Time-Dependent, Extreme Value Approach. *Journal of Geophysical Research-Oceans*, 119(9), 6305-6329. doi:10.1002/2014jc010093
- Sethuraman, L., & Venugopal, V. (2013). Hydrodynamic Response of a Stepped-Spar Floating Wind Turbine: Numerical Modelling and Tank Testing. *Renewable Energy*, 52, 160-174. doi:10.1016/j.renene.2012.09.063
- Souli, M., & Benson, D. J. (2010). *Arbitrary Lagrangian Eulerian and Fluid-Structure Interaction: Numerical Simulation*: John Wiley & Sons.
- SST. (2009). Advanced Anchoring and Mooring Study.
- Tahar, A., Halkyard, J., & Irani, M. (2006). *Comparison of Time and Frequency Domain Analysis with Full Scale Data for the Horn Mountain Spar During Hurricane Isidore*. Paper presented at the 25th International Conference on Offshore Mechanics and Arctic Engineering.

- Tahar, A., & Kim, M. H. (2008). Coupled-Dynamic Analysis of Floating Structures with Polyester Mooring Lines. *Ocean Engineering*, 35(17-18), 1676-1685. doi:10.1016/j.oceaneng.2008.09.004
- Taylor, R. J. (1982). Interaction of Anchors with Soil and Anchor Design. No. NCEL-TN-1627. NAVAL CIVIL ENGINEERING LAB PORT HUENEME CA.
- Thies, P. R., Johanning, L., Harnois, V., Smith, H. C. M., & Parish, D. N. (2014). Mooring Line Fatigue Damage Evaluation for Floating Marine Energy Converters: Field Measurements and Prediction. *Renewable Energy*, 63, 133-144. doi:10.1016/j.renene.2013.08.050
- von Jouanne, A., Lettenmaier, T., Amon, E., Brekken, T., & Phillips, R. (2013). A Novel Ocean Sentinel Instrumentation Buoy for Wave Energy Testing. *Marine Technology Society Journal*, 47(1), 47-54.
- Weller, S., Hardwick, J., Johanning, L., Karimirad, M., Teillant, B., Raventos, A., . . . Sheng, W. (2014). *Deliverable 4.1: A Comprehensive Assessment of the Applicability of Available and Proposed Offshore Mooring and Foundation Technologies and Design Tools for Array Applications*.
- Westphalen, J., Greaves, D. M., Hunt-Raby, A., Williams, C. J. K., Taylor, P. H., Hu, Z. Z., . . . Omidvar, P. (2010). *Numerical Simulation of Wave Energy Converters using Eulerian and Lagrangian CFD Methods*.
- Wolf, N. B. (2012). *The Dynamic Mooring Force on a Wave Energy Converter Moored in a Single Point*. (M.S.), Chalmers University of Technology.
- Yu, Y.-H., & Li, Y. (2013). Reynolds-Averaged Navier-Stokes Simulation of the Heave Performance of a Two-Body Floating-Point Absorber Wave Energy System. *Computers & Fluids*, 73, 104-114. doi:10.1016/j.compfluid.2012.10.007
- Zanuttigh, B., Angelelli, E., & Kofoed, J. P. (2013). Effects of Mooring Systems On the Performance of a Wave Activated Body Energy Converter. *Renewable Energy*, 57, 422-431. doi:10.1016/j.renene.2013.02.006
- Zanuttigh, B., Martinelli, L., & Castagnetti, M. (2013). *Screening of Suitable Mooring Systems*.
- Zurkinden, A. S., Ferri, F., Beatty, S., Kofoed, J. P., & Kramer, M. M. (2014). Non-Linear Numerical Modeling and Experimental Testing of a Point Absorber Wave Energy Converter. *Ocean Engineering*, 78, 11-21. doi:10.1016/j.oceaneng.2013.12.009

Appendices

Appendix A **Drag coefficient C_d and eddy-making damping coefficient C_D for the FPA model in the nonlinear potential flow solver**

The drag coefficient C_d of the Morison equation $F = -\frac{1}{2}\rho C_d A(u_s - u_f)|u_s - u_f|$ is related to the local Reynolds number ($Re = \frac{U_m D}{\nu}$), Keulegan–Carpenter number ($KC = \frac{U_m T}{D}$) and cross section geometry at different positions of the FPA (Faltinsen, 1990), where U_m is maximum fluid velocity, D is a characteristic dimension, ν is the kinematic viscosity and T is the wave period.

The FPA is divided into three parts (the floater, spar and plate) and the drag coefficient C_d for each section in local x' and z' direction is decided individually. The local x' direction is defined as the direction orthogonal to the spar axis and in the same vertical plane as the direction of waves; the local z' direction is defined as the direction along the spar axis.

In the local x' direction, the cross-section shapes of the float, spar and plate are considered as circular cylinders. C_d for the float, spar and plate are 0.5, 2 and 0.5 respectively (based on the local KC number and Reynolds number (Sarpkaya, 1976)).

In the local z' direction, the cross-section shapes of the float and plate are considered as a facing square and a flat plate respectively. C_d for the float and plate are 3 and $8KC^{-0.33}$ (based on the study of (Graham, 1980) and (Bearman et al., 1984)). The drag force on the spar is omitted in the local z' direction.

The value of eddy-making drag coefficient C_D in Equation 2.8 ($F_e = -C_D \dot{\theta} |\dot{\theta}|$) is based on the cross-section geometry of the FPA. As there are rarely any empirical drag coefficients for this kind of I shaped cross section, C_D was initialized to be 9.4×10^8

which is equivalent to the drag coefficient for a rectangular cross section barge (Equation A.1-2 (Ikeda et al., 1993)) with the same dimensions and COG as the FPA (Draft=35m, Beam=14m, Length=14m, COG=-23m). Then C_D is adjusted to 4×10^9 through trial runs until the numerical pitch response was close to the experimental data. The empirical eddy-making drag coefficient of a rectangular shaped barge is expressed as

$$C_D = \frac{3}{4} \rho L D_s^4 \left(H_0^2 + 1 - \frac{OG}{D_s} \right) \left[H_0^2 + \left(1 - \frac{OG}{D_s} \right)^2 \right] \quad \text{Eq. (A.1)}$$

$$H_0 = \frac{B}{2D_s} \quad \text{Eq. (A.2)}$$

where L is the length of barge; D_s is the draft of the barge; H_0 is the half beam draft ratio; B is the beam of the barge and OG is the vertical distance (positive downward) from still water level (SWL) to COG. In the heave direction, the magnitude of the total force is smaller than those of all the individual forces except the mooring force for each wave period. The magnitude of the sum of the restoring force and the Froude-Krylov force, is generally close to the magnitudes of the radiation force and the diffraction force but larger than the magnitude of the viscous force. The magnitude of the viscous force is smaller than the magnitudes of the radiation force, the diffraction force and the sum of the restoring force and the Froude-Krylov force, while larger than the magnitude of the mooring force.

In the surge direction, the magnitude of the total force is larger than the magnitudes of all the individual forces except the sum of the restoring force and the Froude-Krylov force for each wave period. The magnitude of the sum of the restoring force and the Froude-Krylov force, is generally larger than the magnitudes of the radiation force, the

diffraction force and the viscous force. The magnitude of the viscous force is generally smaller than all the other individual forces.

The drag coefficients C_d and C_D in this study are listed in Table 5-1.

Table 5-1. Drag coefficients for the FPA

	Direction	
Floater	x'	$C_d = 0.5$
	z'	$C_d = 3$
Spar	x'	$C_d = 2$
	z'	0
Plate	x'	$C_d = 0.5$
	z'	$C_d = 8KC^{-0.33}$
FPA	pitch	$C_D = 4 \times 10^9$

References

- Bearman, P. W., Graham, J. M. R., Obasaju, E. D., & Drossopoulos, G. M. (1984). The influence of corner radius on the forces experienced by cylindrical bluff bodies in oscillatory flow. *Applied Ocean Research*, 6(2), 83-89.
- Faltinsen, O. (1990). *Sea loads on ships and offshore structures*: Cambridge university press.
- Graham, J. M. R. (1980). The forces on sharp-edged cylinders in oscillatory flow at low Keulegan–Carpenter numbers. *Journal of Fluid Mechanics*, 97(2), 331-346.
- Ikeda, Y., Fujiwara, T., & Katayama, T. (1993). *Roll damping of a sharp-cornered barge and roll control by a new-type stabilizer*. Paper presented at the In Proceedings of the 3rd International Offshore and Polar Engineering Conference.
- Sarpkaya, T. (1976). *Vortex shedding and resistance in harmonic flow about smooth and rough circular cylinders at high Reynolds numbers*. Paper presented at the In Proceedings of the International Conference on Behavior of Offshore Structures BOSS'76.

Appendix B **Calculation the hydrostatic force and the Froude-Krylov force**

The restoring force is the sum of the hydrostatic force and the gravity force. The hydrostatic force is calculated as the integral of the static pressure p_s , which is equal to $\rho g Z_0$, over the instantaneous wetted surface. Z_0 is the vertical distance (positive downward) from still water level to the submerged integration point. The static pressure is calculated as

$$p_s = \rho g (Z_r - \eta) \quad \text{Eq. (B.1)}$$

where η is the instantaneous water surface elevation (positive upward) and Z_r is the vertical distance from the water surface to the submerged integration point.

Based on Equation B.1, the static pressure has an oscillating term $-\rho g \eta$ which is proportional to the wave amplitude. Even when the relative motion between the FPA and water surface is very small, the calculated hydrostatic force still has large oscillation under large amplitude waves.

The Froude-Krylov force is calculated as the integral of the dynamic pressure p_d over the instantaneous wetted surface. The dynamic pressure is calculated as

$$p_d = \rho \frac{d\phi_i}{dt} \quad \text{Eq. (B.2)}$$

where ϕ_i is velocity potential of the undisturbed incident wave field, which is theoretically known.

For the total pressure, which is the sum of the hydrostatic pressure and hydrodynamic pressure, the oscillation term $-\rho g \eta$ in the hydrostatic pressure is balanced out by the hydrodynamic pressure. Therefore, when the relative motion between the FPA and water surface is small, the sum of the hydrostatic force and the Froude-Krylov force also has small oscillation under large amplitude waves. So instead of the individual

hydrostatic force or Froude-Krylov force, the sum of these two forces is compared to the total force in this study.

Appendix C Schematics of the initial Ocean Sentinel mooring design

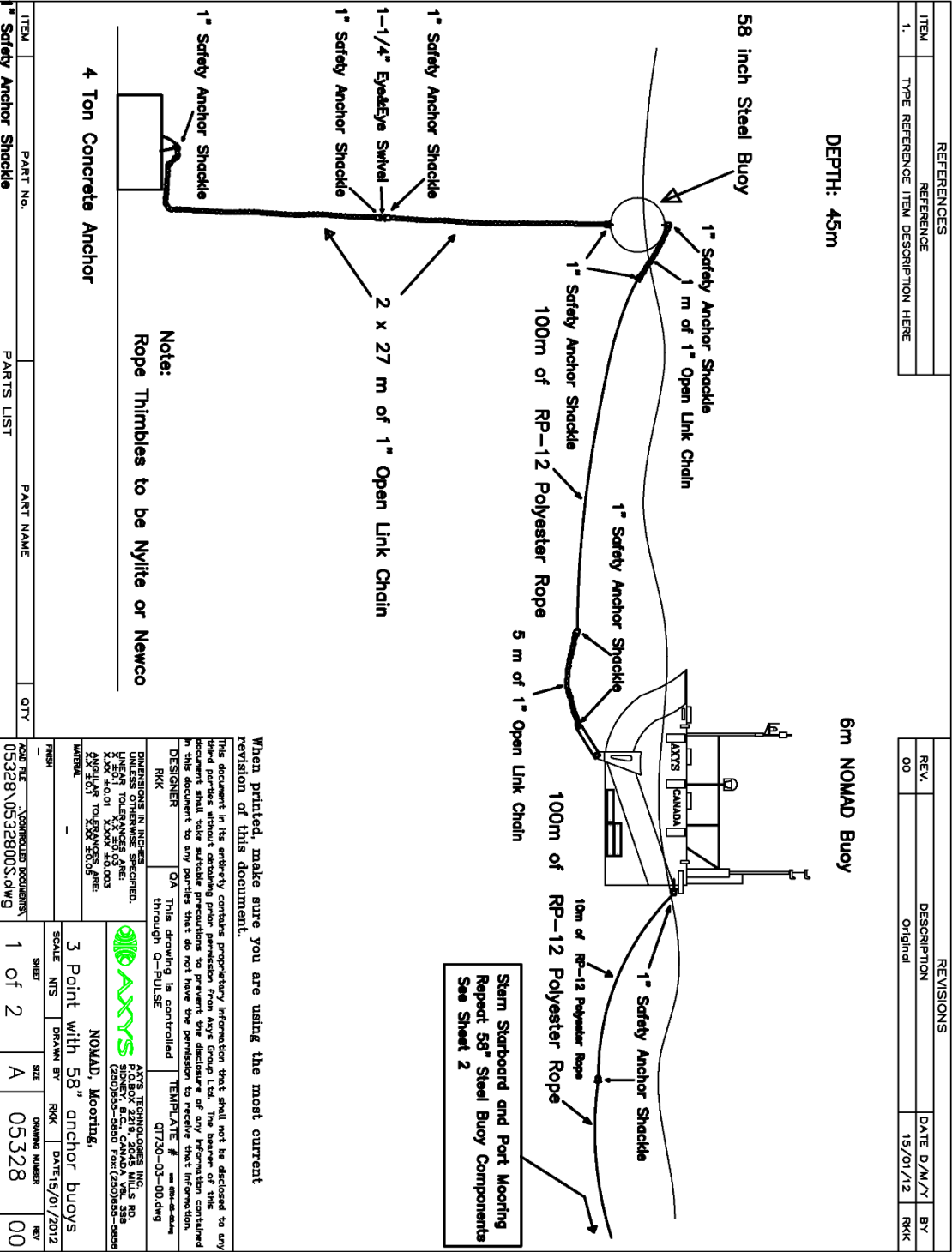


Figure 5-1. Schematics of Initial Ocean Sentinel Mooring Design(AXYS, 2012)

References

AXYS Technologies Inc (2012). Schematics of the Ocean Sentinel mooring design.

Appendix D **Calculation of the reserved capacity C_r with respect to the horizontal force at the top end of the mooring chain F_{th}**

The calculation of the reserved capacity C_r with respect to the horizontal force at the top end of the mooring chain F_{th} is divided to three stages.

In the first stage, when F_{th} is smaller, only part of the mooring chain is suspended. The angle line at the bottom end of the mooring chain θ_b is zero. The anchor reserved capacity of this stage 1 is calculated as

$$C_r = cW_a - F_{th} \quad \text{Eq. (C.1)}$$

In the second stage, after F_{th} increases to a certain value, the whole mooring chain is suspended. The angle line at the bottom end of the mooring chain θ_b is not zero. The anchor reserved capacity of this stage is calculated as

$$C_r = c(W_a - F_{bv}) - F_{th} \quad \text{Eq. (C.2)}$$

where F_{bv} can be calculated based on the catenary equations in Sluijs and Blok (1977).

In the third stage, after F_{th} increases to an even higher value, the vertical force at the top end of the mooring chain F_{tv} reaches to its maximum value B_r , which is the maximum buoyance force of the surface buoy subtracted by the weight of the surface buoy in water. At this stage, the surface buoy is below the water surface.

The anchor reserved capacity of the third stage is calculated as

$$C_r = c(W_a - B_r + W_c) - F_{th} \quad \text{Eq. (C.3)}$$

where W_c is the submerged weight of the mooring chain.

References

Sluijs, M. F. v., & Blok, J. J. (1977). *The Dynamic Behavior of Mooring Lines*. Paper presented at the Offshore Technology Conference, Houston.

Appendix E **Measured mooring tensions with respect to time**

The tension of the bow, port and starboard mooring lines acting on the OS were measured by the load cells attached to the mooring lines during the whole deployment of the OS. The tension data are recorded at 20 Hz.

The time history of average and maximum tension of the bow, port and starboard mooring lines for every three hours from 07/30 to 09/22 are shown in Figure 5-2. It is found that there is a correlation between the maximum tension and the average tension for each mooring line. At times of c, d, g, both average and maximum tension of the port line reached their local maximum values. At the same times, the average and maximum tension of the bow line also reached their local maximum values, while the average tension of the starboard line was at its minimum value which shows a slack condition. At a, b, e and f times both average and maximum tensions of the starboard line reached their local maximum values. At the same times, the average and maximum tensions of the bow line also reached their local maximum values, while the average tension of the port line was at its minimum value which shows a slack condition. At time h, which was on 09/22, the average and maximum tension of the bow and port line reached their global maximum values between 07/30 and 09/22. At the same time, the average and maximum tension of starboard line reached its local maximum values.

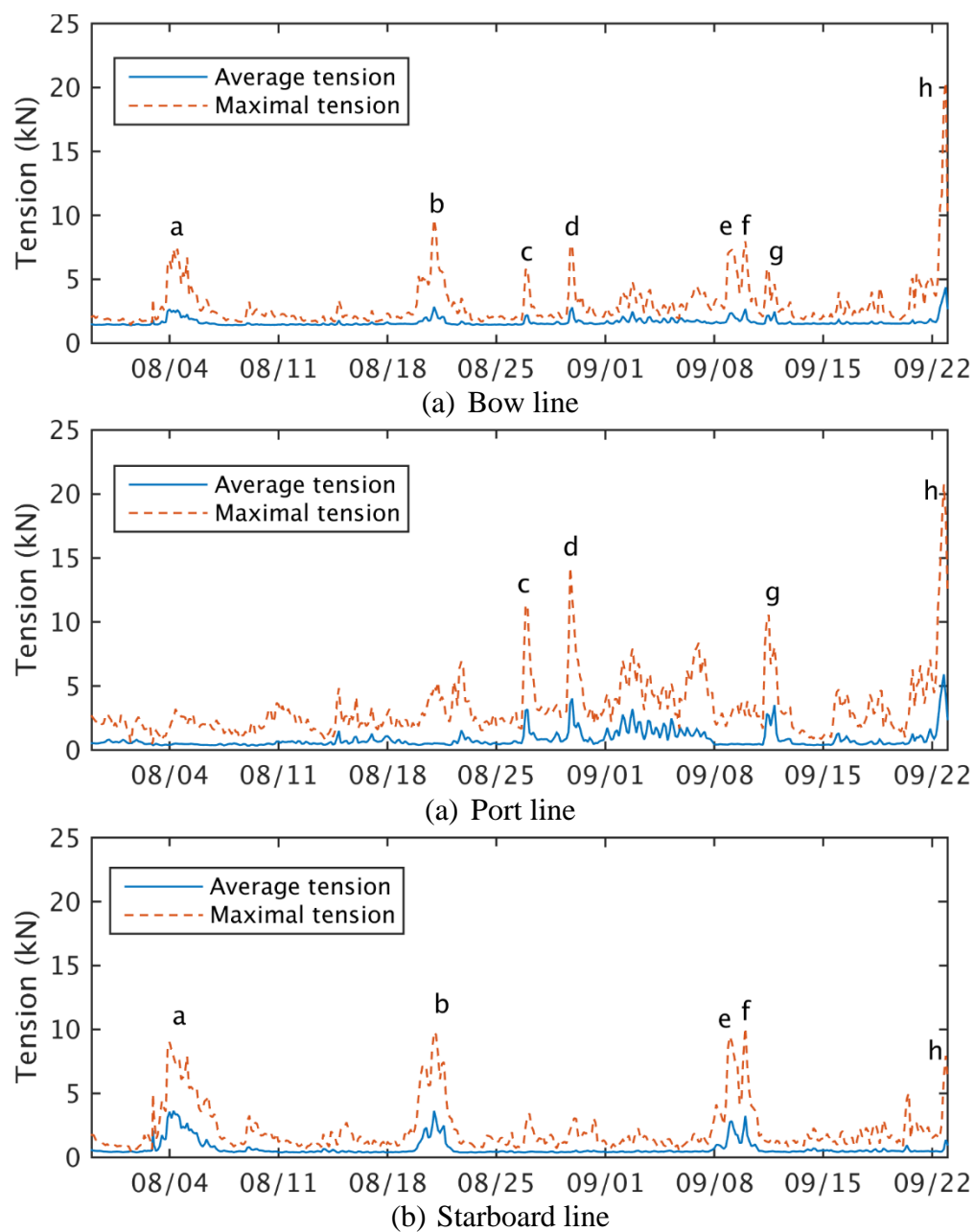


Figure 5-2. Time history of the average and maximum tension of the bow, port and starboard mooring line from 07/30 to 09/22, and the typical times with large mooring tensions

Appendix F **Measured environmental conditions**

During the whole deployment of the OS, the wave data measured by the TRIAXYS buoy (deployed approximately 140m away from the OS) were recorded every 20 minutes in the form of wave height, wave period and wave frequency spectrum. The current measured by the TRIAXYS buoy were recorded every 20 minutes in the form current magnitude and direction changing along with water depth. The wind data measured by the onboard instrument of the OS were recorded every 10 minutes in the form of wind speed and wind direction.

The time history of measured wave, current and wind magnitudes during the whole deployment of the OS (07/30-10/03) is shown in Figure 5-3. The significant wave height for every 20 minutes was between 0.449 and 6.751 m. The surface current speed was between 0.002 and 1.009 m/s. The average wind speed for every 20 minutes was between 0.3 and 20.6 m/s. For the whole deployment, the average significant wave height was 1.607 m; the average surface current speed was 0.259 m/s; the average wind speed was 4.261 m/s.

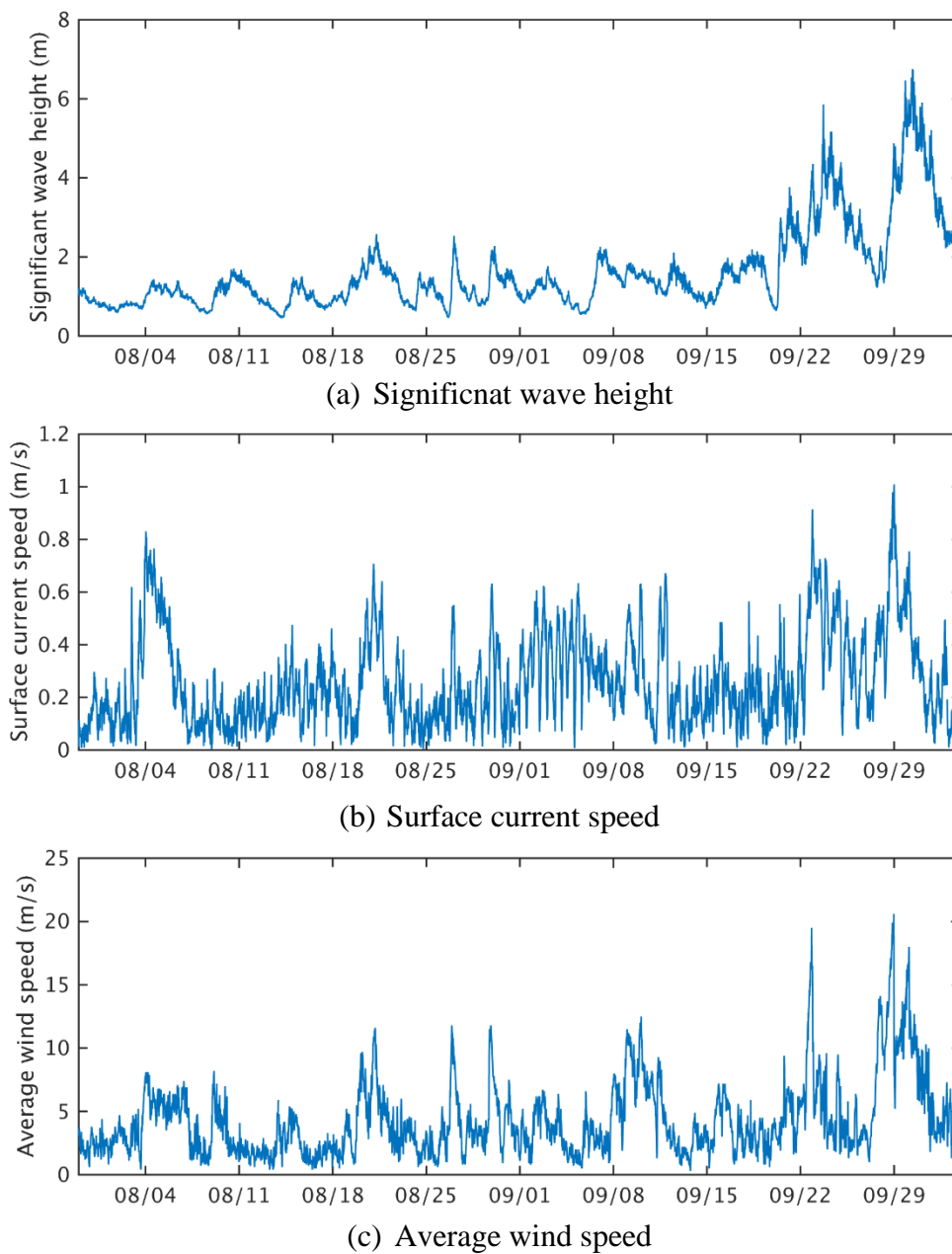


Figure 5-3. Time history of significant wave height, current speed and wind speed during the whole deployment of Ocean Sentinel (07/30-10/03)

Appendix G **Relationship between environmental conditions and Ocean Sentinel positions**

The current, wind and wave conditions with respect to OS positions from 07/30 to 09/21 are plotted in Figure 5-4, Figure 5-5 and Figure 5-6 respectively. The length and color of each arrow reflect the value of surface current speed (m/s), average wind speed (m/s) and significant wave height (m) respectively; the direction of each arrow reflects the direction where the current, wind and wave are moving to.

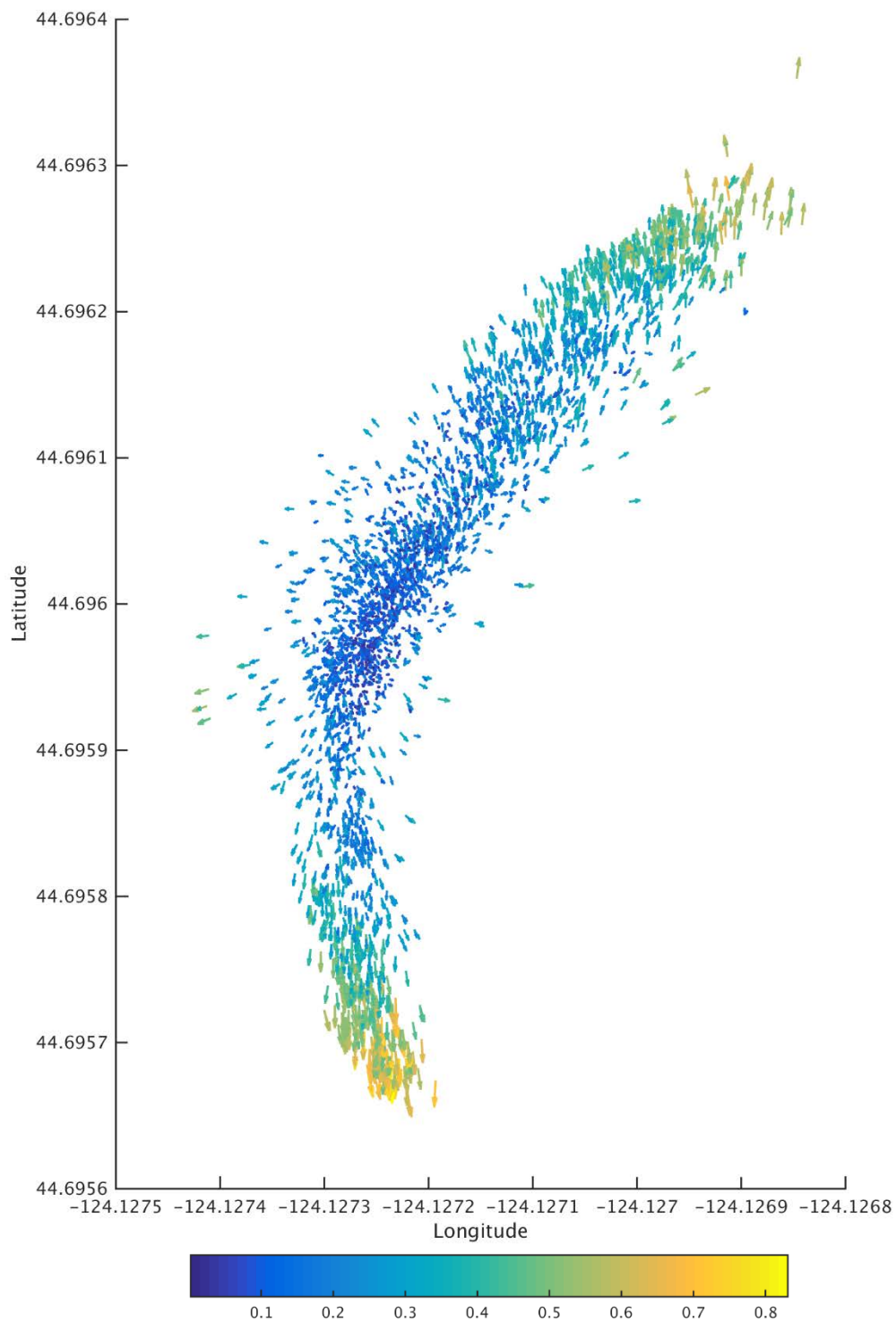


Figure 5-4. Relationship between current conditions (speed and direction) and Ocean Sentinel positions

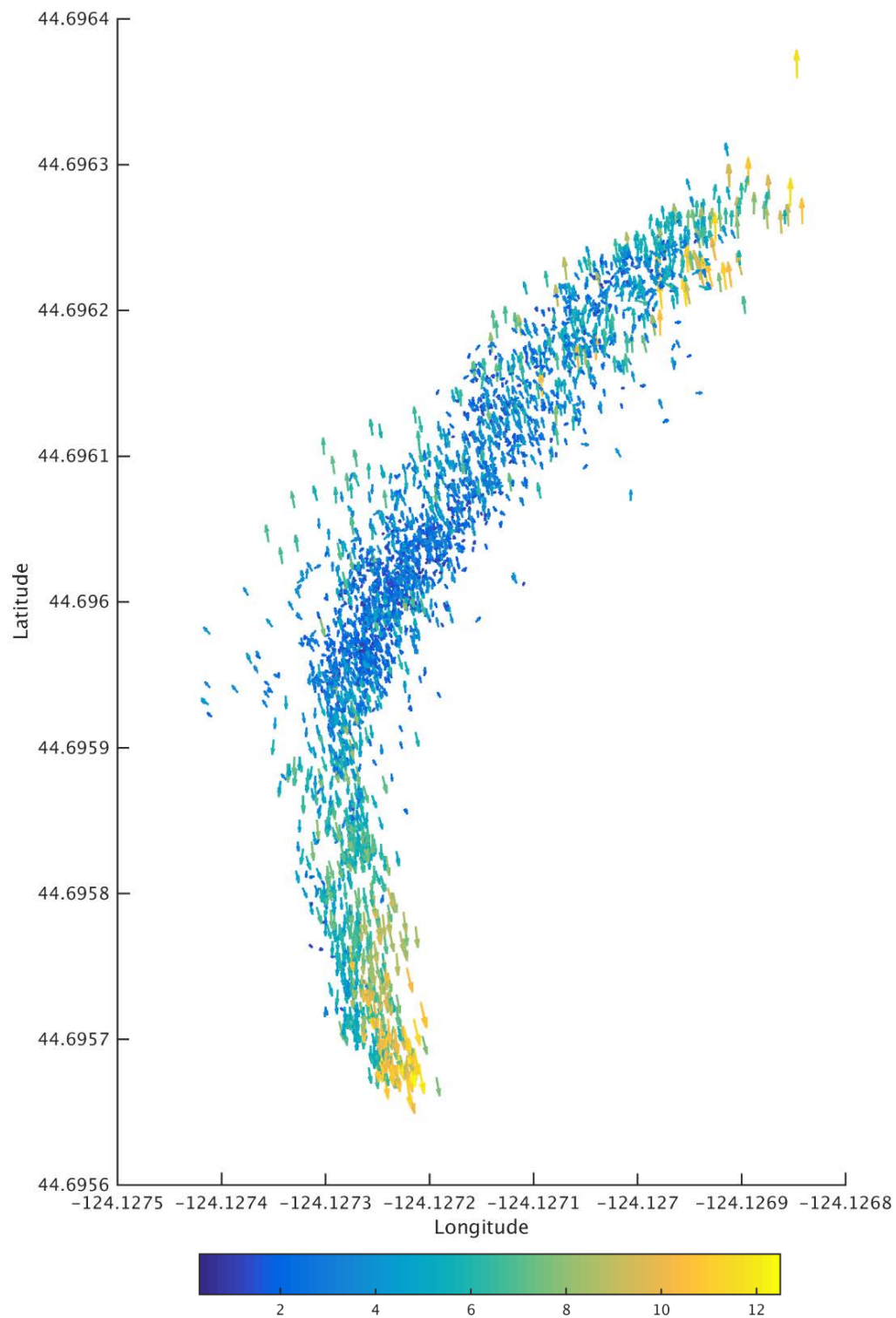


Figure 5-5. Relationship between wind conditions (speed and direction) and Ocean Sentinel positions

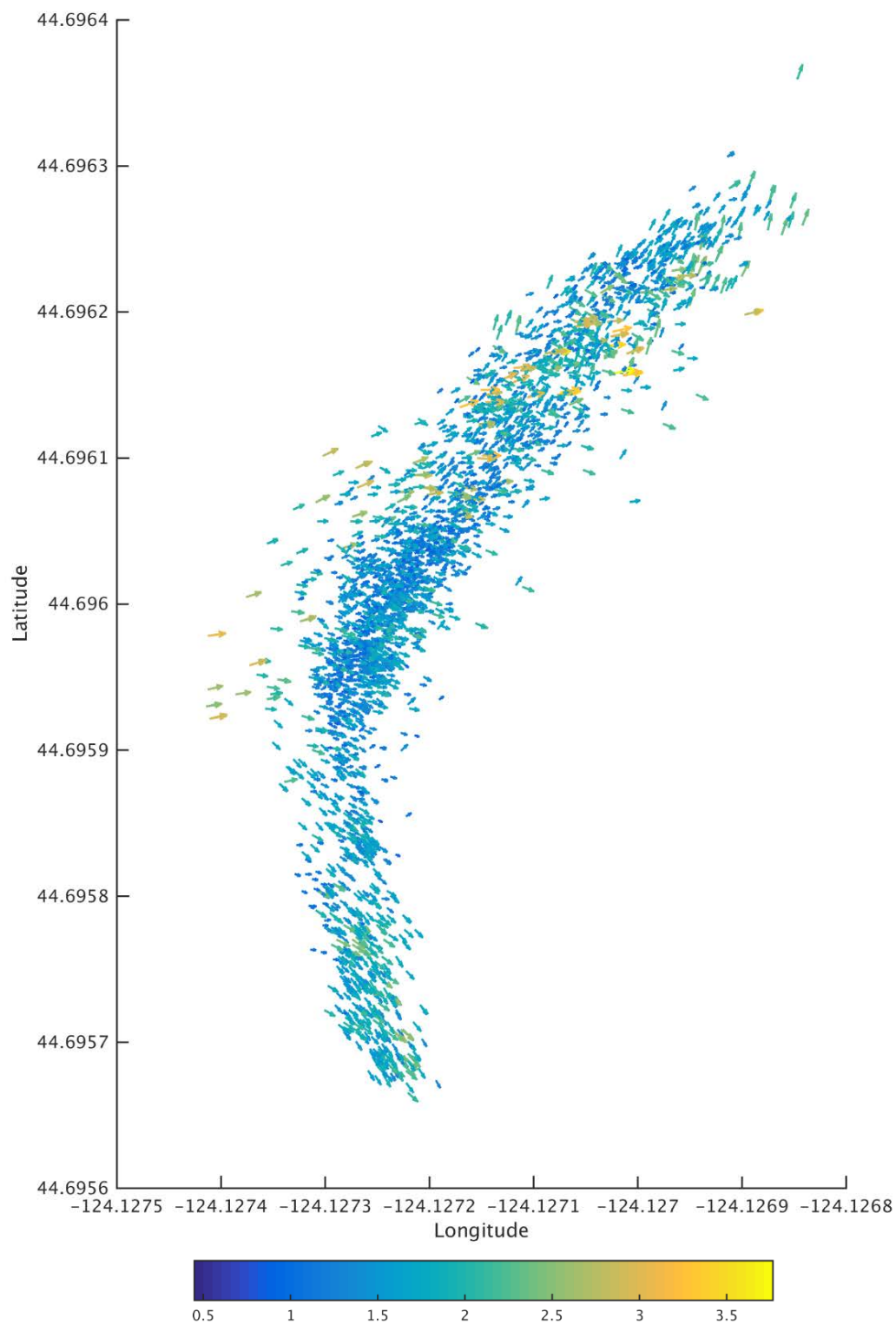


Figure 5-6. Relationship between wave conditions (wave height) and Ocean Sentinel positions

Figure 5-4 demonstrates that there was a strong relationship between the surface current and OS positions. For instance, most of the current arrow vectors, which are close to the boundary of OS positions, point out of the boundary; current vectors with large amplitude are distributed mostly close the boundary. In addition, the OS was pushed toward the northeast edge as the magnitude of the north oriented current increased; the OS was pushed toward the south edge as the magnitude of the south oriented current increased.

Figure 5-5 demonstrates that there was a moderate relationship between the wind and OS positions. For instance, many of the wind arrow vectors, which are close to the boundary of OS positions, point away from the boundary; however, wind vectors with large amplitudes are distributed not only close to the boundary but also inside the position domain.

Figure 5-6 demonstrates that there was a weak relationship between the wave and OS positions. For instance, only small part of the wave arrow vectors, which are close to the boundary of OS positions, point out of the boundary; the wave vectors, which are close to the west boundary, mainly point toward the east direction; large part of wave vectors with large amplitude are distributed inside the position domain. However, the wave direction was mainly toward the northeast and southeast when the OS was at its northeast and south edge respectively. This shows that the waves at strong current may contribute to the drift force acting on the OS which help move the OS further toward the northeast or south edge. This current and wave interaction effect was also discussed in DNV (2010) and Stansberg et al. (2013).

Compare current, wind and wave distribution (Figure 5-4, Figure 5-5 and Figure 5-6) with the mooring tension distribution with respect to OS positions (Figure 3-7), it is found that the maximum tensions of mooring line are not only affected by the wave condition but also affected by the current and wind condition. For the study of extreme mooring tensions, the current and wind condition is likely to be more important than wave condition. This is because as the average tension of mooring line increases, which is mainly induced by the current and wind load, the mooring line becomes stiffer in tension change with respect to line displacement (caused by waves). For example, when the current and wind speed were relatively large at the northeast or south edge as shown in Figure 5-4 and Figure 5-5 respectively, the corresponding dynamic tension of the bow, port or starboard line was also relatively large as shown in Figure 3-7; when the significant wave height was relatively large inside the position domain as shown in Figure 5-6, the corresponding dynamic tension of the bow, port or starboard line was relatively moderate as shown in Figure 3-7.

References

- Stansberg, C. T., Hoff, J. R., Hermundstad, E. M., & Baarholm, R. (2013). *WAVE DRIFT FORCES AND RESPONSES IN CURRENT*. Paper presented at the ASME 2013 32nd International Conference on Ocean, Offshore and Arctic Engineering
- DNV. (2010). *ENVIRONMENTAL CONDITIONS AND ENVIRONMENTAL LOADS*.

Appendix H Wind and current drag coefficients

The angle of attack ε of the wind and current to the Ocean Sentinel are defined as in Figure 5-7. The wind and current drag coefficients of the Ocean Sentinel at scenario a, b, c and d are shown in Figure 5-8 and Figure 5-9.

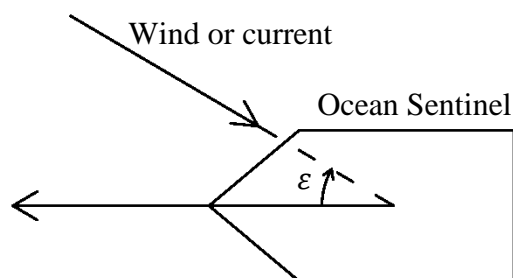


Figure 5-7. Angle of attack definition.

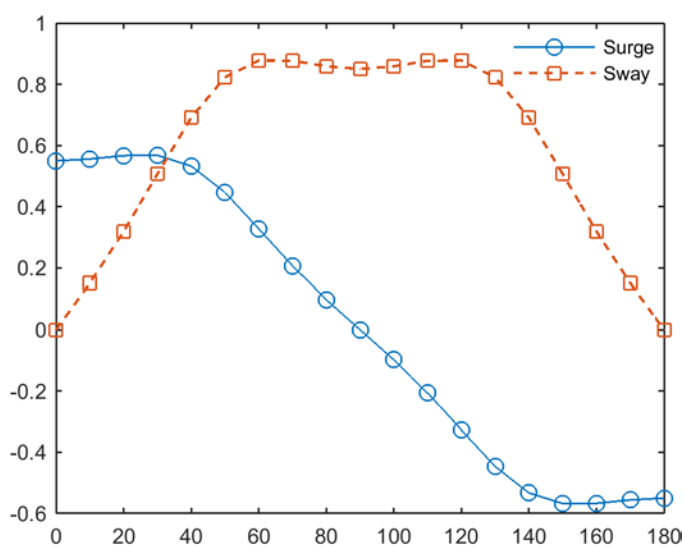
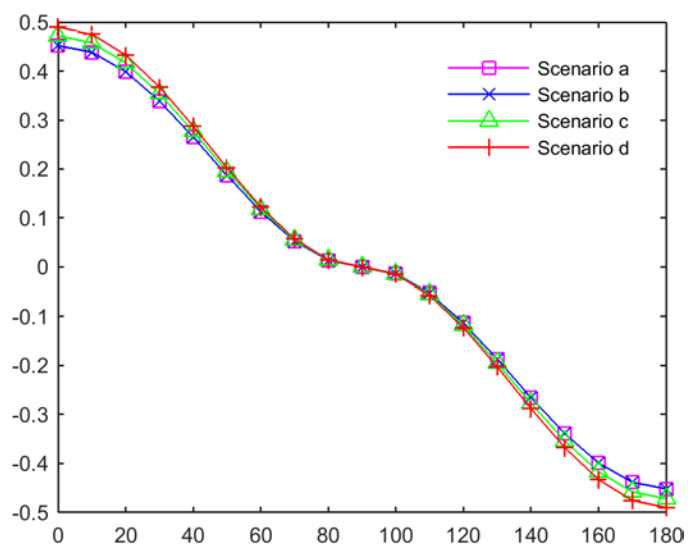
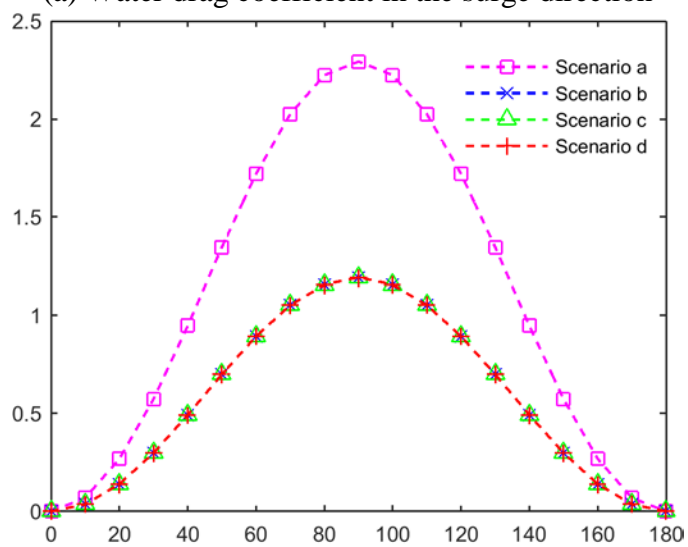


Figure 5-8. Wind drag coefficients at scenario a, b, c and d



(a) Water drag coefficient in the surge direction



(b) Water drag coefficient in the sway direction

Figure 5-9. Water drag coefficient at scenario a, b, c and d